

1 **Tropical upper tropospheric trends in ozone and carbon** 2 **monoxide (2005–2020): observational and model results**

3 Lucien Froidevaux¹, Douglas E. Kinnison², Benjamin Gaubert², Michael J. Schwartz¹, Nathaniel
4 J. Livesey¹, William G. Read¹, Charles G. Bardeen², Jerry R. Ziemke^{3,4}, and Ryan A. Fuller¹

5 ¹Jet Propulsion Laboratory, California Institute of Technology, Pasadena, California, USA

6 ²NSF National Center for Atmospheric Research (NSF NCAR), Boulder, Colorado, USA

7 ³NASA Goddard Space Flight Center, Greenbelt, MD, USA

8 ⁴Goddard Earth Sciences Technology and Research (GESTAR)/Morgan State University,
9 Baltimore, MD, USA

10 *Correspondence to:* Lucien Froidevaux (lucienf@jpl.nasa.gov)

11 **Abstract.** We analyze tropical ozone (O₃) and carbon monoxide (CO) distributions in the upper
12 troposphere (UT) and their temporal changes for 2005–2020 using Aura Microwave Limb Sounder
13 (MLS) observations and chemistry climate model simulations. The simulations are from the Whole
14 Atmosphere Community Climate Model (WACCM) and two variants of the Community
15 Atmosphere Model with Chemistry (CAM-chem), each variant using different anthropogenic
16 emissions for CO. Upper tropospheric trends and variability diagnostics are obtained from multiple
17 linear regression analyses.

18 We compare the model and MLS annual climatologies, focusing on 147 and 215 hPa pressure
19 levels; the model abundances are typically ~5–15% smaller than MLS O₃ at 215 hPa, but larger
20 than the MLS values at 147 hPa by ~20%. MLS O₃ has an averaged UT zonal mean trend at 20°S–
21 20°N of $+0.39 \pm 0.28$ %yr⁻¹; the **WACCM simulation and both CAM-chem simulations** have
22 similar trends, although the WACCM result is somewhat smaller. Our analyses for specific
23 latitude/longitude bins yield positive O₃ trends up to 1.4 %yr⁻¹ over Indonesia and East of that
24 region, as well as over tropical Africa and the tropical Atlantic. Positive tropical UT mapped O₃
25 trends are generally captured by the model simulations, although in a more muted way. We find
26 broad similarities (and some differences) between the mapped MLS-derived UT O₃ trends and
27 corresponding mapped trends of tropospheric column ozone.

28 Regarding UT CO, the model climatologies generally show an underestimate versus the MLS
29 climatology, with model average biases usually about -10% to -20%. Also, in the northern
30 hemisphere tropics, we find significantly poorer model fits to the observed phasing of CO seasonal
31 changes at 215 hPa than at 147 hPa. This discrepancy is much smaller for the comparison of

32 modeled and Measurements of Pollution in the Troposphere (MOPITT) V9J CO columns. We also
33 find that the sensitivity of UT CO to El Niño / Southern Oscillation (ENSO) is positive at all
34 tropical longitudes, in contrast to the dipolar longitudinal structure that exists for UT O₃ ENSO
35 sensitivity. The MLS zonal mean CO UT trend is $-0.25 \pm 0.30 \text{ \%yr}^{-1}$, whereas the corresponding
36 model CO trends are close to zero ($0.0 \pm 0.14 \text{ \%yr}^{-1}$) when the anthropogenic emissions used in
37 CAM-chem and WACCM are taken from Community Emissions Data System (CEDS) version 2.
38 **The CAM-chem simulation driven by CAMS-GLOB-ANTv5 emissions** yields averaged CO UT
39 trends of $0.22 \pm 0.19 \text{ \%yr}^{-1}$, in contrast to the negative tendencies prevalent in the MLS CO trends
40 throughout the tropics. The negative MLS tropical UT CO trends for 2005–2020 agree with (but
41 tend to be smaller in magnitude than) previously published total column CO trends.

42 The MLS-derived upper tropospheric tropical trends in O₃ and CO arise from a well-sampled
43 multi-year data set. We find that there are similarities (and a few differences) between the
44 measured UT trends and corresponding results from model simulations, which incorporate state-
45 of-the-art representations of the complex interplay between emissions, photochemistry,
46 convection, and transport in the upper troposphere and lower stratosphere. These results will
47 contribute to the continuing assessments of tropospheric evolution.

48 **1 Introduction**

49 Tropospheric ozone (O₃) can be influenced by downward transport from the stratospheric ozone
50 layer, but the main O₃ source in the troposphere is in situ photochemical formation through the
51 oxidation of carbon compounds in the presence of (catalyzing) nitrogen oxides (NO_x = NO + NO₂)
52 (Crutzen, 1973; Logan, 1985); tropospheric ozone loss is dominated by in situ photochemistry and
53 by deposition at the Earth's surface (Monks et al., 2015). Past studies have also shown that the
54 main sources of tropospheric NO_x are fossil fuel combustion, biomass burning, soil microbial
55 activity, and lightning. Global anthropogenic emissions dominate the natural NO_x sources and
56 biomass burning plays quite a significant role in the tropics. There is evidence from in situ
57 measurements from ozonesondes and commercial aircraft for slow increases in tropospheric and
58 upper tropospheric O₃ abundances (e.g., Cooper et al., 2014; Gaudel et al., 2020; Thompson et al.,
59 2021; Wang et al., 2022). At the surface, regional differences have been noted, for example, a
60 leveling off in ozone increases over western Europe and parts of the United States after the 1990s,
61 including some decreases, depending on the season. Changes in tropospheric ozone precursor

62 emissions (e.g., from NO_x, carbon monoxide – CO, and volatile organic compounds) have been
63 implicated as causes for global tropospheric ozone change over the past few decades (Zhang et al.,
64 2016; Zheng et al., 2018; Liu et al., 2022; Wang et al., 2022). Souri et al. (2017) and Zhang et al.
65 (2016), for example, discussed the existence of decreases in NO_x emissions over developed
66 countries following emission regulations after the turn of the century. In the North Atlantic region,
67 both surface O₃ and CO have decreased; Kumar et al. (2013) showed this for 2001–2011. Such
68 decreases have been attributed to a decline in anthropogenic emissions from North America that
69 more than compensate for emission increases over parts of Asia. Furthermore, after the dramatic
70 reduction in global economic activity following the CO₂ CoronaVirus Disease 2019 pandemic,
71 significant reductions in northern hemisphere (NH) tropospheric ozone values were observed in
72 2020 and 2021, although the tropical decreases are much smaller (Ziemke et al., 2022; Steinbrecht
73 et al., 2021; Bouarar et al., 2021; Miyazaki et al., 2021).

74 CO is another important pollutant in the troposphere. Its primary tropospheric sources are
75 incomplete combustion (biomass burning emissions and pollution from industrial and traffic-
76 related emissions), and the oxidation of methane and other hydrocarbons (Logan et al., 1981;
77 Crutzen and Andreae, 1990; Khalil and Rasmussen, 1990); its main tropospheric loss pathway is
78 oxidation by the hydroxyl radical (OH). Lower tropospheric CO anomalies are propagated upward
79 by convection and general ascent to produce a tropical “CO tape recorder” (Schoeberl et al., 2006),
80 primarily as a result of biomass burning episodes near the equinoxes (Duncan et al., 2003, 2007;
81 Logan et al., 2008; Nassar et al., 2009; Livesey et al., 2013; Huang et al., 2016). Further insights
82 into the transport of CO pollution into the upper troposphere and lower stratosphere (UTLS) have
83 been provided by Park et al. (2013), who examined CO and other species from the Atmospheric
84 Chemistry Experiment Fourier Transform Spectrometer (ACE-FTS) and MLS. In the tropics, the
85 clear signature of semiannual maxima centered around April and October were observed, primarily
86 over Africa, Indonesia, and South America, with connections to biomass burning and convection
87 patterns. Park et al. (2021) examined CO pollution transport to the UTLS during and long after the
88 highly enhanced 2015 Indonesian fire season, using a combination of CO satellite data and model
89 simulations (with the CAM-chem model). **This model produced underestimates in CO**
90 **comparisons versus tropical upper tropospheric CO from MOPITT, as well as versus MLS and**
91 **ACE-FTS CO data in this region; those retrievals compared well with MOPITT CO.** In terms of

92 tropospheric CO trends, Worden et al. (2013a) found significant CO column decreases for the
93 2000–2011 period at a rate of -1.5 \%yr^{-1} over Europe, East Asia, and the United States; this work
94 was based mainly on data from the Measurements of Pollution in the Troposphere (MOPITT) and
95 the Atmospheric Infrared Sounder (AIRS) (see also Warner et al., 2013). Using MOPITT data,
96 Laken and Sahbaz (2014) obtained a significant global CO trend of -0.6 \%yr^{-1} from 2000–2012;
97 they also pointed to significant increasing trends over parts of Asia, South America, and Africa.
98 Buchholz et al. (2021) found a similar result using 2002–2018 gridded time series from MOPITT
99 CO, AIRS, and other satellite instruments; the global trend for this period was found to be $-0.5 \pm$
100 0.3 \%yr^{-1} , with a slower decreasing trend during 2010–2018. Hedelius et al. (2021) also discussed
101 MOPITT-inferred decreasing trends in column CO for 2002–2017 and pointed out that decreases
102 in CO emissions, obtained from the Emissions Database for Global Atmospheric Research
103 (EDGAR) version 4.3.2, do not always match column CO trends. Analyses of ground-based in situ
104 surface CO data also point to a slowdown in the rate of decrease of CO after 2010, in comparison
105 to the 2001–2010 decade (Patel et al., 2024). There is also a north-south interhemispheric
106 difference in the CO abundances (and total columns), along with faster rates of decrease in the
107 northern hemisphere. Decreasing CO emissions from anthropogenic and biomass burning sources
108 appear to be the main cause of global tropospheric CO decreases (Jiang et al., 2017, Andela et al.,
109 2017), while secondary CO resulting from methane oxidation is increasing (Gaubert et al., 2017).
110 Some steeper CO decreases have been observed in local extra-tropical near-surface data (Li and
111 Liu, 2011; He et al., 2013; Yoon and Pozzer, 2014; Gratz et al., 2015), apparently because of
112 tighter air quality standards and reduced pollution from industrial and traffic-related emissions.

113 The upper troposphere is a complex region where production of NO_x by lightning (Schumann
114 and Huntrieser, 2007; Murray et al., 2014), aircraft NO_x emissions (Hoor et al., 2009; Brasseur et
115 al., 2016; Lee et al., 2021; Wang et al., 2022), and stratosphere-troposphere exchange (STE) (Sudo
116 et al., 2003; Collins et al., 2003; Hegglin and Shepherd, 2009; Hess and Zbinden, 2013; Neu et al.,
117 2014) can significantly impact ozone concentrations; STE plays a larger role in the extra-tropics
118 than in the tropics (Hsu and Prather, 2014). Upper tropospheric trend analyses of in situ CO data
119 from commercial aircraft participating in the In-service Aircraft for a Global Observing System
120 (IAGOS, see Petzold et al., 2015) measurements have indicated decreasing trends from 1995 to
121 2013 in northern midlatitude UT CO, with some larger (and statistically robust) trends as high as
122 -2 to -3 \% yr^{-1} over eastern Asia (Cohen et al., 2018). The UT ozone trends from the latter analyses

123 were found to range between 0.25 to 0.45 ppbv yr⁻¹; this reflects changes of order 0.4–0.8% yr⁻¹.
124 In terms of variability, there are interannual composition changes in the troposphere and in the
125 UTLS associated with ENSO (Chandra et al., 1998; Ziemke and Chandra, 2003; Nassar et al.,
126 2009; Oman et al., 2011, 2013) and related sea surface temperature and pressure changes. It has
127 long been known that this important mode of climate variability that originates in the Pacific
128 Ocean, with alternating warm (El Niño) and cold (La Niña) phases, leads to disruptions in global
129 circulation patterns, and has impacts on fire and wetland emissions that affect tropospheric
130 composition (Feely et al., 1987; Jones et al., 2001; Sudo and Takahashi, 2001; Duncan et al., 2003;
131 Doherty et al., 2006; Calvo et al., 2010; Voulgarakis et al., 2015; Rowlinson et al., 2019).

132 How do changes in the upper troposphere relate to changes in the lower troposphere, such as
133 changes in emissions? There have not been many such studies in the past, in large part because of
134 the lack of well-sampled long-term data in the upper reaches of the troposphere, where ozone is of
135 radiative significance. While this region is not directly connected to surface pollution, fast
136 convection episodes in the tropics imply that there might well be some correlations between lower
137 tropospheric and upper tropospheric abundances, and even for long-term trends. Long-range
138 transport of pollution can, however, extend into the UT, and also back downward with cross-
139 continental impacts on surface pollution levels. Constraints on chemistry climate models are one
140 important goal for studies of long-term measurements of upper tropospheric composition. Such
141 studies are also expected to contribute to continuing assessments of pollutant trends in the
142 troposphere, such as the Tropospheric Ozone Assessment Report Phase II (TOAR-II), while
143 related model simulations are of interest to continuing assessments of chemistry climate models
144 (e.g., CMIP-7).

145 Tropical upper tropospheric profiles of O₃ and CO have been measured on a continuous daily
146 basis by the Microwave Limb Sounder on the Aura satellite, from a near-polar sun synchronous
147 orbit since late 2004. Here, we present results of trends and variability analyses of these data sets
148 (from 2005–2020), along with a similar treatment of UT O₃ and CO time series from two chemistry
149 climate models, “specified dynamics” versions of the Whole Atmosphere Community Climate
150 Model version 6 (WACCM6) and the Community Atmosphere Model with chemistry (CAM-
151 chem), both of which are configurations of the Community Earth System Model version 2.2
152 (CESM2.2). When using regression fits, as done here, to analyze broad-scale atmospheric time
153 series, one should pay attention to likely drivers (e.g., ENSO) of variability in that region, since a

154 better fitting of such variability can reduce the resulting trend uncertainties. Altogether, we use
155 one WACCM simulation as well as two separate CAM-chem simulations (the latter two having
156 different anthropogenic emission inputs for CO), as described in Sect. 2, where we provide more
157 details about the MLS data and these model simulations. Section 3 focuses on the trend analysis
158 methodology. In Sect. 4, we discuss the analysis results for O₃, and then for CO; we review the
159 UT climatologies for these species and some differences versus model simulations, and discuss
160 results from zonal mean and mapped trend analyses. We also place our results in the context of
161 past analyses. We then finish with some brief conclusions in Section 5.

162 **2 Observations, model simulations, and trend analysis methods**

163 For both MLS and the chemistry climate models, we analyze monthly averaged zonal mean
164 time series as well as monthly-averaged longitude/latitude binned time series. The models have
165 been designed to capture key dynamical and chemical processes well enough to be usefully
166 compared to the observations. We focus on a region that is somewhat below the tropopause, to
167 minimize potential effects from stratosphere-troposphere exchange and to avoid results that might
168 depend more on lower stratospheric rather than tropospheric change.

169 **2.1 Observations**

170 The Aura MLS observational dataset considered here is taken from sixteen full years (2005
171 through 2020) of global composition measurements, with about 3500 vertical profiles per day per
172 measured species. The MLS antenna performs scans of the atmospheric limb ahead of the Aura
173 satellite in its near-polar sun-synchronous orbit. MLS measures daytime and nighttime thermal
174 emission using microwave radiometers operating at frequencies near 118, 190, 240, and 640 GHz;
175 a 2.5 THz module measured OH during the early part of the mission. The 240 GHz radiometer
176 provides the standard O₃ and CO measurements. For an overview of the MLS measurement
177 technique, the reader is referred to Waters et al. (2006). Read et al. (2006) gave a description of
178 the simulated MLS forward model and related spectra. The MLS retrievals (Livesey et al., 2006)
179 use the optimal estimation approach (Rodgers, 2000); there is no assumption of atmospheric
180 homogeneity along the line of sight (see Livesey and Read, 2000), and the retrievals make use of
181 the MLS antenna's views along overlapping tangent rays during consecutive scans of the Earth's

182 limb. The specifics of MLS data characterization and data quality, along with estimated errors and
183 related information can be found in the documentation by Livesey et al. (2022).

184 Here, we have used the latest data version from MLS, labeled version 5.0 or v5. More
185 specifically, we use the binned MLS Level 3 data sets, with a latitude grid that includes the
186 equatorial bin (-2° to $+2^{\circ}$) and the 44 other adjacent 4° -wide bins. In this work, we use monthly
187 mean time series based on zonal averages as well as latitude bands divided into 12 longitude bins.
188 The typical number of MLS profiles in a monthly zonal mean 4° bin is of order 2400, and about
189 200 for each of the 12 mapped (monthly) longitude/latitude bins. Prior to averaging the MLS data,
190 the standard MLS data quality screening criteria (Livesey et al., 2022) have been applied to all the
191 O_3 and CO Level 2 profiles; this screening removes only a very small fraction (typically 1–3%) of
192 the retrieved profiles. In the troposphere and stratosphere, the MLS O_3 retrieval grid is defined by
193 a subset of the pressure levels given by $p(n) = 1000 \times 10^{-n/12}$ hPa, where n is the pressure level index
194 number; for CO, the grid is twice as coarse, meaning that $n/6$ is used as an exponent in the above
195 equation, rather than $n/12$. The bottom recommended levels for the O_3 and CO retrievals are at 261
196 and 215 hPa, respectively. Our tropical analyses will focus on results between 215 and 147 hPa,
197 in order to largely obtain upper tropospheric results, as more influence from the stratosphere occurs
198 as one gets closer to 100 hPa in the tropics. In the upper troposphere, the vertical resolution of the
199 O_3 and CO products is about 3 km and 5 km respectively (Livesey et al., 2022). In this region, the
200 single-profile precision (1σ random uncertainty) is 20–30 ppbv (meaning ~ 35 – 50%) for O_3 and
201 15–20 ppbv (~ 20 – 30%) for CO. For our analyses of monthly MLS averages, the relevant precision
202 for O_3 and CO reduces to ~ 0.5 ppbv ($\sim 1\%$) for 4° zonal means and ~ 2 ppbv ($\sim 4\%$) for the gridded
203 data using 30° longitude by 4° latitude bins. In addition, the methodology used by the MLS team
204 to assess the aggregate effects of estimated errors in various input parameters, coupled with
205 validation results (see Livesey et al., 2022), leads to systematic uncertainty estimates (1σ) of 5–12
206 ppbv (~ 10 – 20%) and 15–25 ppbv (~ 20 – 35%) for tropical upper tropospheric O_3 and CO,
207 respectively.

208 Following validation work on UT MLS O_3 and CO in the early few years since the Aura launch
209 (Livesey et al., 2008), studies of UT MLS O_3 by Livesey et al. (2013) focused on seasonal and
210 interannual variability and comparisons versus ozonesonde data. Despite sampling differences
211 between these measurement systems, the temporal patterns evident in the MLS UT O_3 data were
212 found to be generally well correlated with the *in-situ* data over different low latitude regions.

213 Distinct seasonality was evident in O₃ and CO (as well as MLS-derived ice water content) over
214 South America and South Africa. Other patterns such as the “wave-one” pattern in tropical O₃ (see
215 Thompson et al., 2000, 2003, Wang et al., 2006) and double peaks in O₃ variability over eastern
216 equatorial Africa (with enhancements around May/June and September to November) were
217 discussed; for MLS UT CO, distinct seasonal behavior was found, for example, in the northern
218 hemisphere tropics, over Eastern Asia and across the Pacific (see also Huang et al., 2012). Livesey
219 et al. (2013) and Huang et al. (2014) discussed the connection between emissions from intense
220 fires over Indonesia in 2006 (following the El Niño-related drought) and dramatic concomitant
221 enhancements in UT CO (from MLS data) over this region. This work has been expanded upon in
222 analyses by Park et al. (2013, 2021) of the significant and long-lasting impacts of more recent El
223 Niño-related droughts and wildfires on tropospheric and lower stratospheric CO abundances.

224 Regarding MLS ozone, previous work has shown vertical oscillations in zonal mean MLS
225 UTLS O₃ profiles (e.g., see Livesey et al., 2022). There are also some biases in MLS tropical UT
226 ozone values, which tend to be on the high side (by 10–20%) with respect to ozonesonde data (see
227 Hubert et al., 2016, Fig. 6), but the above issues are systematic in nature. While we think that
228 neither these biases nor the small vertical oscillations (a few % in magnitude in the region of
229 interest here) would play a major role in changing our MLS UT trend results, given the trend
230 uncertainties (discussed later), any time-dependent effect, if it exists, would be quite difficult to
231 characterize, or provide a fix for.

232 We also compare the CO simulations to CO data from Terra/MOPITT, obtained from
233 multispectral retrievals (V9J) Level 3 dry air total column data, or X_{CO} in ppbv (Deeter et al.,
234 2022). The simulated CO values are smoothed by using the MOPITT a priori columns as well as
235 the 10 layers a priori and averaging kernel profiles, as recommended for a quantitative comparison
236 of modelled and MOPITT X_{CO}.

237 **2.2 Model simulations**

238 We use the Whole Atmosphere Community Climate Model version 6 (WACCM6) and the
239 Community Atmosphere Model with Chemistry (CAM-chem), both of which are components of
240 the CESM2.2 (Danabasoglu et al., 2020). WACCM6 uses the “high-top” set of 70 model levels
241 between the surface and the lower thermosphere (~140 km), while CAM-chem uses 32 layers
242 (“low-top”) that stop in the middle of the stratosphere (~40 km). Both configurations run on a

243 horizontal resolution that is 0.95° latitude \times 1.25° longitude and share the same vertical grid in the
244 troposphere, with a vertical resolution in the upper troposphere of about 1.2 km. Both CAM-chem
245 and WACCM6 include the same representations of boundary layer processes, shallow convection,
246 liquid cloud macrophysics, and cloud microphysics (Gettelman et al., 2019). Each model employs
247 the same chemical mechanism processes (labeled TS1). The chemical scheme includes the O_x ,
248 NO_x , HO_x , ClO_x , and BrO_x families, along with CH_4 and its degradation products, as well as
249 primary non-methane hydrocarbons and related oxygenated organic compounds (Emmons et al.,
250 2020). Reaction rates follow the JPL Publication 19-5 recommendation (Burkholder et al., 2019).
251 TS1 includes a total of 231 species and 583 chemical reactions broken down into 150 photolysis
252 reactions, 403 gas-phase reactions, 13 tropospheric, and 17 stratospheric heterogeneous reactions.
253 The photolytic reactions are based on both inline chemical modules and a lookup table approach
254 (Kinnison et al., 2007). Secondary organic aerosols are represented through the Volatility Basis
255 Set approach (Tilmes et al., 2019). Comparisons of oxidants during the Korea–United States Air
256 Quality (KORUS-AQ) experiment in South Korea led to a revision of the heterogeneous aerosol
257 uptake of hydroperoxyl radicals (HO_2) to produce H_2O instead of H_2O_2 and a reduction of the
258 coefficient (γ) from 0.2 to 0.1 (Gaubert et al., 2020).

259 To accurately represent weather conditions as well as the Quasi-Biennial Oscillation (QBO)
260 and to reproduce various modes of middle atmospheric variability, both simulations are run in the
261 ‘specified dynamics’ (SD) mode. The model dynamical constraints are taken from meteorological
262 fields provided by the Modern-Era Retrospective Analysis for Research and Applications version
263 2 or MERRA-2 (Gelaro et al., 2017). Contrary to the previous SD approach, the MERRA-2 fields,
264 here the zonal and meridional winds and temperature, are first regridded to the model horizontal
265 and vertical grids. The model nudging (Davis et al., 2022) is updated at every (30 min) time step
266 using the closest 3-hourly MERRA-2 fields; nudging timescales are set at 6 hours for the CAM-
267 chem simulations and at 12 hours for WACCM6. The 11-year solar cycle variability is taken from
268 the Naval Research Laboratory’s (NRL) solar model, namely the NRL Solar Spectral Irradiance
269 version 2 (NRLSSI2; Coddington et al., 2016). Volcanic SO_2 emissions (used in sulfate aerosol
270 density calculations) are derived for significant volcanic eruptions using the Neely and Schmidt
271 (2016) database updated through the year 2020. The model scenario used here is based on historical
272 forcings (and recent updates) from the Climate Model Intercomparison Project – Phase 6
273 (Meinshausen et al., 2017). The forcings include greenhouse gases (CH_4 , N_2O , and CO_2) and

274 organic halogens. After 2014, the greenhouse gas and organic halogen inputs follow the CMIP6
275 SSP5-8.5 scenario that projects inputs beyond 2014 (O'Neill et al., 2016; Riahi et al., 2017;
276 Meinshausen et al., 2020).

277 The emissions used here are taken from CAMS-GLOB-ANT_v5.1 in the simulation we refer
278 to as CAM-chem-CAMS (CAMS is the Copernicus Atmosphere Monitoring Service) and CAMS-
279 GLOB-ANT_v5.3 in the WACCM simulation (labeled WACCM-CEDS) for all surface
280 anthropogenic emissions (Soulié et al., 2024). CO anthropogenic emissions were found to be too
281 low in South Asia and China (Gaubert et al., 2023), so these emissions were replaced by the
282 Community Emissions Data System (CEDS) v2, presented in McDuffie et al. (2020), for the CAM-
283 chem-CEDS simulation also analyzed here, and for the only WACCM simulation used here. The
284 CO anthropogenic emissions from the aforementioned versions 5.3 and 5.1 are almost identical;
285 version 5.3 only includes updates to shipping emissions for years after 2017. As there are no
286 differences in the NO_x or volatile organic compounds (VOC) emissions in all three simulations,
287 we can exclude a change in CO trends between these simulations as a result of differences in CO
288 chemical formation or sink. Daily biomass burning emissions are obtained from the Quick-Fire
289 Emissions Dataset (QFED) 2.5 (Darmenov and da Silva, 2014) in all three simulations.

290 The lightning NO_x production and its role in ozone formation is reviewed by Verma et al.
291 (2021). This study showed that most lightning activity occurs within deep convective clouds in the
292 tropical and subtropical region. In our study, the emission of NO from lightning is based on the
293 Price parametrization (Price and Rind, 1992; Price et al., 1997). This parameterization
294 is dependent on cloud height, which includes a stronger dependence over land versus ocean
295 (Emmons et al., 2010). The CAM-Chem and WACCM models used here derive tropical (and
296 global) lightning NO_x values of 2.34 (3.23) and 2.78 (4.11) Tg (N) yr⁻¹, respectively (Table 1),
297 with no significant trends over the course of these simulations. These global values are within the
298 generally accepted global range of 3–8 TgN yr⁻¹ for lightning NO emission (Schumann and
299 Huntrieser, 2007).

300 Aircraft emissions from CMIP6 were employed in WACCM6 (see Hoesly et al., 2018). Both
301 CAM-chem simulations use the version 2.1 of CAMS-GLOB-AIR for aircraft emissions described
302 by Soulié et al. (2024). Gaubert et al. (2020, 2023) found that this version of CAM-chem tends to
303 overestimate tropospheric oxidants, such as ozone, hydrogen peroxide, nitric acid, and hydroxyl
304 radical, resulting in a shorter lifetime of tropospheric methane and CO, mainly in the northern

305 hemisphere extra-tropics. Some of the main model characteristics (with a focus on the differences)
306 are summarized in Table 1.

307 In terms of the model run analyses, we follow the same basic approach as for the MLS data.
308 The daily model profiles are first interpolated (as a function of $\log(\text{pressure})$) onto the MLS
309 pressure grid and then binned and averaged to produce the monthly zonal means (on a 4° latitude
310 grid) and gridded data on the same latitude/longitude grid as is described in Sect. 2.1 for MLS. We
311 note also that we do not find much impact on the MLS versus model comparisons if we use a
312 vertically smoothed version of the model profiles, which more properly takes into account the
313 vertical resolution of the MLS observations, as the differences between smoothed and unsmoothed
314 zonal mean values are much smaller than the model biases. For general simplicity, and for the
315 above reasons, we use unsmoothed model values in this work. A more detailed example of
316 smoothed model profile analyses is provided further below, in connection with observed seasonal
317 CO differences between the models and the MLS measurements.

318 **2.3 Trend analysis methods**

319 For both MLS and model time series trend analyses in the upper troposphere, we use the
320 multivariate linear regression (MLR) method discussed as part of similar studies performed by
321 Froidevaux et al. (2019) for the stratosphere. We refer the reader to Appendix (A3) of the above
322 reference for more details on the regression fit model, which includes commonly used functional
323 terms, namely a linear trend, and cosine and sine functions with annual and semi-annual
324 periodicities, to account for these known variabilities in atmospheric composition, with 3- and 4-
325 month periodic components to better fit shorter-term (intra-seasonal) variations, which also helps
326 to reduce the trend error bars. In addition, we include functions describing multi-year variations
327 caused by the QBO (which mostly affects the stratosphere) and by ENSO, which has been tied, for
328 example, to regional droughts and biomass burning events, with related increases in convection
329 and transport of surface pollution into the upper troposphere. The QBO-related equatorial wind
330 dataset is obtained from the publicly available datasets at the Free University of Berlin. ENSO-
331 related data are in the form of a multivariate index, following the initial work of Wolter and Timlin
332 (2011), as updated by Zhang et al. (2019). We have also included a fitted component that follows
333 variations in solar radio flux (at 10.7 cm), based on Canadian solar measurements (Tapping, 2013);
334 this component typically plays a negligible role in our results. For trend uncertainty estimates, as

335 discussed also by Froidevaux et al. (2019, 2022), we use the block bootstrap resampling method
336 (Efron and Tibshirani, 1993), as done by Bourassa et al. (2014) and others in such atmospheric
337 composition analyses. For every fitted time series, we analyze thousands of re-samplings of the fit
338 residuals, with year-long blocks of residual values replaced by residual series from randomly
339 chosen years; twice the standard deviations in these random distributions' trends provide the (2σ)
340 trend uncertainty values that we use as trend error bars throughout this work.

341 **3 Results**

342 **3.1 Tropical UT O₃**

343 **3.1.1 O₃ climatologies**

344 Although this work focuses on variability and underlying trends, we start in Fig. 1 by showing
345 annually-averaged climatological ozone comparisons between MLS, the WACCM-CEDS
346 simulation, and the CAM-chem-CEDS simulation for 2005–2020 at 147 and 215 hPa for low
347 latitudes (4-degree bin centers between 24°S and 24°N); mapped fields and zonal mean line plots
348 are compared in this Figure. At 215 hPa near 20°N and 20°S, the zonal mean O₃ values from both
349 models are ~5–15% lower than the MLS fields; differences of this order are also observed in the
350 mapped fields. The differences reach about -20% in the deep tropics, as the MLS latitudinal
351 gradients are flat in this region, in contrast to the models' more curved behavior, with a minimum
352 at the equator (see panel (k)). The differences observed here are within the MLS systematic
353 uncertainties mentioned in Sect. 2.1 (up to 24 ppbv, 2σ). These two models agree quite well in the
354 UT region as a whole (typically within about 5 ppbv); such a good level of agreement is not too
355 surprising, given that these models are based on a very similar framework, with nearly identical
356 inputs (see Sect. 2.2). At smaller pressures (147 hPa and also for 100 hPa, which is not shown
357 here), the models follow the MLS latitudinal gradients better (see panel (d) for the comparison at
358 147 hPa), as well as the longitudinal features (including the well-known wave-one ozone pattern
359 discussed by Thompson et al., 2000, 2003, Wang et al., 2006, and others). However, the models
360 exhibit a positive average bias versus MLS at these two pressure levels (see panel (e), where the
361 model bias for 147 hPa is about +20%). However, MLS UT O₃ profiles have been found to be
362 biased positively (by about 10–20%) versus averaged tropical ozonesonde profiles (Sect. 2.1).
363 Thus, positive model biases versus MLS ozone in the tropical UT are not likely caused by a

364 significant underestimate by MLS. We note that the positive model biases (at 147 and 100 hPa)
365 occur for all months of the year (not shown here), so this is not caused by a very large bias in some
366 months, that could be partially compensated for by negative model biases in other months.

367 As mentioned previously, we focus on the upper tropospheric region, somewhat removed from
368 the tropopause, with 147 to 215 hPa being the main levels of interest in the analyses below; while
369 the UT average differences between model and MLS are worth noting, this is not a primary concern
370 in terms of the trend comparisons that we focus on here.

371 **3.1.2 O₃ zonal mean trends**

372 Figure S1 gives some time series examples for ozone at 12°N and 12°S at 147 and 215 hPa,
373 with the MLS and modeled (WACCM-CEDS) series and their respective regression fits, along
374 with the fitted trend lines. The linear correlation coefficients listed above each panel provide a
375 measure of how well the chemistry climate model can fit the MLS series variability. The UT O₃
376 WACCM-CEDS trends roughly follow the trends that are obtained from the MLS regression fits.

377 Regarding the ozone trends, we now switch to results from our analyses of the monthly zonal
378 mean MLS and model time series. Figure 2 displays ozone trend results for MLS and the three
379 simulations for 147, 178, and 215 hPa, based on a multiple linear regression analysis of the
380 respective time series from 2005 through 2020. Figure 2 shows that the tropical upper tropospheric
381 MLS ozone trends are generally positive and significant (meaning that a zero trend lies outside the
382 2σ estimate of trend uncertainty). The observed average ozone trends at all three pressure levels
383 lie within about 0.3 to 0.5 % yr⁻¹; the peak average trends occur at 178 hPa. There are fairly small
384 latitudinal differences at 178 and 215 hPa. At 147 hPa, the MLS results indicate ~50% larger trends
385 in the NH tropics than in the SH tropics, although this difference is not significant. The zonal mean
386 MLS ozone trend (averaging the three pressure levels at 147, 178, and 215 hPa) for 2005–2020 in
387 the 20°S–20°N UT region is 0.39 ± 0.28 % yr⁻¹. The error bars here indicate the 2σ trend uncertainty
388 (calculated here as the root mean square of the 2σ trend uncertainties at all three pressure levels in
389 Fig. 2). This tropical UT O₃ trend is equivalent to 0.21 ± 0.15 ppbv yr⁻¹ (based on the annual
390 average tropical UT values of 56 ppbv measured by MLS). The corresponding model O₃ zonal
391 mean trend results obtained here for 2005–2020 have a positive trend, with excellent agreement
392 with MLS from CAM-chem-CEDS (0.38 ± 0.28 % yr⁻¹) and nearly identical results from CAM-
393 chem-CAMS (0.38 ± 0.29 % yr⁻¹). This agreement is also apparent in the latitudinal pattern, with

394 larger trends in the NH than in the SH, even if the error bars are large enough that there is no
395 “statistically significant difference” between the hemispheres. There is also good statistical
396 agreement between the MLS zonal mean ozone trends and the slightly smaller WACCM-CEDS
397 trends ($0.21 \pm 0.23 \text{ \%yr}^{-1}$).

398 We note that statisticians have been working to guide “common practices” regarding
399 statements of “significance”, and one should be sensitive to some of the broad differences that
400 occur even within “formal criteria” (such as 2σ or a p-level of 0.05), which could sometimes be
401 interpreted too strictly (Wasserstein et al., 2019), as pointed out also by Y. Cohen (private
402 communication, 2024). We keep this in mind here, but we also wish to comment on the use of
403 broader latitude bins. Indeed, if broader latitude regions were analyzed for trends, the
404 corresponding trend uncertainties would be reduced, which could make some of the compared
405 trends differ by more than their 2σ error bar variability. However, the trend error reduction in our
406 testing with a 20° -wide latitude bin instead of 4° bins is only 5–10%, so the uncertainties get
407 divided by much less than the square root of the number of bins used. Thus, we do not readily
408 obtain more significant differences in our comparisons by just averaging over broader regions.

409 In Figure 3, the MLS and CAM-chem-CEDS UT O_3 trend sensitivity analysis is repeated for
410 2005–2018, 2005–2019, 2006–2020, and 2007–2020, showing the relative insensitivity of the
411 MLS results to the choice of time period. This is also true for the CAM-chem-CEDS trends in the
412 NH tropics, although there is more ozone trend sensitivity to the time period choice in this model’s
413 results over the SH tropics. The WACCM-CEDS tropical UT ozone trend results versus time
414 period (not shown here) lead to a spread in the SH tropical trends that is about halfway between
415 the small MLS trend spread and the larger CAM-chem-CEDS trend sensitivity shown in Fig. 3.

416 **3.1.3 O_3 mapped trends and variability**

417 We now turn to the mapped tropical UT trends by analyzing subsets of the O_3 fields from MLS
418 and the models, based on monthly mean time series for 2005–2020 in latitude/longitude bins,
419 rather than on zonal means. As mentioned previously, these bins are also 4° wide in latitude, and
420 the longitude bins are 30° wide. The same regression methodology as described previously here is
421 used for each of the binned time series; we focus on the WACCM-CEDS and CAM-chem-CEDS
422 ozone trends, as we have found that the CAM-chem-CAMS and CAM-chem-CEDS results are
423 quite similar, in the case of ozone at least. Figure 4 shows the resulting mapped O_3 trends from

424 MLS and the two models for 147 and 215 hPa (top and bottom rows, respectively), with the maps
425 spanning 26°S to 26°N. Hatched bins indicate trends for which the 2σ uncertainty range
426 encompasses the zero trend value which is often interpreted as a low level of “statistical
427 significance”, although one should be cautious (see the previous Section) regarding the strict
428 application of such a criterion or wording. The largest MLS trends are observed over the
429 Indonesian region and (mostly) to the East of that region, as well as over the northern Atlantic.
430 The mapped trends confirm the overall zonal mean result of slightly larger O₃ trends in MLS than
431 in WACCM-CEDS. Broad regions with positive tendencies are observed in both model trend
432 results; these regions include SouthEast Asia, Indonesia, northern Australia, the Atlantic, and
433 northern Africa, with some, but not exact agreement with the regions mentioned above for the
434 larger MLS trends. At 215 hPa, the slightly larger positive trends in CAM-chem-CEDS than in
435 WACCM-CEDS over the Australian region (bottom right quadrant, south of the equator)
436 contribute to the better correspondence between the zonal mean O₃ trend results (Fig. 2c) between
437 CAM-chem-CEDS and MLS over the southern tropics. The mapped trend discrepancies between
438 the simulations and MLS are rarely outside the 2σ error bar ranges. Nevertheless, some of the
439 discrepancies are worth noting, especially when they cover multiple adjacent bins; in particular,
440 the easternmost longitude band shows MLS trends with (significant) positive values, in contrast to
441 the simulation results, with binned trends that are often small and/or negative.

442 We have compared these mapped ozone trend results to those for tropospheric column ozone
443 (TCO) obtained by Ziemke et al. (2019), using a combination of total O₃ columns from the Aura
444 Ozone Monitoring Instrument (OMI) and MLS-based stratospheric O₃ columns. In Fig. 5, we show
445 in the top two rows the trends from MLS ozone at 178 hPa (top map) versus the bottom map which
446 provides the mapped TCO trends for the same time period, arrived at from appropriate horizontal
447 smoothing of the results obtained following the above reference, to make the MLS and TCO
448 horizontal resolutions comparable; this smoothing comes from an interpolation versus latitude and
449 a weighted averaging in longitude, since the TCO results have finer longitudinal resolution (5°-
450 wide bins) than the MLS longitudinal grid used here (30°-wide bins). Similarities are observed in
451 the longitudinal pattern of UT MLS O₃ and TCO trends, as shown also for 3 different latitude bins
452 in panel (c) of Fig. 5; variations of a factor of two to three are observed, mostly in the northern
453 half, between the western and eastern hemispheres for both sets of trends, which tend to lie between
454 roughly 0.3 and 1.2 % yr⁻¹. However, the agreement between MLS UT O₃ and TCO trends is often

455 worse for other MLS pressure level choices; this can be deduced from panel (d), where R
456 (correlation coefficient) values relating to the longitudinal variations obtained from MLS at
457 different pressures versus the longitudinal variations in TCO are displayed as a function of latitude
458 (y-axis). In fact, one might not expect the MLS ozone UT trends to track the TCO trends very well,
459 given that TCO measures the entire column whereas MLS measures trends in a vertical region
460 about 5 km wide in the upper troposphere, but this was worth looking into. Regional variability
461 and horizontal sampling differences between MLS and OMI will also play a role (see Thompson
462 et al., 2021, for variability aspects of sonde-derived tropospheric trends). Our comparisons imply
463 that the correlation between lower and upper tropospheric ozone trends is not a strict “one-to-one
464 mapping”, but there are nevertheless some similarities between these regions.

465 We have also analyzed the level of explained variance in the regression fits for these binned
466 trend results. Figure 6 shows the square of the correlation coefficient values (R^2) as a function of
467 latitude and longitude for different explanatory variables used in the binned O_3 fits at 147 hPa,
468 based on fit comparisons to the MLS series (top 6 panels), and for the regression fit versus the
469 WACCM-CEDS series (bottom 6 panels). We have ignored the solar component in these plots as
470 it was found to be of negligible importance; we display the remaining contributions, namely the
471 annual, semi-annual, short-term (sum of the 3-month and 4-month terms), QBO, and ENSO terms,
472 as well as the contribution from the full regression fit, which shows that most (but certainly not
473 all) of the time series variance can be explained by such a regression model. The annual term and
474 semi-annual terms can generally explain a large part of the variance, usually followed in
475 importance by the ENSO term, over most of the Pacific. The QBO component is very small in the
476 upper troposphere, even though it is a well-known and large contributor to stratospheric trace gas
477 variability in the lowermost stratosphere. There is also a significant annual cycle in the tropical
478 lowermost stratosphere related to variations in vertical velocities and in the Brewer-Dobson
479 circulation (Randel et al., 2007; Witte et al., 2008). The R^2 patterns observed in the MLS panels
480 are reproduced in a broad sense by the fits to the CCM, as shown in the bottom 6 panels; this is
481 also a result of the close match between the CCM and the MLS O_3 time series, shown earlier in
482 this work. The ENSO model pattern for O_3 does not match the MLS-derived pattern that well over
483 Indonesia, but this comparison is generally better in the Pacific region between -90° and -180° . A
484 somewhat weaker R^2 value in the model simulation also exists in parts of the Eastern hemisphere
485 for the semi-annual term. The combination of these differences helps to explain the somewhat

486 poorer overall fits (and variance contributions) for the model than for MLS. For the most part, it
487 does not matter much which model run is used for these analyses, or even which pressure level is
488 used; indeed, the results at 215 hPa (see Fig. S5) are generally similar to those in Fig. 6.

489 To pursue the ENSO-related patterns further, one can obtain a (mapped) sensitivity coefficient
490 to ENSO from the regression fits regarding this component's importance in ppbv/K (where "K"
491 relates to tropical sea surface temperatures changes). The O₃ ENSO sensitivity is shown in Fig. 7
492 for the 2005–2020 MLS and WACCM-CEDS results at 147 and 215 hPa. This provides more
493 information about the sign of the sensitivity over different regions, and we observe generally
494 positive (negative) sensitivity in the Eastern (Western) hemisphere, for both MLS and WACCM-
495 CEDS cases; moreover, at 147 hPa, there are two strong negative minima on each side of the
496 Equator in the central Pacific region. A positive change (or a negative change) in tropical Pacific
497 sea surface temperatures during El Niño (La Niña) conditions will correlate with ozone increases
498 (decreases) in the regions with positive (negative) sensitivity coefficients. The model results are
499 quite consistent with those from MLS in terms of the ENSO-related sensitivity coefficient patterns
500 and magnitudes, although the model response is often slightly smaller than seen in the MLS result.
501 As we discuss further below, such ozone sensitivity patterns have been described and interpreted
502 before. Figure 16 provides the same analysis, but for the CO sensitivity to ENSO. These maps
503 show a positive CO ENSO sensitivity coefficient throughout the tropics, with local maxima in both
504 the Eastern and Western hemispheres, rather than the O₃ dipole (positive/negative) structure shown
505 in Fig. 7. The model CO ENSO sensitivity broadly matches the MLS results, although it is not as
506 strong; the different patterns in the western hemisphere, compared to the O₃ sensitivity to ENSO,
507 might be caused by differences in O₃ and CO vertical profile gradients in these regions, but this
508 would require further detailed investigations. We also note that, especially in the MLS case, the
509 peak magnitudes of the CO ENSO sensitivity coefficients in Fig. 16 match the peak magnitudes
510 of the positive O₃ ENSO sensitivity in Fig. 7.

511 512 **3.1.4 O₃ discussion** 513

514 We have found some climatological differences between the MLS observations of O₃ in the
515 tropical upper troposphere and the WACCM-CEDS simulation, as well as both CAM-chem
516 simulations. The models underestimate the mean MLS O₃ values at 215 hPa; at 147 hPa, the

517 models are biased high by about 15–25%, and we have no reason to believe that such positive
518 biases result from an average negative bias in the corresponding MLS values.

519 The averaged zonal mean tropical UT O₃ trend from MLS for 2005–2020 is $0.39 \pm 0.28 \text{ \%yr}^{-1}$
520 (or about $0.22 \pm 0.16 \text{ ppbv yr}^{-1}$), where the error bars indicate 2σ uncertainties. We note that the
521 MLS ozone profile trend detection capability lies within the most stable among ozone sounders,
522 based on the satellite and ground-based ozone intercomparison work by Hubert et al. (2016). In
523 addition, differences between stratospheric ozone columns from MLS and the Aura Ozone
524 Monitoring Instrument (OMI) exhibit no significant drift (Ziemke et al., 2019), thus providing
525 added confidence in the temporal stability of both measurement systems; also, we expect a similar
526 level of confidence in the stability of MLS CO, since CO is retrieved using the same radiometer
527 as the MLS standard ozone product. We get excellent agreement with MLS tropical UT zonal
528 mean trends from the CAM-chem-CEDS O₃ zonal mean trends ($0.38 \pm 0.28 \text{ \%yr}^{-1}$) and somewhat
529 poorer agreement from the smaller WACCM-CEDS trends ($0.21 \pm 0.23 \text{ \%yr}^{-1}$). We also show that
530 the zonal mean MLS O₃ tropical UT trend results for different time periods, with start and end
531 years adjusted by 1–2 years, do not significantly depart from the 2005–2020 results; there is more
532 sensitivity to the choice of period in the CAM-chem-CEDS trend results over the southern tropics.

533 In terms of mapped ozone trends, the largest MLS-derived tropical trends (up to $+1.4\% \text{ yr}^{-1}$) are
534 observed over Indonesia and East of that region, as well as over the northern Atlantic region. The
535 mapped model O₃ UT trends broadly match the MLS trends, albeit with somewhat smaller
536 variations. The significant model maxima over Southeast Asia and the North Atlantic are similar
537 to the significant MLS patterns in those regions. More qualitatively, the Indonesian region displays
538 smaller model O₃ trends than those derived from MLS data; parts of the western Pacific region
539 exhibit some negative trends in the MLS and model trends, but not with good spatial correlation.
540 The mapped MLS-based UT O₃ trends and TCO trends for the same period (see Fig. 5), based on
541 the analyses of Ziemke et al. (2019), provide good correlations in parts of the tropics, with similar
542 values and longitudinal patterns; however, the MLS UT O₃ trend maxima over the western Pacific
543 are symmetric about the equator, whereas the TCO maxima in that region are found in the northern
544 part only. **Since the TCO measurement weighting does not favor the UT region, we would not**
545 **necessarily expect a really high correlation versus the MLS UT trends.**

546 There have been large differences between past satellite-based tropospheric O₃ trends (Gaudel
547 et al., 2018). Leventidou et al. (2018) pointed out that tropical tropospheric ozone column trends

548 derived from a combination of European satellite measurements from 1996 to 2015 showed
549 regional increases as large as $1\text{--}2\% \text{yr}^{-1}$, with some negative trends over the oceans, but with
550 significant uncertainties (see also Heue et al., 2016, and Ebojje et al., 2016). The TCO analyses by
551 Ziemke et al. (2019) using combined OMI and MLS ozone columns showed that TCO trends are
552 larger for 2005-2016 than in the two decades before 2005; for 2005–2016, the derived TCO
553 tropical trends are $\sim 0.4\text{--}0.7\% \text{yr}^{-1}$ (see also Gaudel et al., 2020). These two investigations found
554 regional differences in TCO trends, with maxima over India, Southeast Asia, the eastern Pacific
555 region and tropical Atlantic, with near zero or slightly negative TCO trends over the Western
556 Pacific. Similar TCO trends (based on combined OMI and MLS data) were also given by Liu et
557 al. (2022) for the 2005–2018 period.

558 A recent study (Gaudel et al., 2024) of tropical tropospheric ozone trends from several satellite-
559 based and in situ datasets between 1994 and 2019 yields “maximum mid- and upper tropospheric
560 increases above India, Southeast Asia and Malaysia, with values from 3.4 ± 0.8 to 6.8 ± 1.8 ppbv
561 decade^{-1} .” The tropical UT O_3 trend results obtained here from MLS data, converted to the same
562 units, are 2.2 ± 1.6 ppbv decade^{-1} , which is consistent with the above results, considering also that
563 the maximum mapped UT trends obtained here (about $1.4\% \text{yr}^{-1}$) translate to ~ 8 ppbv decade^{-1} .
564 The MLS-derived results for zonal mean tropical UT trends versus latitude are tabulated in Table
565 S1 in both sets of units. The OMI/MLS tropical trends (2004–2021) from the above reference are
566 listed as $2 \pm 5\% \text{decade}^{-1}$ for 0 to 20°S and $3 \pm 2\% \text{decade}^{-1}$ for 0 to 20°N ; these numbers are
567 consistent with the slightly larger UT averages from MLS, which show an increase from $\sim 3\% \text{decade}^{-1}$
568 near 20°S to $\sim 4\% \text{decade}^{-1}$ near 20°N (see Table S1 for more details).

569 Regarding other past O_3 trend results for the upper troposphere, IAGOS-derived trends were
570 previously discussed by Cohen et al. (2018) for the 1994–2013 period, but with an emphasis on
571 the extra-tropics. The IAGOS trend analysis by Gaudel et al. (2020) for 5 tropical regions over
572 1994–2016 gave positive UT trends averaging $\sim 0.6\% \text{yr}^{-1}$, with largest values over Southeast Asia.
573 As mentioned above, the MLS results also show peak ozone trends over this general region. Wang
574 et al. (2022) showed that ozone trends from ozonesonde profiles for a very similar time period
575 agree broadly with IAGOS results, although the sonde spatio-temporal coverage is limited, and
576 there can be significant scatter in trends from various sonde sites. Their non-satellite UT data sets
577 and derived trends are similar to those from Gaudel et al. (2020). Thompson et al. (2021) observed
578 significant seasonal variations in tropical ozonesonde trends (based on data for 1994-2019 from

579 the Southern Hemisphere Additional Ozonesondes, or SHADOZ network); these authors noted
580 that dynamical influences (besides emissions changes) likely play a role in these tropical
581 tropospheric trends, which average $\sim 0.1\text{--}0.4\ \text{yr}^{-1}$ (for annual trends), but with trends in certain
582 regions/seasons (February to May in particular) as large as $1\text{--}2.5\ \text{yr}^{-1}$. While model studies in a
583 recent paper by Ma et al. (2024) also confirm that lower stratospheric O_3 and related dynamical
584 transport effects can significantly impact long-term UT O_3 trends, their results suggest that, for the
585 tropics, the largest influence (of order 60–70% or more) comes from the tropospheric O_3 source.
586 Table 2 provides trend averages and trend ranges from MLS, along with those from two of the
587 above references regarding UT O_3 trends, not including column results or references with
588 redundancy or poorer matches to the MLS period. For tropical tropospheric O_3 column trends, a
589 comprehensive review is given by Gaudel et al. (2024). The trends in Table 2 are consistent with
590 MLS tropical UT trends, which are based on more dense and daily coverage. Given the different
591 periods and tropical sampling patterns between IAGOS and sondes versus MLS, these UT trend
592 comparisons give as reasonable an agreement as one might expect; see also the significant impacts
593 on O_3 trends from in situ sampling limitations mentioned by Gaudel et al. (2024).

594 Zhang et al. (2016) and Wang et al. (2022) have ascribed the positive sign of post-2000 tropical
595 ozone trends to an equatorward redistribution of surface emissions over the years. Moreover, Wang
596 et al. (2022) discussed how increases in aircraft emissions of nitrogen oxides should also have
597 contributed to enhancements in UT ozone. The UT zonal mean model O_3 trends shown in our work
598 are typically larger (by $\sim 30\text{--}50\%$) in the NH tropics than in the SH tropics. This is also true for the
599 model simulation (also from CESM2) provided by Wang et al. (2022); these authors also point out
600 that uncertainties in estimates of ozone precursor emission inventories (including those for volatile
601 organic carbons species, or VOCs) may well contribute to differences between modeled and
602 observational ozone trends. While VOC source strengths might be difficult to invoke as a major
603 source of uncertainty for the tropical regions, other potential model issues (e.g., larger than
604 currently expected uncertainties in lightning-generated ozone in the tropical upper troposphere)
605 may be worth further consideration. We note that there are large differences (a range of a factor of
606 two or more) between the tropospheric ozone burden changes predicted by various global models
607 in the work by Wang et al. (2022). Also, Liu et al. (2022) show that significant regional differences
608 in ozone column trends exist in their model results (using the NASA Goddard Earth Observing

609 System Chemistry Climate Model, GEOSCCM), with near zero trends over the tropical western
610 Pacific; their modeled TCO trend results underestimate the observed positive TCO trends.

611 Regarding ozone UT variability, we found that the annual, semi-annual, and ENSO terms
612 dominate the variability in the tropical upper troposphere. The TCO interannual variability has
613 been known to be heavily influenced by ENSO (Ziemke and Chandra, 2003; Ziemke et al., 2010).
614 Oman et al. (2013) found that the ENSO relationship for ozone could be simulated by a chemical
615 climate model driven by observed SSTs. The observed and matching simulated sensitivity
616 coefficients imply increased downwelling from the stratosphere and suppressed convection during
617 El Niño periods for regions of positive sensitivity (Chandra et al., 1998; Sudo and Takahashi,
618 2001; Oman et al., 2013). The MLS UT ozone variations and their relation to ENSO were
619 discussed by Oman et al. (2013), who showed patterns of ozone sensitivity to ENSO at 147 hPa
620 (their Figure 6) that resemble the ones we produced here (in Fig. 7) from analyses of MLS data
621 over almost twice as long a period.

622 **3.2 Tropical UT CO**

623 **3.2.1 CO climatologies**

624 For CO, a similar set of annual mean climatological plots as those from Fig. 1 is provided in
625 Fig. 8. We observe that the model CO values follow the patterns of the MLS UT CO fields fairly
626 well, and the zonal mean model biases are usually around -10% to -20%; the model biases are
627 most often negative, and more so in the northern tropics at 215 hPa. The model mean CO biases
628 shown in Fig. 8 are well within the MLS CO systematic uncertainties mentioned in Sect. 2.1; the
629 CAM-chem-CEDS climatological UT CO is slightly closer to the MLS UT CO climatology than
630 is the WACCM-CEDS CO climatology. As in the case of ozone, the aforementioned model versus
631 data CO biases are found to exist not only for annual averages, but also on a month-to-month basis.
632 The SPARC Data Initiative report (SPARC, 2017) and the more recent update by Hegglin et al.
633 (2021) showed that MLS CO values in the tropical UT are within about 10–15% of the mean values
634 that include other data from ACE-FTS and the Michelson Interferometer for Passive Atmospheric
635 Sounding (MIPAS). However, the MLS mean values are larger than the multi-instrument mean at
636 100 hPa by about 10–20%, which can account for more than half of the MLS/model bias at this
637 level (not shown here). Also, just considering the theoretical systematic uncertainty estimates
638 provided in Sect. 2.1, it is possible that most (or even all) of the bias between models and MLS at

639 100 hPa is caused by a positive bias in the MLS CO data. However, an earlier WACCM-CEDS
640 version (WACCM4) underestimated CO and other hydrocarbon data in the southern tropical UT,
641 as described by Park et al. (2013); those authors noted that model deficiencies in emission source
642 strengths or in the upward rate of transport could potentially explain these model underestimates.
643 **In summary, while we cannot pin down the exact causes for the mean biases between the UT CO**
644 **climatologies from MLS and the models shown here, a combination of MLS and model systematic**
645 **errors likely provides a reasonable explanation.**

646 **3.2.2 CO zonal mean trends**

647 For CO, the zonal mean time series provided in Fig. S2 show that there are some slight
648 differences in the trends between observed and modeled (WACCM-CEDS) CO, with more
649 negative trends in the MLS series than in the model series. The large variability seen in the MLS
650 CO series shows correlation with WACCM-CEDS (see the large correlation coefficient values, R ,
651 in the 12°S series for 147 and 215 hPa). We know that the largest CO peaks in these time series
652 are tied to surface emissions, convection, and subsequent transport into the upper troposphere and
653 lower stratosphere (UTLS), with a strong connection to El Niño-related droughts and intense fire
654 (biomass burning) events (see, e.g., Schoeberl et al., 2006, Jiang et al., 2007, Liu et al., 2013, Park
655 et al., 2021, Duncan et al., 2003, 2007). **The largest CO peaks in the MLS upper tropospheric**
656 **tropical record have been correlated with El Niño events in late 2006, in 2009–2010, and especially**
657 **from late 2015 into 2016 (see Park et al., 2021, and references therein, for further information).** At
658 12°N, the observed CO variability is somewhat smaller than at 12°S, and the model variability is
659 much more muted, while the model versus MLS phasing agreement is quite poor, especially at
660 215 hPa (where R is very small and the MLS time series annual phase is very poorly matched by
661 the model). We have checked that this poor correlation is not tied to an issue involving the
662 smoothing of model profiles to account for the MLS averaging kernels; indeed, Fig. S3 shows the
663 small relative impact resulting from a smoothed (versus vertically interpolated) model series on
664 the average CO profile at 215 hPa and 12°N, as well as regarding the smoothed time series and its
665 phasing.

666 For the UT CO zonal mean trends, Figure 9 provides results in a similar way to Fig. 2 for ozone,
667 but for just the two MLS CO retrieval levels at 147 and 215 hPa. In contrast to ozone, we can see
668 that the MLS-derived tropical UT CO values have typically decreased from 2005 to 2020; these
669 CO trends display negligible latitude dependence. Using the same approach as for ozone, but based

670 on the Fig. 9 results, we obtain an average MLS-based UT CO trend of $-0.25 \pm 0.30 \text{ \%yr}^{-1}$
671 (equivalent to $-0.20 \pm 0.23 \text{ ppbv yr}^{-1}$). The trends at 215 hPa (-0.16 \%yr^{-1}) are a factor of two
672 smaller than those at 147 hPa (-0.34 \%yr^{-1}), although both of these numbers agree within the (2σ)
673 trend uncertainties of 0.3 \%yr^{-1} ; based on the error bars, the CO trend from MLS at 147 hPa is
674 different from zero, while the corresponding MLS trend at 215 hPa is not. In contrast, the average
675 CAM-chem-CAMS UT CO trend at these levels is $0.22 \pm 0.19 \text{ \% yr}^{-1}$, with little difference
676 between 147 and 215 hPa. The two simulations that use CEDS emissions (WACCM-CEDS and
677 CAM-chem-CEDS) yield smaller trends for CO, namely $0.0 \pm 0.14 \text{ \%yr}^{-1}$, with slightly negative
678 average trends at 147 hPa and slightly positive average trends at 215 hPa. This difference in trends
679 can be explained by significant decreases in Chinese anthropogenic emissions in CEDSv2, despite
680 the increasing anthropogenic tropical CO emissions in both CAMS-GLOB-ANTv5.1 and CEDSv2
681 (see Fig. S4).

682 Furthermore, larger MLS CO abundances in 2020 explain why the MLS CO UT trends are
683 more negative if one stops the analyses in 2018 or 2019, as can be seen from Fig. 10, which is
684 analogous to the ozone trend sensitivity study provided in Fig. 3. Regarding another aspect of CO
685 trend sensitivities, we considered the issue of large peaks in the observed MLS CO time series (see
686 examples in Fig. S2) typically resulting from El Niño related biomass burning events, followed by
687 convective uplift and CO advective transport into the UTLS. If the model has smaller peaks than
688 the MLS data show, it may be that this could explain some differences, or even a change of sign
689 in the trends. This would stand out more if the large peaks occurred close to the beginning or end
690 of the time series. As a sensitivity test, we artificially suppressed the peaks in these series by setting
691 any CO value larger than 2.5 times the (1σ) variability to a value of 1.5 times this variability, and
692 we found the impact on the linear trends to be negligible (well within the error bars shown here).
693 Such a sensitivity study gives added confidence in the robustness of these trends.

694 In Fig. 11, we show the MLS, WACCM-CEDS, and CAM-chem-CEDS climatological mean
695 CO changes over the annual cycle at 215 hPa for 12°N and 12°S , along with the range of variability
696 (twice the standard deviations about the means). The fits from the models to the MLS CO behavior
697 at 12°S are quite good. The MLS CO curves show the two maxima previously observed in seasonal
698 analyses of biomass burning events, with related upward injections of CO and their subsequent
699 transport to the UT being implicated. Based on fire counts from satellite data (see e.g., Duncan et
700 al., 2003, 2007), a March biomass burning maximum has been associated with the northern

701 hemisphere (mainly from Southeast Asia, but also from northern Africa); outflow from the Asian
702 monsoon contributes to the August NH maximum. The September/October maximum arises from
703 the southern hemisphere (Indonesia, Malaysia, Southern Africa, Brazil). We should also note
704 (more broadly) that the climatological double maximum CO structure measured by MLS near
705 215 hPa over the broader (20°S–20°N) tropics is well matched by MIPAS CO zonal means (see
706 SPARC DI, 2017, chapter 4). At 12°N, however, the lack of correlation between the model
707 variations and those deduced from MLS in Fig. 11 appears to stem from the poorly modeled double
708 maximum structure; we also find that these poorer fits occur more generally throughout the
709 northern tropics. The model underestimates the boreal winter buildup of CO (Gaubert et al., 2020;
710 2023), which may explain a poor representation of the northern hemisphere March/April
711 maximum. Also, biomass burning emission biases can vary regionally and this might explain some
712 of the model/data differences, with some regions providing somewhat better comparisons than
713 others. We do not ascribe the larger model/MLS discrepancies at 215 hPa in the northern tropics
714 to an undue influence of the MLS a priori on the retrievals in this region, as the (averaged) a priori
715 MLS values (although not shown in Fig. 11) follow the WACCM-CEDS fields quite well, and the
716 MLS CO retrievals are producing significantly different variations. To explore this hemispherical
717 asymmetry further, we show CO column comparisons between zonal mean time series from
718 MOPITT, CAM-chem-CEDS and WACCM-CEDS in Fig. 12; all CO columns are averaged over
719 the same latitudes (10°N–14°N and 10°S–14°S). We obtain much better agreement in the phasing
720 of these CO column comparisons for 12°N than we do in the model versus MLS CO comparisons
721 at 215 hPa in Fig. 11. This is clearly seen in the time series evolution, as well as in the correlation
722 coefficients shown in both of these Figures, although R is smaller at 12°N than at 12°S in Fig. 12
723 (but still about 0.75 to 0.8). We also look at this issue for the gridded fields and provide R values
724 for the 12°N and 12°S bins in Fig. 13, where we superpose the column CO model results versus
725 MOPITT and the 215 hPa model results versus MLS as a function of longitude. Again, we observe
726 that R is much higher for the CO total columns than for the 215 hPa level, especially so in the
727 northern tropics. The patterns versus longitude indicate that poorer correlations exist over the
728 Atlantic Ocean (just West of the Greenwich meridian) than over land masses. We do not have clear
729 explanations for the exact patterns in Fig. 13, except for the suggestion that regions with strong
730 land convection might show better UT correlations between models and data, while outflow
731 regions (downwind of convection) in the upper troposphere could be more poorly modeled. The

732 models do not follow the observed UT CO seasonal behavior in a narrow UT region of the northern
733 tropics, even if the modeled seasonal total columns compare well to MOPITT columns in that
734 region. More in-depth analysis would be needed to probe whether this might be caused by a poor
735 representation of emissions and/or transport to this region. Alternatively, it might be that currently
736 unaccounted for variations of the MLS vertical averaging kernels could affect the (properly
737 smoothed) model values in the northern hemisphere tropics at 215 hPa, in ways that are somehow
738 significantly different than what we show in Fig. S3; this is highly unlikely, given that the
739 smoothed model plots in this Figure hardly change if we replace the tropical MLS averaging kernel
740 values used in that plot by kernels appropriate for 70°N. Another potential issue might be poorly
741 understood cloud impacts on the 215 hPa MLS retrievals, specifically in the northern hemisphere
742 tropics; although this is speculative, it might be worth exploring in the future.

743 **3.2.3 CO mapped trends and variability**

744 In Fig. 14, we show the mapped CO trend results for MLS and all three simulations (WACCM-
745 CEDS, CAM-chem-CAMS, and CAM-chem-CEDS) at 147 and 215 hPa. As seen above, MLS
746 CO trends in the UT are generally negative, with the more statistically significant result occurring
747 at 147 hPa (where the trends are more negative than at 215 hPa). There is an indication of slightly
748 positive trends over or near western Africa, mainly at 215 hPa, although this is not statistically
749 significant. The binned model results from CAM-chem-CAMS confirm the zonal mean view from
750 this model, with mostly positive trends, in contrast to the generally negative tendencies in the MLS
751 trend results. The average trends (from both pressure levels) based on all grid cells for MLS is
752 -0.25 \%yr^{-1} , as opposed to $+0.24 \text{ \%yr}^{-1}$ obtained from CAM-chem-CAMS. Of note, these values
753 lie well outside twice the standard errors in the means (of 0.1 \%yr^{-1}), although one should
754 understand that there are limitations in the use of such a small error bar, given the existence of
755 correlations in atmospheric variability between the various bins. When the CEDS emissions are
756 used, as done for WACCM-CEDS and CAM-chem-CEDS, there is a general decrease in the UT
757 CO trends, with some small negative values, although the vast majority of the model CO trends
758 obtained here are not statistically different from zero within any given bin. The averaged UT
759 mapped trend for CAM-chem-CEDS is 0.0 \% yr^{-1} , with twice the standard error in the mean also
760 about 0.1 \%yr^{-1} . While the use of the model CEDS emissions does lead to a better model agreement

761 with the gridded MLS UT CO trends, the MLS-derived trends are still, on the whole, more negative
762 than these simulated CO trends.

763 For CO, we repeat in Fig. 15 the explained variance analysis provided in Fig. 6 for O₃. Overall,
764 the full fits explain less of the variability in the CO case, in part because of the large ENSO-related
765 peaks that occur throughout the MLS and WACCM-CEDS records, which the regression model,
766 as designed, can only imperfectly match. Also, there are regions in the southern tropics where the
767 annual cycle in the model is better fit by the regression than in the MLS case, and this translates
768 to a somewhat better overall full fit. For both MLS and model, the semi-annual cycle component
769 shows peaks over the South Atlantic region, which is likely linked to biomass burning in Africa
770 and related CO transport to the UT following convective activity (e.g., Duncan et al., 2007; Park
771 et al., 2013, 2021). As for the ozone case, the QBO-related UT variability in the tropics is very
772 small (as seen from the QBO R² contributions). For both MLS and model representations, the
773 ENSO-related correlation patterns are broadly similar to the ozone case, in that there is larger
774 variance in the more extreme longitudes of both western and eastern sides. As for O₃, there are
775 somewhat smaller variance contributions in the Eastern hemisphere from ENSO and the semi-
776 annual term than in the MLS case. At 215 hPa (see Fig. S6), the ENSO variance contribution is
777 slightly larger than at 147 hPa only in a small number of bins, but the overall ENSO-related
778 patterns are not stronger, as seen also in the CO sensitivity coefficients to ENSO in Figure 16
779 below, which shows only slight differences between the two pressure levels.

780

781 **3.2.4 CO discussion**

782 Regarding the CO climatology, the models underestimate the MLS UT values by up to 20%,
783 and these differences could be readily caused by systematic biases in either MLS or the models,
784 or both. Park et al. (2013) also found that model CO values from a (WACCM4) simulation at
785 147 hPa were smaller than the ACE-FTS (and MLS) CO abundances, especially in the SH sub-
786 tropics; they attributed this to a possible underestimation of surface emissions or transport via deep
787 convection. We note that low biases in simulated tropospheric CO have also been found before at
788 northern latitudes and may arise from various factors, such as underestimated CO emissions, high
789 biases in modeled tropospheric OH (Strode et al., 2016; Gaubert et al., 2023), or issues with
790 simulated CO dry deposition rates (Stein et al., 2014). Based on our model/MLS comparisons of
791 UT CO seasonal changes, we find significantly poorer matches at 215 hPa in the northern tropics

792 than in the southern tropics. The detailed causes of this discrepancy are currently not clear to us,
793 given the better matches (correlation coefficients) we obtain between MOPITT total CO columns
794 and modeled CO columns. Potential causes could include model inaccuracies (possibly related to
795 convection and/or CO emissions and subsequent transport in this fairly narrow latitude region),
796 stratosphere-troposphere exchange, or an alternate explanation having to do with poorly
797 understood limitations of the MLS data in this same region.

798 For the CO trends, the average tropical MLS UT trend is $-0.25 \pm 0.30 \text{ \%yr}^{-1}$, whereas the
799 corresponding trends from CAM-chem-CEDS and WACCM-CEDS are close to zero (0.0 ± 0.14
800 \%yr^{-1}) for this region; these average trend results are statistically in agreement, even if the MLS
801 CO trends tend to generally be more negative than the simulation results. Note, however, that the
802 MLS-derived CO UT trends for 2005–2023 are closer to zero (about $-0.1\% \text{ yr}^{-1}$), as we mention in
803 the Conclusion section, but we have no model simulations (or model trends) for that extended
804 period. The (2005–2020) CAM-chem-CAMS simulations (which use CAMS anthropogenic CO
805 emissions, see sect. 2.2), yield statistically significant positive average tropical UT CO trends
806 ($+0.22 \pm 0.19 \text{ \%yr}^{-1}$). More specifically, these simulated latitude-dependent trends are significantly
807 different from the MLS CO trends in the 12°N – 24°N latitude bins. Larger MLS CO abundances in
808 2020 explain why the MLS CO UT trends are more negative if one stops the analyses in 2018 or
809 2019. The mapped MLS CO trends in the UT are also negative, with the more statistically
810 significant result (stronger negative trends) occurring at 147 hPa.

811 While there have not been any past decades-long trend estimates for CO in the broad tropical
812 UT region, our results yield somewhat smaller rates of decrease than other trends mentioned in the
813 Introduction, for example -0.5 to -2 \%yr^{-1} , based on IAGOS UT data at northern midlatitudes
814 (Cohen et al., 2018). Column CO in the free troposphere has generally shown decreasing trends
815 since the turn of the century, typically between -0.5 and -1.5 \%yr^{-1} , as observed in particular by
816 MOPITT and AIRS (Worden et al., 2013a, Strode et al., 2016; Buchholz et al., 2021; Hedelius et
817 al., 2021); however, these trends are not necessarily expected to agree with UT CO trends, since
818 they represent two different altitude regimes. Liu et al. (2022) presented a recent analysis of
819 MOPITT CO data from 2005–2018, along with tropospheric model comparisons to observed CO
820 and O_3 time series. These authors found (as shown here and described for MLS and ACE-FTS data
821 by Park et al., 2021) that their modeled and observational time series both exhibit large interannual
822 variability, with some of the largest interannual changes driven by El Niño events in 2006 and

823 2015 and related biomass burning and CO enhancements tied to droughts over the Indonesian
824 region (see also Logan et al., 2008; Zhang et al., 2011; Livesey et al., 2013; Worden et al., 2013b;
825 Park et al., 2013; Field et al., 2016). Liu et al. (2022) found that modeled CO column trends over
826 various regions of the globe were generally negative, although a lower latitude region (India)
827 exhibited a positive model trend. Jiang et al. (2017) provide some arguments (and other references)
828 pointing to flat biomass burning emission trends over Africa for the first 10–15 years since the
829 turn of the century. Not including the strong tropical anomaly caused by El Niño in 2015, they
830 infer a negative trend in global biomass burning emissions. Uncertainties in the temporal evolution
831 of OH (a major sink for CO) could also explain model CO trend issues. However, Jiang et al.
832 (2017) implied that changes in global OH abundances could not readily explain global CO
833 decreases, given constraints from methyl chloroform surface data (this species also having OH as
834 a major sink, as discussed by Montzka et al., 2011) and despite large uncertainties in OH,
835 especially during the last decade. Rather, these authors conclude that decreasing CO emissions
836 from anthropogenic and biomass burning sources are the main cause of tropospheric CO decreases,
837 although some regional increasing emission trends do exist. While a systematic model bias cannot
838 readily lead to a significant discrepancy in model trend estimates (in percent per year) versus
839 observations, time-dependent emission biases could (e.g., Gaubert et al., 2023). To first order, the
840 decreasing UT CO tropical trends derived from MLS for 2005–2020 agree with (but tend to be
841 smaller in magnitude than) total column CO trends discussed previously in the literature. As
842 discussed by others, some temporal non-linearity in CO trends may be responsible for some of the
843 differences between past tropospheric CO trend results over different periods.

844 For CO in particular, the temporal variability that MLS has observed in the upper troposphere
845 is difficult to fit completely using standard linear regression, given the existence of short-term
846 variability in the troposphere (e.g., Dunkerton and Crum, 1995; Ziemke et al., 2015), as well as
847 large episodic and somewhat random enhancements in the UT CO abundances. Regarding this CO
848 variability, we note that ACE-FTS UT CO monthly zonal mean time series track those from MLS,
849 as shown by Park et al. (2021); this helps to validate the UT time series and variability from MLS.
850 We find that the CO sensitivity to ENSO is much more spatially uniform in sign than the O₃
851 sensitivity; UT O₃ generally increases toward the tropopause while CO decreases, leading to
852 opposite sensitivities to increased upwelling phase over the Pacific (Figs. 7 and 16). In some
853 regions, the CO sensitivity has the same sign as for ozone, and in other regions, it differs;

854 moreover, the model's UT CO sensitivity coefficient to ENSO seems to broadly match the
855 observational sensitivity from MLS, as it shows positive values throughout the tropics. These
856 different behaviors between tropical UT O₃ and CO seem to mainly reflect a stronger (and positive)
857 sensitivity to biomass burning events in the case of CO.

858 **5 Conclusions**

859 We have analyzed tropical ozone (O₃) and carbon monoxide (CO) distributions in the upper
860 troposphere (UT) and their temporal changes for 2005–2020 using Aura Microwave Limb Sounder
861 (MLS) observations and chemistry climate model simulations. Upper tropospheric trends and
862 variability diagnostics were obtained from multiple linear regression analyses.

863

864 ***Tropical UT O₃:***

865 We have compared the model and MLS annual ozone climatologies, focusing on the 147 hPa
866 and 215 hPa pressure levels; the model abundances are typically ~5–15% smaller than MLS O₃ at
867 215 hPa, but larger than the MLS values at 147 hPa by ~20%. MLS O₃ has an averaged UT zonal
868 mean trend at 20°S–20°N of $+0.39 \pm 0.28$ %yr⁻¹. We obtain excellent agreement with the above
869 result from the (averaged) CAM-chem-CEDS O₃ zonal mean trends (0.38 ± 0.28 %yr⁻¹) and
870 somewhat poorer agreement from the smaller WACCM-CEDS trends (0.21 ± 0.23 %yr⁻¹). **We**
871 **note that the MLS tropical UT zonal mean O₃ trends for 2005–2023 are 0.34 ± 0.22 %yr⁻¹, so these**
872 **trends have only changed by a small amount versus the 2005–2020 results; it is useful that the**
873 **trend error bars are reduced by about 23% for the analysis using 3 more years (the same holds for**
874 **the CO 2005–2023 trends mentioned below). However, we cannot readily update any of the model**
875 **simulations (and related trend comparisons) with more analysis years at the time of this writing.**

876 Our analyses for various latitude/longitude bins produce positive mapped O₃ trends of up to
877 1.4 %yr⁻¹ over Indonesia and East of that region, as well as over tropical Africa and the tropical
878 Atlantic. Positive tropical UT mapped O₃ trends are generally captured by the model simulations,
879 although in a more muted way. We find broad similarities (and some differences) between the
880 mapped MLS UT O₃ trends and corresponding mapped trends of tropospheric column ozone for
881 the same time period.

882

883

884 ***Tropical UT CO:***

885 The model climatologies generally show an underestimate versus the MLS CO climatology,
886 with model average biases usually about -10% to -20%. Also, in the northern hemisphere tropics,
887 we find significantly poorer model fits to the observed phasing of CO seasonal changes at 215 hPa
888 than at 147 hPa. This discrepancy is much smaller for the comparison of modeled and
889 Measurements of Pollution in the Troposphere (MOPITT) V9J CO columns. The MLS zonal mean
890 CO UT trend is $-0.25 \pm 0.30 \text{ \%yr}^{-1}$, while the corresponding model CO trends are close to zero
891 ($0.0 \pm 0.14 \text{ \%yr}^{-1}$) when the anthropogenic emissions used in CAM-chem and WACCM are taken
892 from Community Emissions Data System (CEDS) version 2. The non-CEDS version of CAM-
893 chem (the CAM-chem-CAMS simulation) yields averaged CO UT trends of $0.22 \pm 0.19 \text{ \%yr}^{-1}$, in
894 contrast to the negative tendencies prevalent in the MLS CO trends throughout the tropics. These
895 three average CO trend results agree within the limits of the (2σ) error bars provided above,
896 although the model versus MLS agreement is more marginal when non-CEDS CO emissions are
897 used. We note that the MLS tropical UT CO trends for 2005–2023 are $-0.09 \pm 0.23 \text{ \%yr}^{-1}$, so these
898 trends have changed by somewhat more than the ozone trend results and are closer to zero than
899 the 2005–2020 MLS CO UT trends. Unfortunately, the coming end of the MLS data record will
900 soon make such MLS updates impossible. As we noted for O₃, we cannot readily update any of
901 the model simulations (and related trend comparisons) with more analysis years.

902 The negative MLS tropical UT CO trends for 2005–2020 agree with (but tend to be smaller in
903 magnitude than) previously published total column CO trends, although one does not expect
904 complete agreement between UT and column trends. We also find that the sensitivity of UT CO
905 to El Niño / Southern Oscillation (ENSO) is positive at all tropical longitudes, in contrast to the
906 (well-known) dipolar longitudinal structure that exists for the UT O₃ ENSO sensitivity.

907

908 The MLS-derived upper tropospheric tropical trends in O₃ and CO arise from a well-sampled
909 multi-year data set, with the results showing a first-order correlation to large-scale changes in
910 lower tropospheric composition (O₃ increases and CO decreases). We find that there are broad
911 similarities (and a few differences) between the measured UT trends and corresponding results
912 from model simulations, which incorporate state-of-the-art representations of the complex
913 interplay between emissions, photochemistry, convection, and transport in the upper troposphere

914 and lower stratosphere. These results will contribute to the continuing assessments of tropospheric
915 evolution, in particular the large community efforts regarding TOAR-II and CMIP-7.

916 Changes in O₃ precursor emissions have been implicated previously as a driver for global
917 tropospheric O₃ changes (e.g., long-term increases), while decreasing CO emissions from
918 anthropogenic and biomass burning sources have been suggested as the main causes of recent
919 decreases in tropospheric CO. We believe that further investigations into how well different
920 models of O₃ and CO in the tropical UT match the corresponding MLS UT trends are warranted,
921 to provide better understanding of differences between models. There may still be adjustments to
922 make to the models regarding the assumed CO surface emissions, convection, and/or transport-
923 related issues, even though such studies are beyond the scope of this paper. Indeed, biomass
924 burning from Africa or South America and emissions from Asia, followed by transport, can (and
925 will continue to) influence the tropical upper tropospheric abundances of CO and O₃ (e.g.,
926 Tsvilidou et al., 2023). On a longer timescale, the troposphere is a region where the relative
927 importance of multiple factors might change over the multi-decadal timescale of climate change;
928 also, longer-term projections from (free running) models may not be representative of changes
929 from a particular decade or two (see Fiore et al., 2022, regarding model ensemble projections). For
930 example, long-term positive trends in the influx of ozone from the stratosphere to the troposphere
931 may be expected as a result of climate change (Meul et al., 2018), probably with more of an
932 influence on the extra-tropical upper troposphere. Regarding the tropics, Stevenson et al. (2013)
933 showed that a number of chemistry climate model simulations of climate change scenarios yielded
934 long-term ozone decreases in the lower troposphere as a result of enhancements in water vapor
935 (implying more ozone destruction), but low latitude upper tropospheric ozone could be expected
936 to rise, following increased production from lightning. Obtaining accurate enough observations of
937 large-scale tropospheric composition change over the long-term is expected to represent a
938 continuing, but worthy challenge.

939

940 **Data availability.**

941 The MLS data files analyzed here come from the MLS Level 3 data sets (zonal mean and gridded
942 quantities), which are publicly available from the Goddard Earth Sciences Data and Information Services
943 Center (GES DISC) at <https://earthdata.nasa.gov/eosdis/daacs/gesdisc>.
944 The MOPITT Version 9 products are available from NASA through the Earthdata portal
945 (<https://earthdata.nasa.gov/>; https://asdc.larc.nasa.gov/project/MOPITT/MOP03JM_9; or directly from the

946 ASDC archive (<https://asdc.larc.nasa.gov/data/MOPITT/>). We used the following site,
947 ftp://ftp.seismo.nrcan.gc.ca/spaceweather/solar_flux/monthly_averages/solflux_monthly_average.txt to
948 obtain monthly means of the Canadian F10.7 solar flux measurements (Tapping, 2013); these series (see
949 <http://www.spaceweather.gc.ca>) were included in our regression fits. The QBO-related equatorial wind
950 monthly time series were obtained from the public website at [https://www.geo.fu-](https://www.geo.fu-berlin.de/en/met/ag/strat/produkte/qbo)
951 [berlin.de/en/met/ag/strat/produkte/qbo](https://www.geo.fu-berlin.de/en/met/ag/strat/produkte/qbo). The multivariate ENSO index dataset was obtained from the NOAA
952 Physical Sciences Laboratory website at <https://www.psl.noaa.gov/enso/mei/> (Wolter and Timlin, 2011;
953 Zhang et al., 2019). OMI/MLS tropospheric ozone data were obtained from the NASA satellite tropospheric
954 ozone webpage https://acd-ext.gsfc.nasa.gov/Data_services/cloud_slice/.

955

956 **Supplement.** Supplementary material is included as a separate file.

957

958 **Author contributions.** LF analyzed the MLS and model data for trends and variability, and prepared the
959 manuscript, along with contributions from all co-authors. DEK, CGB, and BG provided inputs for running
960 the model runs, as well as properly averaged and formatted outputs from the model, as well as pertinent
961 model-related comments and interpretation of results. JRZ provided TCO datasets and comments on the
962 manuscript. NJL, MJS, WGR, and others on the MLS team provided analyses and expertise to enable the
963 production of the Aura MLS data sets; NJL, MJS, and WGR also provided comments on the manuscript;
964 RAF provided programming assistance for the creation of the MLS data sets and for storage and analyses
965 of the MLS and model files.

966

967 **Competing interests.** The authors declare that they have no conflict of interest.

968

969 **Acknowledgments.** We are thankful to the whole MLS team (past and present) for their contributions over
970 the years to the MLS instrument, data, processing, and database management. We very much acknowledge
971 the referees, who helped improve the initial manuscript with quite a list of useful and detailed comments.
972 We acknowledge the encouragement from Owen Cooper and Helen Worden to link our paper to the
973 TOAR-II Copernicus special issue; thanks also to Kai-Lan Chang for briefly reviewing aspects of our
974 statistical approach regarding the guidelines adopted for reporting TOAR-linked results. WACCM-CEDS
975 is a component of the CESM, supported by the National Science Foundation (NSF). We acknowledge high-
976 performance computing support from Cheyenne (doi:10.5065/D6RX99HX) provided by NCAR's
977 Computational and Information Systems Laboratory, sponsored by the NSF. F10.7 data collection and
978 dissemination are supported by the National Research Council of Canada, with the participation of Natural
979 Resources Canada and support by the Canadian Space Agency. Work at the Jet Propulsion Laboratory,

980 California Institute of Technology, was performed under contract with the National Aeronautics and Space
981 Administration (80NM0018D0004). Copyright 2024. All rights reserved.

982

983 **Financial support.** LF and RAF were funded by the NASA Atmospheric Composition Modeling and
984 Analysis Program (ACMAP). NJL, MJS, and WGR (as well as LF) were supported by the Aura Microwave
985 Limb Sounder project. DEK, BG, and CGB were funded separately by NASA and NSF grants. Part of this
986 material is based upon work supported by the NSF National Center for Atmospheric Research, which is a
987 major facility sponsored by the U.S. National Science Foundation under Cooperative Agreement No.
988 1852977. The NSF NCAR MOPITT project is supported by the National Aeronautics and Space
989 Administration (NASA) Earth Observing System (EOS) program.

990 **References**

- 991 Andela, N., Morton, D. C., Giglio, L., Chen, Y., van der Werf, G. R., Kasibhatla, P. S., DeFries, R. S., Collatz, G. J.,
992 Hantson, S., Kloster, S., Bachelet, D., Forrest, M., Lasslop, G., Li, F., Mangeon, S., Melton, J. R., Yue, C., and
993 Randerson, J. T.: A human-driven decline in global burned area, *Science*, 356(6345):1356-1362, doi:
994 10.1126/science.aal4108, 2017.
- 995 Bouarar, I., Gaubert, B., Brasseur, G. P., Steinbrecht, W., Doumbia, T., Tilmes, S., et al.: Ozone anomalies in the free
996 troposphere during the COVID-19 pandemic, *Geophys. Res. Lett.*, 48, e2021GL094204.
997 <https://doi.org/10.1029/2021GL094204>, 2021.
- 998 Bourassa, A. E., Degenstein, D. A., Randel, W. J., Zawodny, J. M., Kyrölä, E., McLinden, C. A., Sioris, C. E., and
999 Roth, C. Z.: Trends in stratospheric ozone derived from merged SAGE II and Odin-OSIRIS satellite observations,
1000 *Atmos. Chem. Phys.*, 14, 6983-6994, <https://doi.org/10.5194/acp-14-6983-2014>, 2014.
- 1001 Brasseur, G. P., Gupta, M., Anderson, B. E., Balasubramanian, S., Barrett, S., Duda, D., Fleming, G., Forster, P. M.,
1002 Fuglestvedt, J., Gettelman, A., Halthore, R. N., Jacob, D., Jacobson, M. Z., Khodayari, A., Liou, K.-N., Lund, M.
1003 T., Miake-Lye, R. C., Minnis, P., Olsen, S., Penner, J. E., Prinn, R., Schumann, U., Selkirk, H. B., Sokolov, A.,
1004 Unger, N., Wolfe, P., Wong, H.-W., Wuebbles, D. W., Yi, B., Yang, P., and Zhou, C.: Impact of aviation on
1005 climate, FAA's Aviation Climate Change Research Initiative (ACCRI) Phase II, *Bull. Amer. Met. Soc.*,
1006 10.1175/BAMS-D-13-00089.1, 2016.
- 1007 Buchholz, B. R., Worden H. M., et al.: Air pollution trends measured from Terra: CO and AOD over industrial, fire-
1008 prone, and background regions, *Remote Sensing of Environment*, 256, 112275,
1009 <https://doi.org/10.1016/j.rse.2020.112275>, 2021.
- 1010 Burkholder, J. B., Sander, S. P., Abbatt, J. P. D., Barker, J. R., Cappa, C., Crouse, J. D., Dibble, T. S., Huie, R. E.,
1011 Kolb, C. E., Kurylo, M. J., Orkin, V. L., Percival, C. J., Wilmouth, D. M., and Wine, P. H.: Chemical kinetics and
1012 photochemical data for use in atmospheric studies, Evaluation No. 19, JPL Publication 19-5, Jet Propulsion
1013 Laboratory, California Institute of Technology, Pasadena, <http://jpldataeval.jpl.nasa.gov> (last access: 1 March
1014 2022), 2019.
- 1015 Calvo, N., Garcia, R. R., Randel, W. J., and Marsh, D.: Dynamical mechanism for the increase in tropical upwelling
1016 in the lowermost tropical stratosphere during warm ENSO events, *J. Atmos. Sci.*, 67, 2331–2340,
1017 <https://doi.org/10.1175/2010JAS3433.1>, 2010.
- 1018 Chandra, S., Ziemke, J. R., Min, W., and Read, W. G.: Effects of 1997–1998 El Niño on tropospheric ozone and water
1019 vapor, *Geophys. Res. Lett.*, 25(20), 3867– 3870, <https://doi.org/10.1029/98GL02695>, 1998.
- 1020 Coddington, O., Lean, J., Pilewskie, P., Snow, M., and Lindholm, D.: A solar irradiance climate data record, *Bull.*
1021 *Amer. Meteor. Soc.*, <https://doi.org/10.1175/BAMS-D-14-00265.1>, 2016.
- 1022 Cohen, Y., Petetin, H., Thouret, V., Marécal, V., Josse, B., Clark, H., Sauvage, B., Fontaine, A., Athier, G., Blot, R.,
1023 Boulanger, D., Cousin, J.-M., and Nédélec, P.: Climatology and long-term evolution of ozone and carbon
1024 monoxide in the upper troposphere–lower stratosphere (UTLS) at northern midlatitudes, as seen by IAGOS from
1025 1995 to 2013, *Atmos. Chem. Phys.*, 18, 5415–5453, <https://doi.org/10.5194/acp-18-5415-2018>, 2018.

1026 Collins, W. J., Derwent, R. G., Garnier, B., C. E. Johnson, C. E., Sanderson, M. G., and Stevenson, D. S.: Effect of
1027 stratosphere-troposphere exchange on the future tropospheric ozone trend, *J. Geophys. Res.*, 108, D12, 8528,
1028 <https://doi.org/10.1029/2002JD002617>, 2003.

1029 Cooper, O. R., Parrish, D. D., Ziemke, J. R., Balashov, N. V., Cupeiro, M., Galbally, I., Gilge, S., Horowitz, L., Jensen,
1030 N. R., Lamarque, J.-F., Naik, V., Oltmans, S. J., Schwab, J., Shindell, D. T., Thompson, A. M., Thouret, V., Wang,
1031 Y., and Zbinden, R. M.: Global distribution and trends of tropospheric ozone: An observation-based review,
1032 *Elementa*, 2, 000029, <https://doi.org/10.12952/journal.elementa.000029>, 2014.

1033 Crutzen, P. J.: A discussion of the chemistry of some minor constituents in stratosphere and troposphere, *Pure Appl.*
1034 *Geophys.*, 106, 1385–1399, <https://doi.org/10.1007/BF00881092>, 1973.

1035 Crutzen, P. J., and Andreae, M. O.: Biomass burning in the tropics: Impact on atmospheric chemistry and
1036 biogeochemical cycles, *Science*, 250, 1669–1678, <https://doi.org/10.1126/science.250.4988.1669>, 1990.

1037 Danabasoglu, G., Lamarque, J.-F., Bacmeister, J., Bailey, D. A., DuVivier, A. K., Edwards, J., Emmons, L. K.,
1038 Fasullo, J., Garcia, R., Gettelman, A., Hannay, C., Holland, M. M., Large, W. G., Lauritzen, P. H., Lawrence, D.
1039 M., Lenaerts, J. T. M., Lindsay, K., Lipscomb, W. H., Mills, M. J., Neale, R., Oleson, K. W., Otto-Bliesner, B.,
1040 Phillips, A. S., Sacks, W., Tilmes, S., van Kampenhout, L., Vertenstein, M., Bertini, A., Dennis, J., Deser, C.,
1041 Fischer, C., Fox-Kemper, B., Kay, J. E., Kinnison, D. E., Kushner, P. J., Larson, V. E., Long, M. C.,
1042 Mickelson, S., Moore, J. K., Nienhouse, E., Polvani, L., Rasch, P. J., and Strand, W. G.: The Community Earth
1043 System Model Version 2 (CESM2), *J. Adv. in Modeling Earth Systems*, 12,
1044 <https://doi.org/10.1029/2019MS001916>, 2020.

1045 Darnenov, A., and da Silva, A. M.: The Quick Fire Emissions Dataset (QFED) - Documentation of versions 2.1, 2.2
1046 and 2.4, NASA/TM–2015–104606, 2015;38:183, <http://gmao.gsfc.nasa.gov/pubs/tm/>, 2014.

1047 Davis, N. A., Callaghan, P., Simpson, I. R., and Tilmes, S.: Specified dynamics scheme impacts on wave-mean flow
1048 dynamics, convection, and tracer transport in CESM2 (WACCM6), *Atmos. Chem. Phys.*, 22, 197–
1049 214, <https://doi.org/10.5194/acp-22-197-2022>, 2022.

1050 Deeter, M., Francis, G., Gille, J., Mao, D., Martínez-Alonso, S., Worden, H., Ziskin, D., Drummond, J., Commane,
1051 R., Diskin, G., and McKain, K.: The MOPITT Version 9 CO product: sampling enhancements and validation,
1052 *Atmos. Meas. Tech.*, 15, 2325–2344, <https://doi.org/10.5194/amt-15-2325-2022>, 2022.

1053 Doherty, R. M., Stevenson, D. S., Johnson, C. E., Collins, W. J., and Sanderson, M. G.: Tropospheric ozone and El
1054 Niño–Southern Oscillation: Influence of atmospheric dynamics, biomass burning emissions, and future climate
1055 change, *J. Geophys. Res.-Atmos.*, 111, D19304, <https://doi.org/10.1029/2005JD006849>, 2006.

1056 Duncan, B. N., Martin, R. V., Staudt, A. C., Yevich, R., and Logan, J. A.: Interannual and seasonal variability of
1057 biomass burning emissions constrained by satellite observations, *J. Geophys. Res.-Atmos.*, 108, 4100,
1058 <https://doi.org/10.1029/2002jd002378>, 2003.

1059 Duncan, B. N., Strahan, S. E., Yoshida, Y., Steenrod, S. D., and Livesey, N.: Model study of the cross-tropopause
1060 transport of biomass burning pollution, *Atmos. Chem. Phys.*, 7, 3713–3736, [https://doi.org/10.5194/acp-7-3713-](https://doi.org/10.5194/acp-7-3713-2007)
1061 [2007](https://doi.org/10.5194/acp-7-3713-2007), 2007.

1062 Dunkerton, T. J., and Crum, F. X.: Eastward propagating eastward ~2- to 15-day equatorial convection and its relation
1063 to the tropical intraseasonal oscillation, *J. Geophys. Res.*, 100, D12, 25781–25790,
1064 <http://dx.doi.org/10.1029/95JD02678>, 1995.

1065 Ebojje, F., Burrows, J. P., Gebhardt, C., Ladstter-Weienmayer, A., von Savigny, C., Rozanov, A., Weber, M., and
1066 Bovensmann, H.: Global tropospheric ozone variations from 2003 to 2011 as seen by SCIAMACHY, *Atmos.*
1067 *Chem. Phys.*, 16, 417–436, <https://doi.org/10.5194/acp-16-417-2016>, 2016.

1068 Efron, B., and Tibshirani, R.: *An Introduction to the Bootstrap*, Monographs on Statistics and Applied Probability 57,
1069 Chapman and Hall, 1993.

1070 Emmons, L. K., Walters, S., Hess, P. G., Lamarque, J. F., Pfister, G. G., Fillmore, D., Granier, C. Guenther, A.
1071 Kinnison, D., Laepple, T., Orlando J., Tie, X., Tyndall, G., Wiedinmyer, C., Baughcum S. L., and Kloster,
1072 S.: Description and evaluation of the Model for Ozone and Related chemical Tracers, version 4 (MOZART-
1073 4). *Geoscientific Model Development*, 3(1), 43-67. <https://doi.org/10.5194/gmd-3-43-2010>.

1074 Emmons, L. K., Schwantes, R. H., Orlando, J. J., Tyndall, G., Kinnison, D., Lamarque, J.-F., Marsh, D., Mills, M. J.,
1075 Tilmes, S., Bardeen, C., Buchholz, R. R., Conley, A., Gettelman, A., Garcia, R., Simpson, I., Blake, D. R.,
1076 Meinardi, S., and Pétron, G.: The Chemistry Mechanism in the Community Earth System Model version 2
1077 (CESM2), *Journal of Advances in Modeling Earth Systems*, 12, <https://doi.org/10.1029/2019MS001882>, 2020.

1078 Feely, R. A., Gammon, R. H., Taft, B. A., Pullen, P. E., Waterman, L. S., Conway, T. J., Gendron, J. F., and
1079 Wisegarver, D. P.: Distribution of chemical tracers in the eastern equatorial Pacific during and after the 1982–
1080 1983 El Niño/Southern Oscillation Event, *J. Geophys. Res.-Oceans*, 92, 6545–6558,
1081 <https://doi.org/10.1029/JC092iC06p06545>, 1987.

1082 Field, R. D., van der Werf, G. R., Fanin, T., Fetzer, E. J., Fuller, R., Jethva, H., Levy, R., Livesey, N. J., Luo, M.,
1083 Torres, O., and Worden, H. M.: Indonesian fire activity and smoke pollution in 2015 show persistent nonlinear
1084 sensitivity to El Niño-induced drought, *Proceedings of the National Academy of Sciences of the United States of*
1085 *America*, 113, 9204–9209, <https://doi.org/10.1073/pnas.1524888113>, 2016.

1086 Fiore, A. M., Hancock, S. E., Lamarque, J.-F., Correa, G. P., Chang, K.-L., Ru, M., Cooper, O., Gaudel, A., Polvani,
1087 L. M., Sauvage, B., and Ziemke, J. R.: Understanding recent tropospheric ozone trends in the context of large
1088 internal variability: a new perspective from chemistry-climate model ensembles, *Environ. Res.: Climate* 1 (2022)
1089 025008, <https://doi.org/10.1088/2752-5295/ac9cc2>, 2022.

1090 Froidevaux, L., Kinnison, D. E., Wang, R., Anderson, J., and Fuller, R. A.: Evaluation of CESM1 (WACCM) free-
1091 running and specified dynamics atmospheric composition simulations using global multispecies satellite data
1092 records, *Atmos. Chem. Phys.*, 19, 4783–4821, <https://doi.org/10.5194/acp-19-4783-2019>, 2019.

1093 Froidevaux, L., Kinnison, D. E., Santee, M. L., Millán, L. F., Livesey, N. J., Read, W. G., Bardeen, C. G., Orlando, J.
1094 J., and Fuller, R. A.: Upper stratospheric ClO and HOCl trends (2005–2020): Aura Microwave Limb Sounder and
1095 model results, *Atmos. Chem. Phys.*, 22, 4779–4799, <https://doi.org/10.5194/acp-22-4779-2022>, 2022.

1096 Gaubert, B., Worden, H. M., Arellano, A. F. J., Emmons, L. K., Tilmes, S., Barré, J., Martínez Alonso, S., Vitt, F.,
1097 Anderson, J. L., Alkemade, F., Houweling, S., and Edwards, D. P.: Chemical feedback from decreasing carbon
1098 monoxide emissions, *Geophys. Res. Lett.*, 44, 9985–9995, <https://doi.org/10.1002/2017GL074987>, 2017.

1099 Gaubert, B., Emmons, L. K., Raeder, K., Tilmes, S., Miyazaki, K., Arellano Jr., A. F., Elguindi, N., Granier, C., Tang,
1100 W., Barré, J., Worden, H. M., Buchholz, R. R., Edwards, D. P., Franke, P., Anderson, J. L., Saunio, M., Schroeder,
1101 J., Woo, J.-H., Simpson, I. J., Blake, D. R., Meinardi, S., Wennberg, P. O., Crouse, J., Teng, A., Kim, M.,
1102 Dickerson, R. R., He, H., Ren, X., Pusede, S. E., and Diskin, G. S.: Correcting model biases of CO in East Asia:
1103 impact on oxidant distributions during KORUS-AQ, *Atmos. Chem. Phys.*, 20, 14617–14647,
1104 <https://doi.org/10.5194/acp-20-14617-2020>, 2020.

1105 Gaubert, B., Edwards, D. P., Anderson, J. L., Arellano, A.F., Barré, J., Buchholz, R.R., Darras, S., Emmons, L.K.,
1106 Fillmore, D., Granier, C., et al.: Global Scale Inversions from MOPITT CO and MODIS AOD, *Remote Sens.* 15,
1107 4813, <https://doi.org/10.3390/rs15194813>, 2023.

1108 Gaudel, A., Cooper, O. R., Ancellet, G., Barret, B., Boynard, A., Burrows, J. P., Clerbaux, C., Coheur, P. F., Cuesta,
1109 J., Cuevas, E., Doniki, S., Dufour, G., Ebojje, F., Foret, G., Garcia, O., Granados-Muñoz, M. J., Hannigan, J. W.,
1110 Hase, F., Hassler, B., Huang, G., Hurtmans, D., Jaffe, D., Jones, N., Kalabokas, P., Kerridge, B., Kulawik, S.,
1111 Latter, B., Leblanc, T., Le Flochmoën, E., Lin, W., Liu, J., Liu, X., Mahieu, E., McClure-Begley, A., Neu, J. L.,
1112 Osman, M., Palm, M., Petetin, H., Petropavlovskikh, I., Querel, R., Rahpoe, N., Rozanov, A., Schultz, M. G.,
1113 Schwab, J., Siddans, R., Smale, D., Steinbacher, M., Tanimoto, H., Tarasick, D. W., Thouret, V., Thompson, A.
1114 M., Trickl, T., Weatherhead, E., Wespes, C., Worden, H. M., Vigouroux, C., Xu, X., Zeng, G., and Ziemke, J.:
1115 Tropospheric Ozone Assessment Report: Present-day distribution and trends of tropospheric ozone relevant to
1116 climate and global atmospheric chemistry model evaluation, *Elem. Sci. Anth.*, 6, 39,
1117 <https://doi.org/10.1525/elementa.291>, 2018.

1118 Gaudel, A., Cooper, O. R., Chang, K.-L., Bourgeois, I., Ziemke, J. R., Strode, S. A., Oman, L. D., Sellitto, P., Nédélec,
1119 P., Blot, R., Thouret, V., and Granier, C.: Aircraft observations since the 1990s reveal increases of tropospheric
1120 ozone at multiple locations across the Northern Hemisphere, *Sci. Adv.*, 6, eaba8272,
1121 <https://doi.org/10.1126/sciadv.aba8272>, 2020.

1122 Gaudel, A., Bourgeois, I., Li, M., Chang, K.-L., Ziemke, J., Sauvage, B., Stauffer, R. M., Thompson, A. M., Kollonige,
1123 D. E., Smith, N., Hubert, D., Keppens, A., Cuesta, J., Heue, K.-P., Veffkind, P., Aikin, K., Peischl, J., Thompson,
1124 C. R., Ryerson, T. B., Frost, G. J., McDonald, B. C., and Cooper, O. R.: Tropical tropospheric ozone distribution
1125 and trends from in situ and satellite data, *Atmos. Chem. Phys.*, 24, 9975–10000, [https://doi.org/10.5194/acp-24-](https://doi.org/10.5194/acp-24-9975-2024)
1126 [9975-2024](https://doi.org/10.5194/acp-24-9975-2024), 2024.

1127 Gelaro, R., McCarty, W., Suarez, M. J., Todling, R., Molod, A., Takacs, L., Randles, C. A., Darmenov,
1128 A., Bosilovich, M. G., Reichle, R., Wargan, K., Coy, L., Cullather, R., Draper, C., Akella, S., Buchard,
1129 V., Conaty, A., da Silva, A. M., Gu, W., Kim, G.-K., Koster, R., Lucchesi, R., Merkova, D., Nielsen, J.
1130 E., Partyka, G., Pawson, S., Putman, W., Rienecker, M., Schubert, S. D., Sienkiewicz, M., and Zhao, B.: The
1131 Modern-Era Retrospective Analysis for Research and Applications, Version 2 (MERRA2), *J. Clim.*, 30, 5419–
1132 5454, <https://doi.org/10.1175/JCLI-D-16-0758.1>, 2017.

1133 Gettelman, A., Mills, M. J., Kinnison, D. E., Garcia, R. R., Smith, A. K., Marsh, D. R., Tilmes, S., Vitt, F., Bardeen,
1134 C. G., McInerny, J., Liu, H.-L., Solomon, S. C., Polvani, L. M., Emmons, L. K., Lamarque, J.-F., Richter, J. H.,
1135 Glanville, A. S., Bacmeister, J. T., Phillips, A. S., Neale, R. B., Simpson, I. R., DuVivier, A. K., Hodzic, A., and

1136 Randel, W. J.: The Whole Atmosphere Community Climate Model version 6 (WACCM6), *J. Geophys. Res.-*
1137 *Atmos.*, 124, 12,380–12,403, <https://doi.org/10.1029/2019JD030943>, 2019.

1138 Gratz, L. E., Jaffe, D. A., and Hee, J. R.: Causes of increasing ozone and decreasing carbon monoxide in springtime
1139 at the Mt. Bachelor Observatory from 2004 to 2013, *Atm. Env.*, 109, 323–330,
1140 <http://dx.doi.org/10.1016/j.atmosenv.2014.05.076>, 2015.

1141 He, H., Stehr, J. W., Hains, J. C., Krask, D. J., Doddridge, B. G., Vinnikov, K. Y., Canty, T. P., Hosley, K. M.,
1142 Salawitch, R. J., Worden, H. M., and Dickerson, R. R.: Trends in emissions and concentrations of air pollutants in
1143 the lower troposphere in the Baltimore/Washington airshed from 1997 to 2011, *Atmos. Chem. Phys.*, 13,
1144 <https://doi.org/10.5194/acp-13-7859-2013>, 2013.

1145 Hedelius, J. K., Toon, G. C., Buchholz, R. R., Iraci, L. T., Podolske, J. R., Roehl, C. M., et al.: Regional and urban
1146 column CO trends and anomalies as observed by MOPITT over 16 years, *J. Geophys. Res.-Atmos.*, 126,
1147 e2020JD033967, <https://doi.org/10.1029/2020JD033967>, 2021.

1148 Hegglin, M. I., and Shepherd, T. G.: Large Climate-Induced Changes in Ultraviolet Index and Stratosphere-to
1149 Troposphere Ozone Flux, *Nature Geoscience*, 2, 687–691, <http://dx.doi.org/10.1038/ngeo604>, 2009.

1150 Hegglin, M. I., Tegtmeier, S., Anderson, J., Bourassa, A. E., Brohede, S., Degenstein, D., Froidevaux, L., Funke, B.,
1151 Gille, J., Kasai, Y., Kyrölä, E. T., Lumpe, J., Murtagh, D., Neu, J. L., Pérot, K., Remsberg, E. E., Rozanov, A.,
1152 Toohey, M., Urban, J., von Clarmann, T., Walker, K. A., Wang, H.-J., Arosio, C., Damadeo, R., Fuller, R. A.,
1153 Lingenfelter, G., McLinden, C., Pendlebury, D., Roth, C., Ryan, N. J., Sioris, C., Smith, L., and Weigel, K.:
1154 Overview and update of the SPARC Data Initiative: comparison of stratospheric composition measurements from
1155 satellite limb sounders, *Earth Syst. Sci. Data*, 13, 1855–1903, <https://10.5194/essd-13-1855-2021>, 2021.

1156 Hess, P. G., and Zbinden, R.: Stratospheric impact on tropospheric ozone variability and trends: 1990–2009, *Atmos.*
1157 *Chem. Phys.*, 13, 649–674, <https://doi.org/10.5194/acp-13-649-20132013>, 2013.

1158 Heue, K.-P., Coldewey-Egbers, M., Delcloo, A., Lerot, C., Loyola, D., Valks, P., and van Roozendaal, M.: *Atmos.*
1159 *Meas. Tech.*, 9, 5037–5051, <https://doi.org/10.5194/amt-9-5037-2016>, 2016.

1160 Hoesly, R. M., Smith, S. J., Feng, L., Klimont, Z., Janssens-Maenhout, G., Pitkanen, T., Seibert, J. J., Vu, L., Andres,
1161 R. J., Bolt, R. M., Bond, T. C., Dawidowski, L., Kholod, N., Kurokawa, J.-I., Li, M., Liu, L., Lu, Z., Moura, M.
1162 C. P., O'Rourke, P. R., and Zhang, Q.: Historical (1750–2014) anthropogenic emissions of reactive gases and
1163 aerosols from the Community Emissions Data System (CEDS), *Geosci. Model Dev.*, 11, 369–408. doi:
1164 10.5194/gmd-11-369-2018, 2018.

1165 Horr, P., Borken-Kleefeld, J., Caro, D., Dessens, O., Endresen, O., Gauss, M., Grewe, V., Hauglustaine, D., Isaksen,
1166 I. S. A., Jockel, P., Lelieveld, J., Myhre, G., Meijer, E., Olivie, D., Prather, M., Schnadt Poberaj, C., Shine, K. P.,
1167 Staehelin, J., Tang, Q., van Aardenne, J., van Velthoven, P., and Sausen, R.: The impact of traffic emissions on
1168 atmospheric ozone and OH: results from QUANTIFY, *Atmos. Chem. Phys.*, 9, 3113–3136, [www.atmos-chem-](http://www.atmos-chem-phys.net/9/3113/2009/)
1169 [phys.net/9/3113/2009/](http://www.atmos-chem-phys.net/9/3113/2009/), 2009.

1170 Hsu, J. and Prather, M. J.: Is the residual vertical velocity a good proxy for stratosphere-troposphere exchange of
1171 ozone?, *Geophys. Res. Lett.*, 41, 9024–9032, <https://doi.org/10.1002/2014GL061994>, 2014.

1172 Huang, L., Fu, R., Jiang, J. H., Wright, J. S., and Luo, M.: Geographic and seasonal distributions of CO transport
1173 pathways and their roles in determining CO centers in the upper troposphere, *Atmos. Chem. Phys.*, 12, 4683–4698,
1174 <https://doi.org/10.5194/acp-12-4683-2012>, 2012.

1175 Huang, L., Fu, R., and Jiang, J. H.: Impacts of fire emissions and transport pathways on the interannual variation of
1176 CO in the tropical upper troposphere, *Atmos. Chem. Phys.*, 14, 4087–4099, [https://doi.org/10.5194/acp-14-4087-](https://doi.org/10.5194/acp-14-4087-2014)
1177 [2014](https://doi.org/10.5194/acp-14-4087-2014), 2014.

1178 Huang, L., Jiang, J. H., Murray, L. T., Damon, M. R., Su, H., and Livesey, N. J.: Evaluation of UTLS carbon monoxide
1179 simulations in GMI and GEOS-Chem chemical transport models using Aura MLS observations, *Atmos. Chem.*
1180 *Phys.*, 16, 5641–5663, <https://doi.org/10.5194/acp-16-5641-2016>, 2016.

1181 Hubert, D., Lambert, J.-C., Verhoelst, T., Granville, J., Keppens, A., Baray, J.-L., Bourassa, A. E., Cortesi, U.,
1182 Degenstein, D. A., Froidevaux, L., Godin-Beekmann, S., Hoppel, K. W., Johnson, B. J., Kyrölä, E., Leblanc, T.,
1183 Lichtenberg, G., Marchand, M., McElroy, C. T., Murtagh, D., Nakane, H., Portafaix, T., Querel, R., Russell III, J.
1184 M., Salvador, J., Smit, H. G. J., Stebel, K., Steinbrecht, W., Strawbridge, K. B., Stübi, R., Swart, D. P. J., Taha,
1185 G., Tarasick, D. W., Thompson, A. M., Urban, J., van Gijssel, J. A. E., Van Malderen, R., von der Gathen, P.,
1186 Walker, K. A., Wolfram, E., and Zawodny, J. M.: Ground-based assessment of the bias and long-term stability of
1187 14 limb and occultation ozone profile data records, *Atmos. Meas. Tech.*, 9, 2497–2534,
1188 <https://doi.org/10.5194/amt-9-2497-2016>, 2016.

1189 Jiang, J. H., Livesey, N. J., Su, H., Neary, L., McConnell, J. C., and Richards, N. A. D.: Connecting surface emissions,
1190 convective uplifting, and long-range transport of carbon monoxide in the upper troposphere: New observations
1191 from the Aura Microwave Limb Sounder, *Geophys. Res. Lett.*, 34, L18812, <https://doi.org/10.1029/2007gl030638>,
1192 2007.

1193 Jiang, Z., Worden, J. R., Worden, H., Deeter, M., Jones, D. B. A., Arellano, A. F., and Henze, D. K.: A 15-year record
1194 of CO emissions constrained by MOPITT CO observations, *Atmos. Chem. Phys.*, 17, 4565–4583,
1195 <https://doi.org/10.5194/acp17-4565-2017>, 2017.

1196 Jones, C. D., Collins, M., Cox, P. M., and Spall, S. A.: The Carbon Cycle Response to ENSO: A Coupled Climate–
1197 Carbon Cycle Model Study, *J. Climate*, 14, 4113–4129, [https://doi.org/10.1175/1520-](https://doi.org/10.1175/1520-0442(2001)014<4113:tcrcrte>2.0.CO;2)
1198 [0442\(2001\)014<4113:tcrcrte>2.0.CO;2](https://doi.org/10.1175/1520-0442(2001)014<4113:tcrcrte>2.0.CO;2), 2001.

1199 Kinnison, D. E., Brasseur, G. P., Walters, S., Garcia, R. R., Sassi, F., Boville, B. A., Marsh, D. Harvey, L., Randall,
1200 C., Randel, W., Lamarque, J. F., Emmons, L. K., Hess, Orlando, J., Tyndall, G., and Pan, L.: Sensitivity of
1201 chemical tracers to meteorological parameters in the MOZART-3 chemical transport model, *J. Geophys. Res.*,
1202 112, D20302, <https://doi.org/10.1029/2006JD007879>, 2007.

1203 Khalil, M. A. K., and Rasmussen, R. A.: The global cycle of carbon monoxide: trends and mass balance, *Chemosphere*,
1204 20, Nos. 1–2, pp. 227–242, [https://doi.org/10.1016/0045-6535\(90\)90098-E](https://doi.org/10.1016/0045-6535(90)90098-E), 1990.

1205 Kumar, A., Wu, S., Weise, M. F., Honrath, R., Owen, R. C., Helmig, D., Kramer, L., Val Martin, M., and Li, Q.: Free-
1206 troposphere ozone and carbon monoxide over the North Atlantic for 2001–2011, *Atmos. Chem. Phys.*, 13, 12537–
1207 12547, <https://doi.org/10.5194/acp-13-12537-2013>, 2013.

1208 Laken, B. A., and Shahbaz, T.: Satellite-Detected Carbon Monoxide Pollution during 2000–2012: Examining Global
1209 Trends and also Regional Anthropogenic Periods over China, the EU and the USA, *Climate*, 2014, 2, 1-16,
1210 <https://doi.org/10.3390/cli2010001>, 2014.

1211 Lee, D. S., Fahey, D. W., Skowron, A., Allen, M. R., Burkhardt, U., Chen, Q., Doherty, S. J., Freeman, S., Forster, P.
1212 M., Fuglestedt, J., Gettelman, A., De Leon, R. R., Lim, L. L., Lund, M. T., Millar, R. J., Owen, B., Penner, J. E.,
1213 Pitari, G., Prather, M. J., Sausen, R., and Wilcox, L. J.: The contribution of global aviation to anthropogenic climate
1214 forcing for 2000 to 2018, *Atmos. Env.*, 244, 117834, doi.org/10.1016/j.atmosenv.2020.117834, 2021.

1215 Leventidou, E., Weber, M., Eichmann, K.-U., Burrows, J. P., Heue, K.-P., Thompson, A. M., and Johnson, B. J.:
1216 Harmonisation and trends of 20-year tropical tropospheric ozone data, *Atmos. Chem. Phys.*, 18, 9189–9205,
1217 <https://doi.org/10.5194/acp-18-9189-2018>, 2018.

1218 Li, L., and Liu, Y.: Space-borne and ground observations of the characteristics of CO pollution in Beijing, 2000–2010,
1219 *Atmos. Env.*, 45, 2367–2372. <https://doi.org/10.1016/j.atmosenv.2011.02.026>, 2011.

1220 Liu, J., Logan, J. A., Murray, L. T., Pumphrey, H. C., Schwartz, M. J., and Megretskaja, I. A.: Transport analysis and
1221 source attribution of seasonal and interannual variability of CO in the tropical upper troposphere and lower
1222 stratosphere, *Atmos. Chem. Physics*, 13, 129–146. <https://doi.org/10.5194/acp-13-129-2013>, 2013.

1223 Liu, J., Strode, S. A., Liang, Q., Oman, L. D., Colarco, P. R., Fleming, E. L., Manyin, M. E., Douglass, A. R., Ziemke,
1224 J. R., Lamsal, L. N., and Li, C.: Change in tropospheric ozone in the recent decades and its contribution to global
1225 total ozone, *J. Geophys. Res.-Atmos.*, 127, e2022JD037170. <https://doi.org/10.1029/2022JD037170>, 2022.

1226 Livesey, N. J., and Read, W. G.: Direct retrieval of line-of-sight atmospheric structure from limb sounding
1227 observations, *Geophys. Res. Lett.*, 27, 891-894, <https://doi.org/10.1029/1999GL010964>, 2000.

1228 Livesey, N. J., Van Snyder, W., Read, W. G., and Wagner, P. A.: Retrieval algorithms for the EOS Microwave Limb
1229 Sounder (MLS), *IEEE Trans. Geosci. Remote Sens.*, 44, 1144-1155, <https://doi.org/10.1109/TGRS.2006.872327>,
1230 2006.

1231 Livesey, N. J., Filipiak, M. J., Froidevaux, L., Read, W. G., Lambert, A., Santee, M. L., Jiang, J. H., Waters, J. W.,
1232 Cofield, R. E., Cuddy, D. T., Daffer, W. H., Drouin, B. J., Fuller, R. A., Jarnot, R. F., Jiang, Y. B., Knosp, B. W.,
1233 Li, Q. B., Perun, V. S., Schwartz, M. J., Snyder, W. V., Stek, P. C., Thurstans, R. P., Wagner, P. A., Pumphrey, H.
1234 C., Avery, M., Browell, E. V., Cammas, J.-P., Christensen, L. E., Edwards, D. P., Emmons, L. K., Gao, R.-S., Jost,
1235 H.-J., Loewenstein, M., Lopez, J. D., Nédélec, P., Osterman, G. B., Sachse, G. W., and Webster, C. R.: Validation
1236 of Aura Microwave Limb Sounder O₃ and CO observations in the upper troposphere and lower stratosphere, *J.*
1237 *Geophys. Res.*, 113, D15S02, <https://doi.org/10.1029/2007JD008805>, 2008.

1238 Livesey, N. J., Logan, J. A., Santee, M. L., Waters, J. W., Doherty, R. M., Read, W. G., Froidevaux, L., and Jiang, J.
1239 H.: Interrelated variations of O₃, CO and deep convection in the tropical/subtropical upper troposphere observed
1240 by the Aura Microwave Limb Sounder (MLS) during 2004-2011, *Atmos. Chem. Phys.*, 13, 579–598,
1241 <https://doi.org/10.5194/acp-13-579-2013>, 2013.

1242 Livesey, N. J., Read, W. G., Wagner, P. A., Froidevaux, L., Santee, M. L., Schwartz, M. J., Lambert, A., Millan Valle,
1243 L. F., Pumphrey, H. C., Manney, G. L., Fuller, R. A., Jarnot, R. F., Knosp, B. W., and Lay, R. R.: EOS MLS

1244 Version 5.0x Level 2 and 3 data quality and description document, Tech. rep., Jet Propulsion Laboratory D-105336
1245 Rev. B, Jan. 30, 2022, <https://mls.jpl.nasa.gov/eos-aura-mls/documentation.php>, 2022.

1246 Logan, Jennifer A.: Tropospheric ozone: Seasonal behavior, trends, and anthropogenic influence, *J. Geophys. Res.-*
1247 *Atmos.*, 90, 10463–10482, <https://doi.org/10.1029/JD090iD06p10463>, 1985.

1248 Logan, J. A., Prather, M. J., Wofsy, S. C., and McElroy, M. B.: Tropospheric chemistry: a global perspective, *J.*
1249 *Geophys. Res.*, 86, 7210–7254, <https://doi.org/10.1029/JC086iC08p07210>, 1981.

1250 Logan, J. A., Megretskaya, I., Nassar, R., Murray, L. T., Zhang, L., Bowman, K. W., Worden, H. M., and Luo, M.:
1251 Effects of the 2006 El Niño on tropospheric composition as revealed by data from the Tropospheric Emission
1252 Spectrometer (TES), *Geophys. Res. Lett.*, 35, L03816, <https://doi.org/10.1029/2007GL031698>, 2008.

1253 Ma, X., Huang, J., Hegglin, M. I., Jöckel, P., and Zhao, T.: Causes of growing middle-upper tropospheric ozone over
1254 the Northwest Pacific region, *Atmos. Chem. Phys.*, <https://doi.org/10.5194/egusphere-2023-2411>, in press, 2024.

1255 McDuffie, E. E., Smith, S. J., O'Rourke, P., Tibrewal, K., Venkataraman, C., Marais, E. A., Zheng, B., Crippa, M.,
1256 Brauer, M., and Martin, R. V.: A global anthropogenic emission inventory of atmospheric pollutants from sector-
1257 and fuel-specific sources (1970–2017): an application of the Community Emissions Data System (CEDS), *Earth*
1258 *Syst. Sci. Data*, 12, 3413–3442, <https://doi.org/10.5194/essd-12-3413-2020>, 2020.

1259 Meinshausen, M., Vogel, E., Nauels, A., Lorbacher, K., Meinshausen, N., Etheridge, D. M., Fraser, P. J., Montzka, S.
1260 A., Rayner, P. J., Trudinger, C. M., Krumme, P. B., Beyerle, U., Canadell, J. G., Daniel, J. S., Enting, I. G., Law,
1261 R. M., Lunder, C. R., O'Doherty, S., Prinn, R. G., Reimann, S., Rubino, M., Velders, G. J. M., Vollmer, M. K.,
1262 Wang, R. H.-J., and Weiss, R.: Historical greenhouse gas concentrations for climate modelling (CMIP6),
1263 *Geoscientific Model Development*, 10(5), 2057–2116. <https://doi.org/10.5194/gmd-10-2057-2017>, 2017.

1264 Meinshausen, M., Nicholls, Z. R. J., Lewis, J., Gidden, M. J., Vogel, E., Freund, M., Beyerle, U., Gessner, C., Nauels,
1265 A., Bauer, N., Canadell, J. G., Daniel, J. S., John, A., Krummel, P. B., Luderer, G., Meinshausen, N., Montzka, S.
1266 A., Rayner, P. J., Reimann, S., Smith, S. J., van den Berg, M., Velders, G. J. M., Vollmer, M. K., and Wang, R.
1267 H. J.: The shared socio-economic pathway (SSP) greenhouse gas concentrations and their extensions to 2500,
1268 *Geosci. Model Dev.*, 13, 3571–3605, <https://doi.org/10.5194/gmd-13-3571-2020>, 2020.

1269 Meul, S., Langematz, U., Kröger, P., Oberländer-Hayn, S., and Jöckel, P.: Future changes in the stratosphere-to-
1270 troposphere ozone mass flux and the contribution from climate change and ozone recovery, *Atmos. Chem. Phys.*,
1271 18, 7721–7738, <https://doi.org/10.5194/acp-18-7721-2018>, 2018.

1272 Miyazaki, K., Bowman, K., Sekiya, T., Takigawa, M., Neu, J. L., Sudo, K., Osterman, G., and Eskes, H.: Global
1273 tropospheric ozone responses to reduced NO_x emissions linked to the COVID-19 worldwide lockdowns, *Science*
1274 *Advances*, 7(24), eabf7460, <https://doi.org/10.1126/sciadv.abf7460>, 2021.

1275 Monks, P. S., Archibald, A. T., Colette, A., Cooper, O., Coyle, M., Derwent, R., Fowler, D., Granier, C., Law, K. S.,
1276 Mills, G. E., Stevenson, D. S., Tarasova, O., Thouret, V., von Schneidmesser, E., Sommariva, R., Wild, O., and
1277 Williams, M. L.: Tropospheric ozone and its precursors from the urban to the global scale from air quality to short-
1278 lived climate forcer, *Atmos. Chem. Phys.*, 15, 8889–8973, <https://doi.org/10.5194/acp-15-8889-2015>, 2015.

1279 Montzka, S. A., Krol, M., Dlugokencky, E., Hall, B., Jöckel, P., and Lelieveld, J.: Small Interannual Variability of
1280 Global Atmospheric Hydroxyl, *Science*, 331, 67–69, <https://doi.org/10.1126/science.1197640>, 2011.

1281 Murray, L. T., Mickley, L. J., Kaplan, J. O., Sofen, E. D., Pfeiffer, M., and Alexander, B.: Factors controlling
1282 variability in the oxidative capacity of the troposphere since the Last Glacial Maximum, *Atmos. Chem. Phys.*, 14,
1283 3589–3622, <https://doi.org/10.5194/acp-14-3589-2014>, 2014.

1284 Nassar, R., Logan, J. A., Megretskaia, I. A., Murray, L. T., Zhang, L., & Jones, D. B. A., Analysis of tropical
1285 tropospheric ozone, carbon monoxide, and water vapor during the 2006 El Niño using TES observations and the
1286 GEOS-Chem model, *J. Geophys. Res.-Atmos.*, 114, D17304, <https://doi.org/10.1029/2009jd011760>, 2009.

1287 Neely, R. R., and Schmidt, A.: VolcanEESM: Global volcanic sulphur dioxide (SO₂) emissions database from 1850
1288 to present - Version 1.0., <https://doi.org/10.5285/76ebdc0b-0eed-4f70-b89e-55e606bcd568>, 2016.

1289 Neu, J. L., Flury, T., Manney, G. L., Santee, M. L., Livesey, N. J., and Worden, J.: Tropospheric ozone variations
1290 governed by changes in stratospheric circulation, *Nat. Geosci.*, 7, 340–344, <https://doi.org/10.1038/ngeo2138>,
1291 2014.

1292 O’Neill, B. C., Tebaldi, C., van Vuuren, D. P., Eyring, V., Friedlingstein, P., Hurtt, G., Knutti, R., Kriegler, E.,
1293 Lamarque, J.-F., Lowe, J., Meehl, G. A., Moss, R., Riahi, K., and Sanderson, B. M.: The Scenario Model
1294 Intercomparison Project (Scenario MIP) for CMIP6, *Geosci. Model Dev.*, 9, 3461–3482,
1295 <https://doi.org/10.5194/gmd-9-3461-2016>, 2016.

1296 Oman, L. D., Ziemke, J. R., Douglass, A. R., Waugh, D. W., Lang, C., Rodriguez, J. M., and Nielsen, J. E.: The
1297 response of tropical tropospheric ozone to ENSO, *Geophys. Res. Lett.*, 38, L13706,
1298 <https://doi.org/10.1029/2011gl047865>, 2011.

1299 Oman, L. D., Douglass, A. R., Ziemke, J. R., Rodriguez, J. M., Waugh, D. W., and Nielsen, J. E.: The ozone response
1300 to ENSO in Aura satellite measurements and a chemistry-climate simulation, *J. Geophys. Res.*, 118, 965–976,
1301 <https://doi.org/10.1029/2012jd018546>, 2013.

1302 Park, M., Randel, W. J., Kinnison, D. E., Emmons, L. K., Bernath, P. F., and Walker, K. A., Boone, C. D., and Livesey,
1303 N. J.: Hydrocarbons in the upper troposphere and lower stratosphere observed from ACE-FTS and comparisons
1304 with WACCM, *J. Geophys. Res.-Atmos.*, 118, 1964–1980, <https://doi.org/10.1029/2012JD018327>, 2013.

1305 Park, K., Wang, Z., Emmons, L. K., and Mak, J. E.: Variation of atmospheric CO, $\delta^{13}\text{C}$, and $\delta^{18}\text{O}$ at high northern
1306 latitude during 2004–2009: Observations and model simulations, *J. Geophys. Res.-Atmos.*, 120, 11,024–11,036,
1307 <https://doi.org/10.1002/2015JD023191>, 2015.

1308 Park, M., Worden, H. M., Kinnison, D. E., Gaubert, B., Tilmes, S., Emmons, L. K., Santee, M. L., Froidevaux, L.,
1309 and Boone, C. D.: Fate of pollution emitted during the 2015 Indonesian fire season, *J. Geophys. Res.-Atmos.*, 126,
1310 e2020JD033474, <https://doi.org/10.1029/2020JD033474>, 2021.

1311 Patel, A., Mallika, C., Chandrab, N., Patrab, P. K., Steinbacher, M., Revisiting regional and seasonal variations in
1312 decadal carbon monoxide variability: Global reversal of growth rate, *Science of the Total Environment*, 909,
1313 168476, <https://doi.org/10.1016/j.scitotenv.2023.168476>, 2024.

1314 Petzold, A., Thouret, V., Gerbig, C., Zahn, A., Brenninkmeijer, C. A. M., Gallagher, M., Hermann, M., Pontaud, M.,
1315 Ziereis, H., Boulanger, D., Marshall, J., Nédélec, P., Smit, H. G. J., Friess, U., Flaud, J.-M., Wahner, A., Cammas,
1316 J.-P., and Volz-Thomas, A.: Global-scale atmosphere monitoring by in-service aircraft – current achievements and

1317 future prospects of the European Research Infrastructure IAGOS, *Tellus B*, 67, 28452,
1318 <https://doi.org/10.3402/tellusb.v67.28452>, 2015.

1319 Price, C., and Rind, D.: A simple lightning parameterization for calculating global lightning distributions, *J. Geophys.*
1320 *Res.-Atmos.*, 97, 9919–9933, <https://doi.org/10.1029/92JD00719>, 1992.

1321 Price, C., Penner, J., and Prather, M.: NO_x from lightning: 1. Global distribution based on lightning physics, *J.*
1322 *Geophys. Res.-Atmos.*, 102(D5), 5929–5941. <https://doi.org/10.1029/96JD03504>, 1997.

1323 Randel, W. J., Park, M., Wu, F., and Livesey, N. J.: A large annual cycle in ozone above the tropical tropopause linked
1324 to the Brewer-Dobson circulation, *J. Atmos. Sci.*, 64, 4479–4488, <https://doi.org/10.1175/2007JAS2409.1>, 2007.

1325 Read, W. G., Shippony, Z., and Snyder, W. V.: The clear-sky unpolarized forward model for the EOS Aura microwave
1326 limb sounder (MLS), *IEEE Trans. Geosci. Remote Sens.*, 44, 1367-1379,
1327 <https://doi.org/10.1109/TGRS.2006.862267>, 2006.

1328 Riahi, K., van Vuuren, D. P., Kriegler, E., Edmonds, J., O'Neill, B. C., Fujimori, S., Bauer, N., Calvin, K., Dellink,
1329 R., Fricko, O., Lutz, W., Popp, A., Crespo Cuaresma, J., Samir, K. C., Leimbach, M., Jiang, L., Kram, T., Rao, S.,
1330 Emmerling, J., Ebi, K., Hasegawa, T., Havlik, P., Humpenöder, F., Da Silva, A., Smith, S., Stehfest, E., Bosetti,
1331 V., Eom, J., Gernaat, D., Masui, T., Rogelj, J., Strefler, J., Drouet, L., Krey, V., Luderer, G., Harmsen, M.,
1332 Takahashi, K., Baumstark, L., Doelman, J. C., Kainuma, M., Klimont, Z., Marangoni, G., Lotze-Campen, H.,
1333 Obersteiner, M., Tabeau, A., Tavoni, M.: The Shared Socioeconomic Pathways and their energy, land use, and
1334 greenhouse gas emissions implications: An overview, *Global Environ. Chang.*, 42, 1045 153–168,
1335 <https://doi.org/10.1016/j.gloenvcha.2016.05.009>, 2017.

1336 Rodgers, C.: *Inverse Methods for Atmospheric Sounding: Theory and Practice*, Vol. 2 of Series on Atmospheric,
1337 Oceanic and Planetary Physics, World Scientific, Singapore, 2000.

1338 Rowlinson, M. J., Rap, A., Arnold, S. R., Pope, R. J., Chipperfield, M. P., McNorton, J., Forster, P., Gordon, H.,
1339 Pringle, K. J., Feng, W., Kerridge, B. J., Latter, B. L., and Siddans, R.: Impact of El Niño–Southern Oscillation on
1340 the interannual variability of methane and tropospheric ozone, *Atmos. Chem. Phys.*, 19, 8669–8686,
1341 <https://doi.org/10.5194/acp-19-8669-2019>, 2019.

1342 Schoeberl, M. R., Duncan, B. N., Douglass, A. R., Waters, J., Livesey, N., Read, W., and Filipiak, M.: The carbon
1343 monoxide tape recorder, *Geophys. Res. Lett.*, 33, L12811, <https://doi.org/10.1029/2006gl026178>, 2006.

1344 Schumann, U., and Huntrieser, H.: The global lightning-induced nitrogen oxides source, *Atmos. Chem. Phys.*, 7,
1345 3823–3907, <https://doi.org/10.5194/acp-7-3823-2007>, 2007.

1346 Soulié, A., Granier, C., Darras, S., Zilbermann, N., Doumbia, T., Guevara, M., Jalkanen, J.-P., Keita, S., Lioussé, C.,
1347 Crippa, M., Guizzardi, D., Hoesly, R., and Smith, S. J.: Global anthropogenic emissions (CAM5-GLOB-ANT) for
1348 the Copernicus Atmosphere Monitoring Service simulations of air quality forecasts and reanalyses, *Earth Syst.*
1349 *Sci. Data*, 16, 2261–2279, <https://doi.org/10.5194/essd-16-2261-2024>, 2024.

1350 Souri, A. H., Choi, Y., Jeon, W., Woo, J.-H., Zhang, Q., and Kurokawa, J.: Remote sensing evidence of decadal
1351 changes in major tropospheric ozone precursors over East Asia, *J. Geophys. Res.-Atmos.*, 122, 2474–2492,
1352 <https://doi.org/10.1002/2016JD025663>, 2017.

1353 SPARC: The SPARC Data Initiative: Assessment of stratospheric trace gas and aerosol climatologies from satellite
1354 limb sounders, M. I. Hegglin and S. Tegtmeier (eds.), SPARC Report No. 8, WCRP-5/2017, available at
1355 www.sparc-climate.org/publications/sparc-reports/, 2017.

1356 Stein, O., M. G. Schultz, M. G., Bouarar, I., Clark, H., Huijnen, V., A. Gaudel, A., George, M., and Clerbaux, C.: On
1357 the wintertime low bias of Northern Hemisphere carbon monoxide found in global model simulations, *Atmos.*
1358 *Chem. Phys.*, 14, 9295–9316, <https://doi.org/10.5194/acp-14-9295-2014>, 2014.

1359 Steinbrecht, W., Kubistin, D., Plass-Dülmer, C., Davies, J., Tarasick, D. W., Gathen, P. v. d., Deckelmann, H., Jepsen,
1360 N., Kivi, R., Lyall, N., Palm, M., Notholt, J., Kois, B., Oelsner, P., Allaart, M., Píters, A., Gill, M., Van Malderen,
1361 R., Delcloo, A. W., Sussmann, R., Mahieu, E., Servais, C., Romanens, G., Stübi, R., Ancellet, G., Godin-
1362 Beekmann, S., Yamanouchi, S., Strong, K., Johnson, B., Cullis, P., Petropavlovskikh, I., Hannigan, J. W.,
1363 Hernandez, J.-L., Diaz Rodriguez, A., Nakano, T., Chouza, F., Leblanc, T., Torres, C., Garcia, O., Röhling, A. N.,
1364 Schneider, M., Blumenstock, T., Tully, M., Paton-Walsh, C., Jones, N., Querel, R., Strahan, S., Stauffer, R. M.,
1365 Thompson, A. M., Inness, A., Engelen, R., Chang, K.-L., and Cooper, O. R.: COVID-19 Crisis Reduces Free
1366 Tropospheric Ozone Across the Northern Hemisphere, *Geophys. Res. Lett.*, 48, e2020GL091987,
1367 <https://doi.org/10.1029/2020GL091987>, 2021.

1368 Stevenson, D. S., Young, P. J., Naik, V., Lamarque, J.-F., Shindell, D. T., Voulgarakis, A., Skeie, R. B., Dalsoren, S.
1369 B., Myhre, G., Berntsen, T. K., Folberth, G. A., Rumbold, S. T., Collins, W. J., MacKenzie, I. A., Doherty, R. M.,
1370 Zeng, G., van Noije, T. P. C., Strunk, A., Bergmann, D., Cameron-Smith, P., Plummer, D. A., Strode, S. A.,
1371 Horowitz, L., Lee, Y. H., Szopa, S., Sudo, K., Nagashima, T., Josse, B., Cionni, I., Righi, M., Eyring, V., Conley,
1372 A., Bowman, K. W., Wild, O., and Archibald, A.: Tropospheric ozone changes, radiative forcing and attribution
1373 to emissions in the Atmospheric Chemistry and Climate Model Intercomparison Project (ACCMIP), *Atmos.*
1374 *Chem. Phys.*, 13, 3063–3085, <https://doi.org/10.5194/acp-13-3063-2013>, 2013.

1375 Strode, S. A., Worden, H. M., Damon, M., Douglass, A. R., Duncan, B. N., Emmons, L. K., Lamarque, J.-F., Manyin,
1376 M., Oman, L. D., Rodriguez, J. M., Strahan, S. E., and Tilmes, S.: Interpreting space-based trends in carbon
1377 monoxide with multiple models, *Atmos. Chem. Phys.*, 16, 7285–7294, <https://doi.org/10.5194/acp-16-7285-2016>,
1378 2016.

1379 Sudo, K. and Takahashi, M.: Simulation of tropospheric ozone changes during 1997–1998 El Niño: Meteorological
1380 impact on tropospheric photochemistry, *Geophys. Res. Lett.*, 28, 4091–4094,
1381 <https://doi.org/10.1029/2001GL013335>, 2001.

1382 Sudo, K., Takahashi, M., and Akimoto, H.: Future changes in stratosphere-troposphere exchange and their impacts on
1383 future tropospheric ozone simulations, *Geophys. Res. Lett.*, 30, 24, 2256, <https://doi.org/10.1029/2003GL018526>
1384 , 2003.

1385 Tapping, K.F.: The 10.7 cm solar radio flux (F10.7), *Space Weather*, 11, 394–406, <https://doi.org/10.1002/swe.20064>,
1386 2013.

1387 Thompson, A. M., Doddridge, B. G., Witte, J. C., Hudson, R. D., Luke, W. T., Johnson, J. E., Johnson, B. J., Oltmans,
1388 S. J., and Weller, R.: A tropical Atlantic ozone paradox: Shipboard and satellite views of a tropospheric ozone

1389 maximum and wave-one in January–February 1999, *Geophys. Res. Lett.*, 27, 3317–3320,
1390 <https://doi.org/10.1029/1999GL011273>, 2000.

1391 Thompson, A. M., Witte, J. C., Oltmans, S. J., Schmidlin, F. J., Logan, J. A., Fujiwara, M., Kirchhoff, V. W. J., Posny,
1392 F., Coetzee, G. J. R., Hoegger, B., Kawakami, S., Ogawa, T., Fortuin, J. P. F., and Kelder, H. M.: Southern
1393 Hemisphere Additional Ozonesondes (SHADOZ) 1998–2000 tropical ozone climatology. 2. Tropospheric
1394 variability and the zonal wave-one, *J. Geophys. Res.-Atmos.*, 108(D2), 8241,
1395 <https://doi.org/10.1029/2002JD002241>, 2003.

1396 Thompson, A. M., Stauffer, R. M., Wargan, K., Witte, J. C., Kollonige, D. E., and Ziemke, J. R.: Regional and
1397 seasonal trends in tropical ozone from SHADOZ profiles: Reference for models and satellite products, *J. Geophys.*
1398 *Res.-Atmos.*, 126, e2021JD034691, <https://doi.org/10.1029/2021JD034691>, 2021.

1399 Tilmes, S., Hodzic, A., Emmons, L. K., Mills, M. J., Gettelman, A., Kinnison, D. E., Park, M., Lamarque, J.-F., Vitt,
1400 F., Shrivastava, M., Campuzano-Jost, P., Jimenez, J. L., and Liu, X.: Climate forcing and trends of organic
1401 aerosols in the Community Earth System Model (CESM2), *J. of Adv. in Modeling Earth Systems*, 11, 4323–4351,
1402 <https://doi.org/10.1029/2019MS001827>, 2019.

1403 Tsvilidou, M., Sauvage, B., Bennouna, Y., Blot, R., Boulanger, D., Clark, H., Le Flochmoën, E., Nédélec, P., Valérie
1404 Thouret, V., Wolff, P., and Barret, B.: Tropical tropospheric ozone and carbon monoxide distributions:
1405 characteristics, origins, and control factors, as seen by IAGOS and IASI, *Atmos. Chem. Phys.*, 23, 14039–14063,
1406 <https://doi.org/10.5194/acp-23-14039-2023>, 2023.

1407 Verma, S., Yadava, P. K., Lal, D. M., Mall, R. K., Kumar, H., and Payra, S.: Role of Lightning NO_x in Ozone
1408 Formation: A Review, *Pure Appl. Geophys.*, <https://doi.org/10.1007/s00024-021-02710-5>, 2021.

1409 Voulgarakis, A., Marlier, M. E., Faluvegi, G., Shindell, D. T., Tsigaridis, K., and Mangeon, S.: Interannual variability
1410 of tropospheric trace gases and aerosols: The role of biomass burning emissions, *J. Geophys. Res.-Atmos.*, 120,
1411 7157–7173, <https://doi.org/10.1002/2014JD022926>, 2015.

1412 Wang, P.-H., Fishman, J., Harvey, V. L., and Hitchman, M. H.: Southern tropical upper tropospheric zonal ozone
1413 wave-1 from SAGE II observations (1985–2002), *J. Geophys. Res.-Atmos.*, 111, D08305,
1414 <https://doi.org/10.1029/2005JD006221>, 2006.

1415 Wang, H., Lu, X., Jacob, D. J., Cooper, O. R., Chang, K.-L., Li, K., Gao, M., Liu, Y., Sheng, B., Wu, K., Wu, T.,
1416 Zhang, J., Sauvage, B., Nédélec, P., Blot, R., and Fan, S.: Global tropospheric ozone trends, attributions, and
1417 radiative impacts in 1995–2017: an integrated analysis using aircraft (IAGOS) observations, ozonesonde, and
1418 multi-decadal chemical model simulations, *Atmos. Chem. Phys.*, 22, 13753–13782, <https://doi.org/10.5194/acp-22-13753-2022>, 2022.

1420 Warner, J., Carminati, F., Wei, Z., Lahoz, W., and Attié, J.-L.: Tropospheric carbon monoxide variability from AIRS
1421 under clear and cloudy conditions, *Atmos. Chem. Phys.*, 13, 12469–12479, [https://doi.org/10.5194/acp-13-12469-](https://doi.org/10.5194/acp-13-12469-2013)
1422 [2013](https://doi.org/10.5194/acp-13-12469-2013), 2013.

1423 Waters, J., Froidevaux, L., Harwood, R., Jarnot, R., Pickett, H., Read, W., Siegel, P., Cofield, R., Filipiak, M., Flower,
1424 D., Holden, J., Lau, G., Livesey, N., Manney, G., Pumphrey, H., Santee, M., Wu, D., Cuddy, D., Lay, R., Loo, M.,
1425 Perun, V., Schwartz, M., Stek, P., Thurstans, R., Boyles, M., Chandra, S., Chavez, M., Chen, G.-S., Chudasama,

1426 B., Dodge, R., Fuller, R., Girard, M., Jiang, J., Jiang, Y., Knosp, B., LaBelle, R., Lam, J., Lee, K., Miller, D.,
1427 Oswald, J., Patel, N., Pukala, D., Quintero, O., Scaff, D., Snyder, V., Tope, M., Wagner, P., and Walch, M.: The
1428 Earth Observing System Microwave Limb Sounder (EOS MLS) on the Aura satellite, *IEEE Transac. Geosci.*
1429 *Remote Sens.*, 44, 5, <https://doi.org/10.1109/TGRS.2006.873771>, 2006.

1430 Witte, J. C., Schoeberl, M. R., Douglass, A. R., and Thompson, A. M.: The quasi-biennial oscillation in tropical ozone
1431 from SHADOZ and HALOE, *Atmos. Chem. Phys.*, 8, 3929–3936, <https://doi.org/10.5194/acp-8-3929-2008>, 2008.

1432 Wolter, K., and Timlin, M. S.: El Niño/Southern Oscillation behaviour since 1871 as diagnosed in an extended
1433 multivariate ENSO index (MEI.ext), *Intl. J. Climatology*, 31, 1074–1087, <https://doi.org/10.1002/joc.2336>, 2011.

1434 Worden, H. M., Deeter, M. N., Frankenberg, C., George, M., Nichitiu, F., Worden, J., Aben, I., Bowman, K. W.,
1435 Clerbaux, C., Coheur, P. F., de Laat, A. T. J., Detweiler, R., Drummond, J. R., Edwards, D. P., Gille, J. C.,
1436 Hurtmans, D., Luo, M., Martinez- Alonso, S., Massie, S., Pfister, G., and Warner, J. X.: Decadal record of satellite
1437 carbon monoxide observations, *Atmos. Chem. Phys.*, 13, 837–850, <https://doi.org/10.5194/acp-13-837-2013>,
1438 2013a.

1439 Worden, J., Wecht, K., Frankenberg, C., Alvarado, M., Bowman, K., Kort, E., Kulawik, S., Lee, M., Payne, V., and
1440 Worden, H.: CH₄ and CO distributions over tropical fires during October 2006 as observed by the Aura TES
1441 satellite instrument and modeled by GEOS-Chem, *Atmos. Chem. Phys.*, 13, 3679–3692,
1442 <https://doi.org/10.5194/acp-13-3679-2013>, 2013b.

1443 Yoon, J., and Pozzer, A.: Model-simulated trend of surface carbon monoxide for the 2001–2010 decade, *Atmos.*
1444 *Chem. Phys.*, 14, 10465–10482, <https://doi.org/10.5194/acp-14-10465-2014>, 2014.

1445 Zhang, L., Li, Q. B., Jin, J., Liu, H., Livesey, N., Jiang, J. H., Mao, Y., Chen, D., Luo, M., and Chen, Y.: Impacts of
1446 2006 Indonesian fires and dynamics on tropical upper tropospheric carbon monoxide and ozone, *Atmos. Chem.*
1447 *Phys.*, 11, 10929–10946, <https://doi.org/10.5194/acp-11-10929-2011>, 2011.

1448 Zhang, S., Zhao, P., He, L., Yang, Y., Liu, B., He, W., Cheng, Y., Liu, Y., Liu, S., Hu, Q., Huang, C., Wu, Y., On-
1449 board monitoring (OBM) for heavy-duty vehicle emissions in China: Regulations, early-stage evaluation and
1450 policy recommendations, *Science of the Total Environment*, Vol. 731, 139045, ISSN 0048-9697,
1451 <https://doi.org/10.1016/j.scitotenv.2020.139045>, 2020.

1452 Zhang, T., Hoell, A., Perlwitz, J., Eischeid, J., Murray, D., Hoerling, M., and Hamill, T.: Towards Probabilistic
1453 Multivariate ENSO Monitoring, *Geophys. Res. Lett.*, 46, <https://doi.org/10.1029/2019GL083946>, 2019.

1454 Zhang, Y., Cooper, O. R., Gaudel, A., Thompson, A. M., Nédélec, P., Ogino, S.-Y., and West, J. J.: Tropospheric
1455 ozone change from 1980 to 2010 dominated by equatorward redistribution of emissions, *Nat. Geosci.*, 9, 875–879,
1456 <https://doi.org/10.1038/ngeo2827>, 2016.

1457 Zheng, B., Chevallier, F., Ciais, P., Yin, Y., Deeter, M. N., Worden, H. M., Wang, Y., Zhang, Q., and He, K.: Rapid
1458 decline in carbon monoxide emissions and export from East Asia between years 2005 and 2016, *Environ. Res.*
1459 *Lett.*, 13, 044007, <https://doi.org/10.1088/1748-9326/aab2b3>, 2018.

1460 Ziemke, J. R., and Chandra, S.: La Niña and El Niño–induced variabilities of ozone in the tropical lower atmosphere
1461 during 1970–2001, *Geophys. Res. Lett.*, 30, 3, 1142, <https://doi.org/10.1029/2002GL016387>, 2003.

1462 Ziemke, J. R., Chandra, S., Oman, L. D., and Bhartia, P. K.: A new ENSO index derived from satellite measurements
1463 of column ozone, *Atmos. Chem. Phys.*, 10, 3711–3721, <https://doi.org/10.5194/acp-10-3711-2010>, 2010.

1464 Ziemke, J. R., A. R. Douglass, A. R., L. D. Oman, L. D., S. E. Strahan, S. E., and B. N. Duncan, B. N.: Tropospheric
1465 ozone variability in the tropics from ENSO to MJO and shorter timescales, *Atmos. Chem. Phys.*, 15, 8037–8049,
1466 <https://doi.org/10.5194/acp-15-8037-2015>, 2015.

1467 Ziemke, J. R., Oman, L. D., Strode, S. A., Douglass, A. R., Olsen, M. A., McPeters, R. D., Bhartia, P. K., Froidevaux,
1468 L., Labow, G. J., Witte, J. C., Thompson, A. M., Haffner, D. P., Kramarova, N. A., Frith, S. M., Huang, L.-K.,
1469 Jaross, G. R., Sefstor, C. J., Deland, M. T., and Taylor, S. L.: Trends in global tropospheric ozone inferred from a
1470 composite record of TOMS/OMI/MLS/OMPS satellite measurements and the MERRA-2 GMI simulation, *Atmos.*
1471 *Chem. Phys.*, 19, 3257–3269, <https://doi.org/10.5194/acp-19-3257-2019>, 2019.

1472 Ziemke, J. R., Kramarova, N. A., Frith, S. M., Huang, L.-K., Haffner, D. P., and Wargan, K.: NASA satellite
1473 measurements show global-scale reductions in free tropospheric ozone in 2020 and again in 2021 during COVID-
1474 19, *Geophys. Res. Lett.*, 49, e2022GL098712, <https://doi.org/10.1029/2022GL098712>, 2022.

1475

1476 **Table 1.** Some characteristics of the three chemistry climate model simulations used in this work.
 1477

Model Designation	Simulation Name	CO Anthropogenic Emissions Dataset	CO Biomass Burning dataset	Nudging timescale (hours)	Tropical Lightning NO_x (Tg N yr⁻¹)	Aircraft NO_x Dataset¹
CAM-chem	CAM-chem-CAMS	CAMS-GLOB-ANT_v5.1	QFED	6	2.34	Soulié et al. (2024)
CAM-chem	CAM-chem-CEDS	CEDSv2	QFED	6	2.34	Soulié et al. (2024)
WACCM	WACCM-CEDS	CEDSv2	QFED	12	2.78	CMIP6

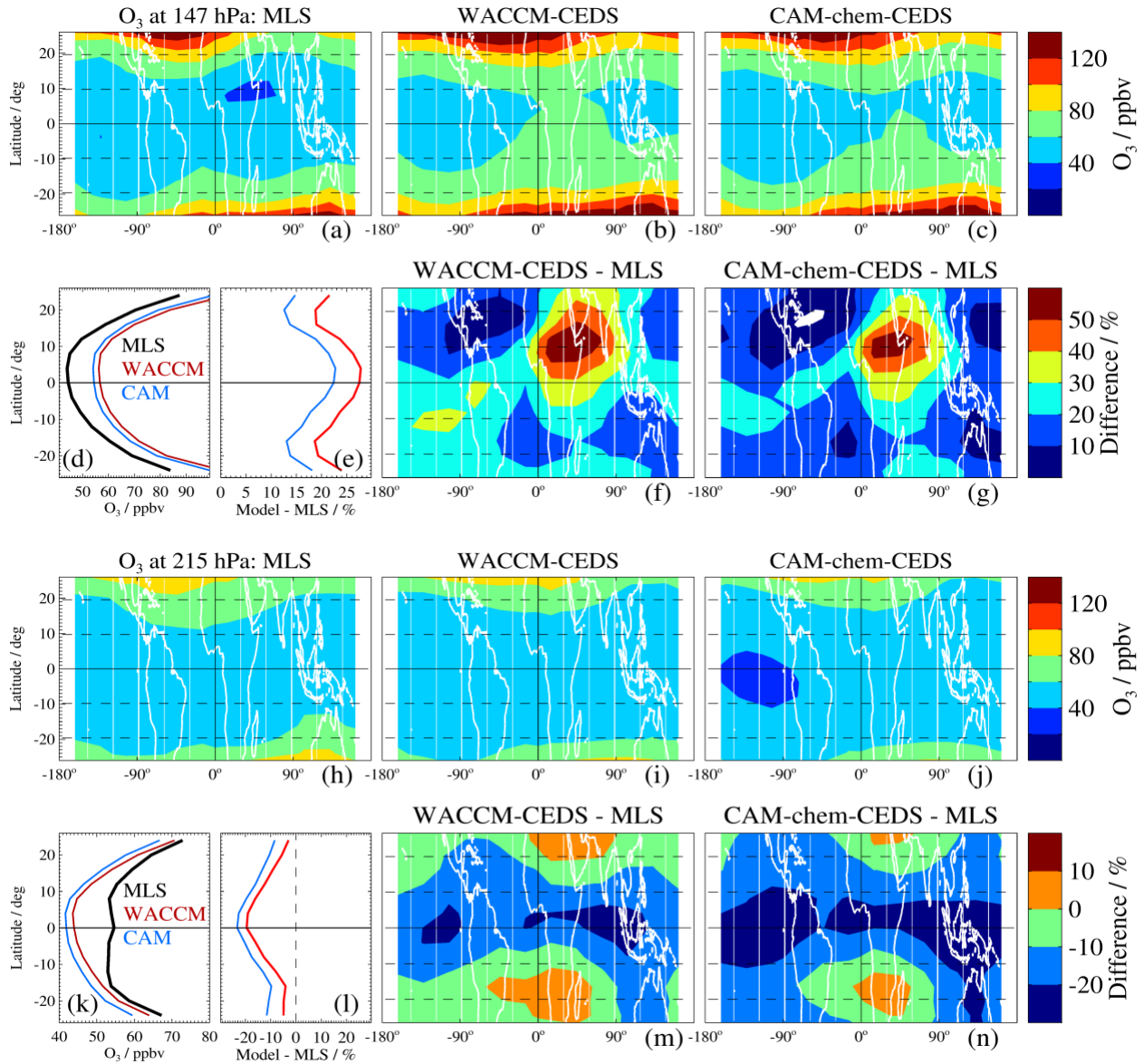
1478
 1479 ¹For 2005–2014, the aircraft NO_x emissions for WACCM-CEDS and both CAM-chem model simulations
 1480 are identical. From 2015 onward, the WACCM-CEDS emissions are kept constant.
 1481

1482 **Table 2.** Trend results from recent tropical upper tropospheric O₃ data analyses. See Sec. 3.1.4
 1483 for other references and comments.
 1484

Reference	Data	Time Period	Trends		Comments
			ppbv decade ⁻¹	% decade ⁻¹	
This work	Aura MLS UT data at 147, 178, and 215 hPa for 20°S–20°N ~8–14 km range	2005–2020	2.0 (1.4) -2 to 7	3.9 (2.8) -4 to 14	trend average (2σ error) trend range* (the negative values are not significantly different from 0)
Based on Thompson et al. (2021)	ozonesonde data from the free troposphere at 5 SHADOZ stations ~5–15 km range	1998–2019	~1 (~2) 0.5 to 2	~2 (~4) 1 to 4	(annual) trend average (annual) trend range
Based on (Fig. S24 of) Gaudel et al. (2024)	IAGOS and sonde UT data from 5 tropical regions ~200–300 hPa range	2004–2019	~3 (~3) -1 to 7	~6 (~6) -2 to 14	trend average trend range

1485 * Trend range for MLS is taken from the minimum and maximum values in mapped tropical UT trends.

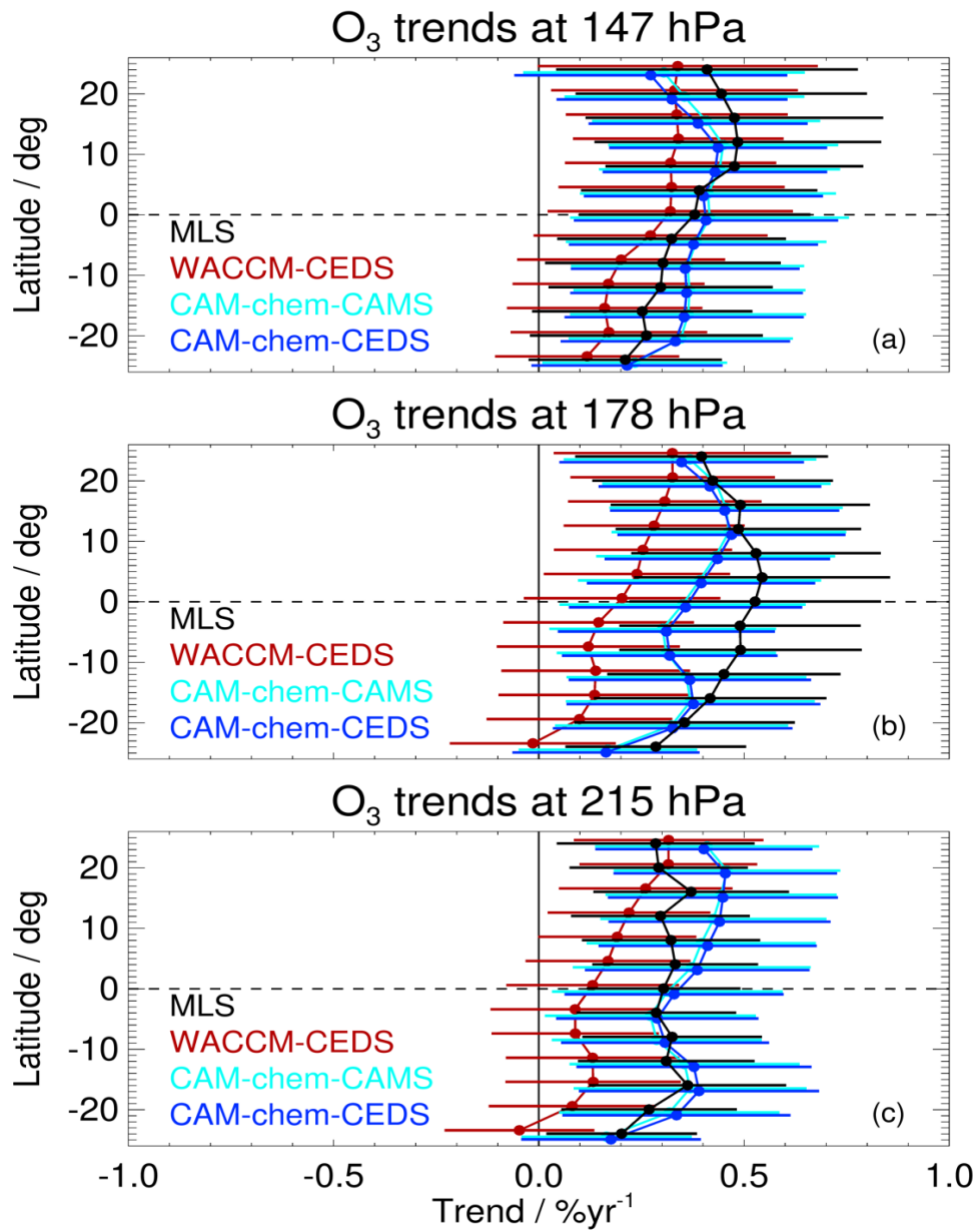
1486 **Figures**
 1487



1488
 1489

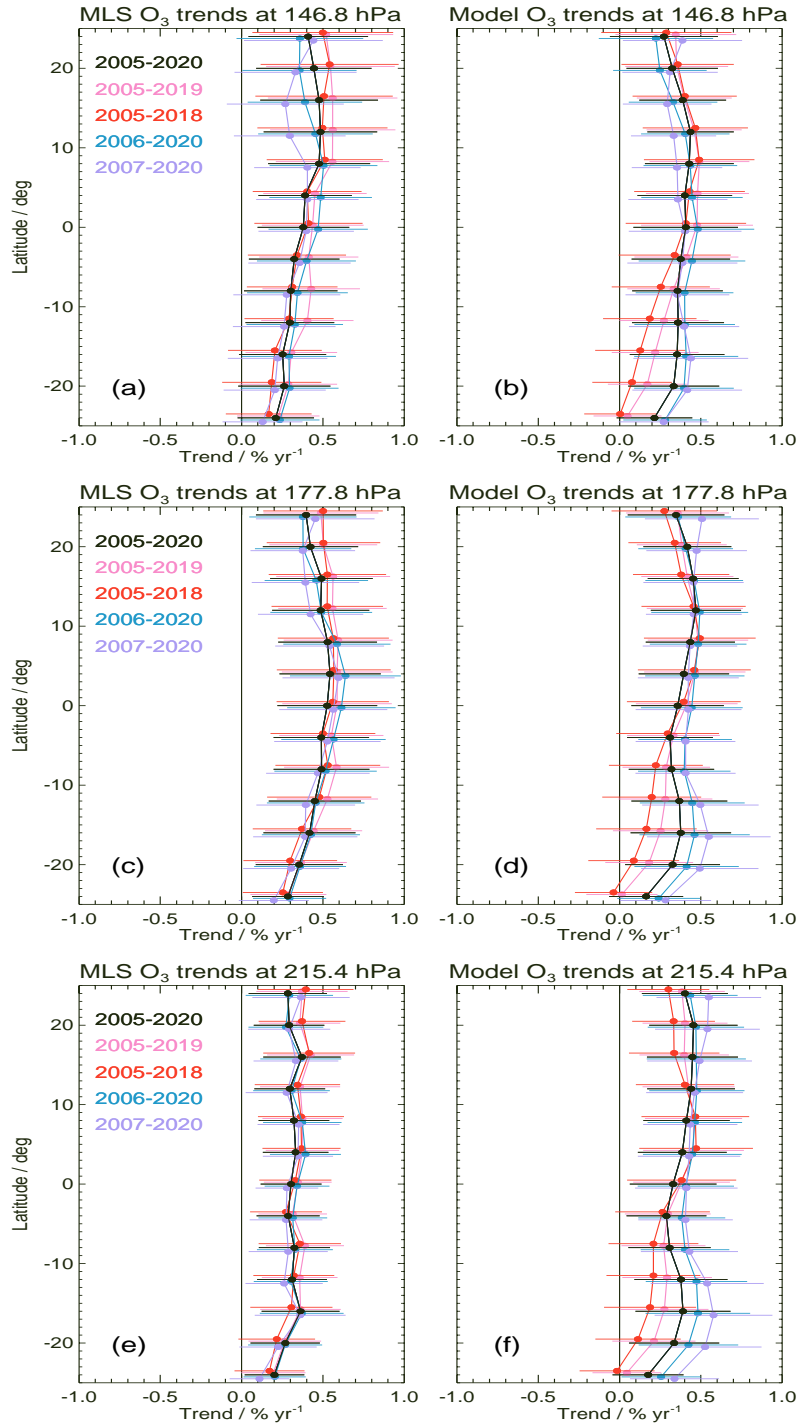
1490 **Figure 1.** Annually-averaged climatological comparisons between MLS and model ozone fields for 2005-
 1491 2020 at low latitudes (full range shown from 26°S to 26°N) at 147 hPa ((a) through (g)) and at 215 hPa ((h)
 1492 through (n)). For 147 hPa: (a) climatological O₃ maps from MLS, (b) from WACCM-CEDS, (c) from
 1493 CAM-chem-CEDS; (d) shows the zonal mean climatology from the MLS data and both model simulations,
 1494 with (e) giving the differences in zonal means for both model simulations minus MLS (color-coded as
 1495 shown in the (d) legend), while (f) provides a difference map of the climatologies from WACCM-CEDS
 1496 minus MLS, and (g) gives the difference map for CAM-chem-CEDS minus MLS. Panels (h) through (n)
 1497 provide the same information as (a) through (g), but for 215 hPa. We note that in panels (d) and (k), CAM
 1498 is an abbreviation for the CAM-chem-CEDS simulation, and WACCM is an abbreviation for the WACCM-
 1499 CEDS simulation.

1500
1501
1502



1503
1504
1505
1506
1507
1508
1509

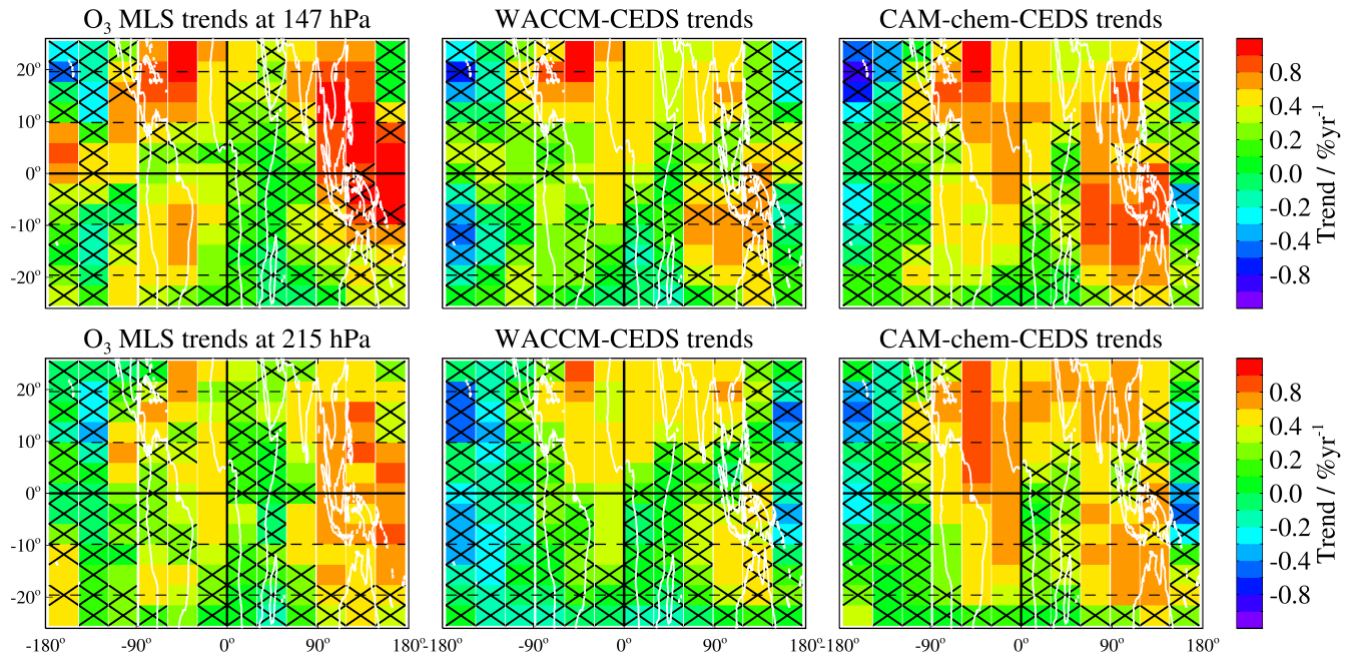
Figure 2. Ozone zonal mean trends versus latitude in the tropical upper troposphere, for 2005–2020, based on MLR analyses of time series from MLS (black), WACCM-CEDS (red), CAM-chem-CAMS (cyan) and CAM-chem-CEDS (blue). Each row corresponds to a different pressure level: (a) for 147 hPa, (b) for 178 hPa, and (c) for 215 hPa, as labeled above each panel. Error bars give the uncertainties (2σ) in the estimated linear trends (see text for more details).



1510
 1511
 1512
 1513
 1514
 1515
 1516
 1517
 1518
 1519

Figure 3. Ozone zonal mean trends versus latitude in the tropical upper troposphere, with results from MLS data analyses shown in the left panels, and model results from CAM-chem-CEDS in the right panels. Each row corresponds to a different pressure level, as labeled. All panels show the trend sensitivity to the time period used in the regression fits. For example, black is used to show the period from 2005 through 2020; results from four other time periods are also shown, with the start or end year shifted by one or two years (see legend for the meaning of the various colors). The error bars given here represent the (2σ) uncertainties in the estimated linear trends.

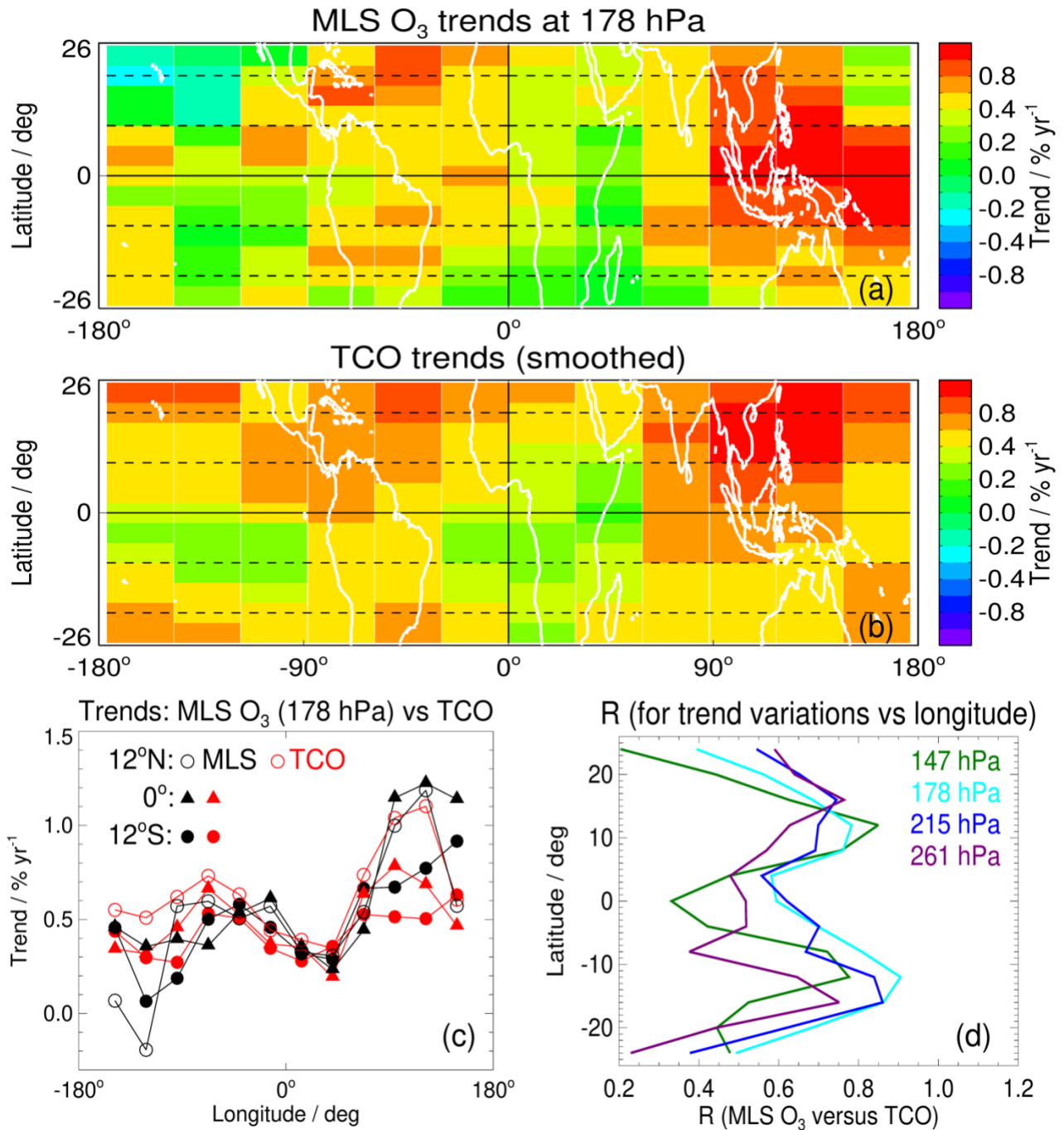
1520
1521



1522
1523
1524
1525
1526
1527
1528
1529

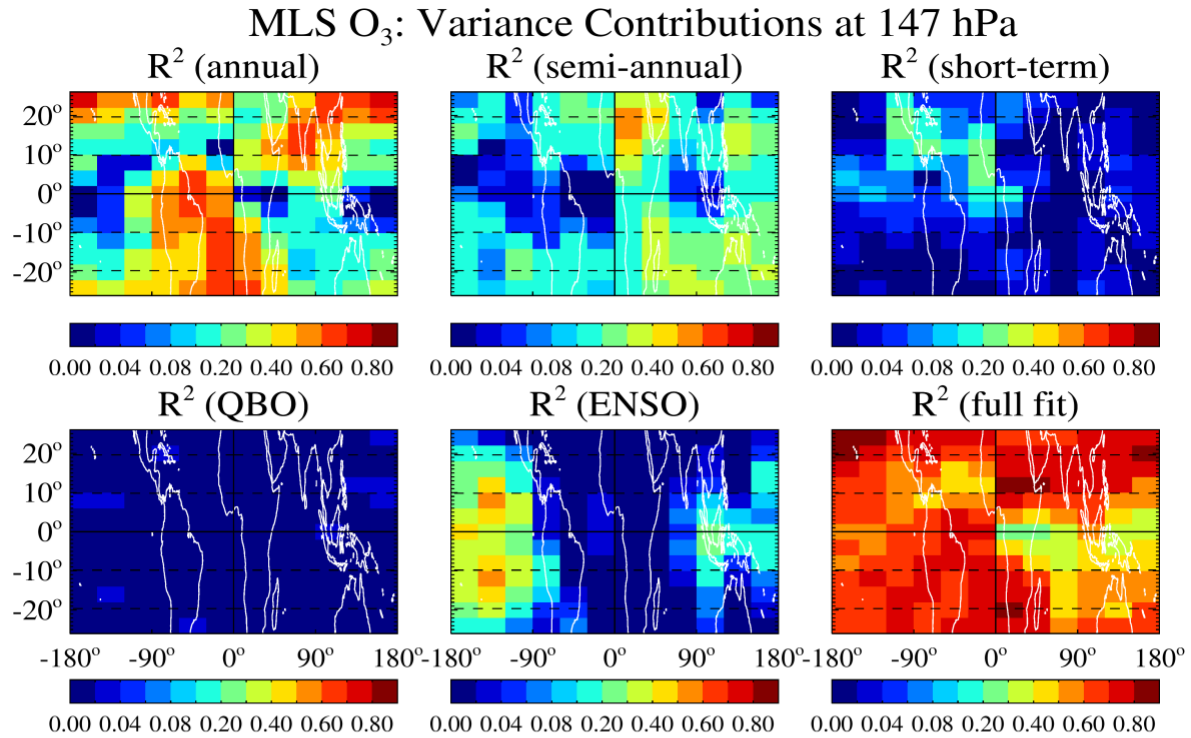
Figure 4. Maps of upper tropospheric O₃ trends (% yr⁻¹) in the tropics for 147 hPa (top row) and 215 hPa (bottom row); the latitude range is from 26°S to 26°N, with maps all centered on the Greenwich meridian. MLS trends (left column) are compared to trends from WACCM-CEDS (middle column) and CAM-chem-CEDS (right column). Black crosses show grid boxes for which the trend estimate is not significantly different from zero (based on our 2 σ error estimates).

1530
1531



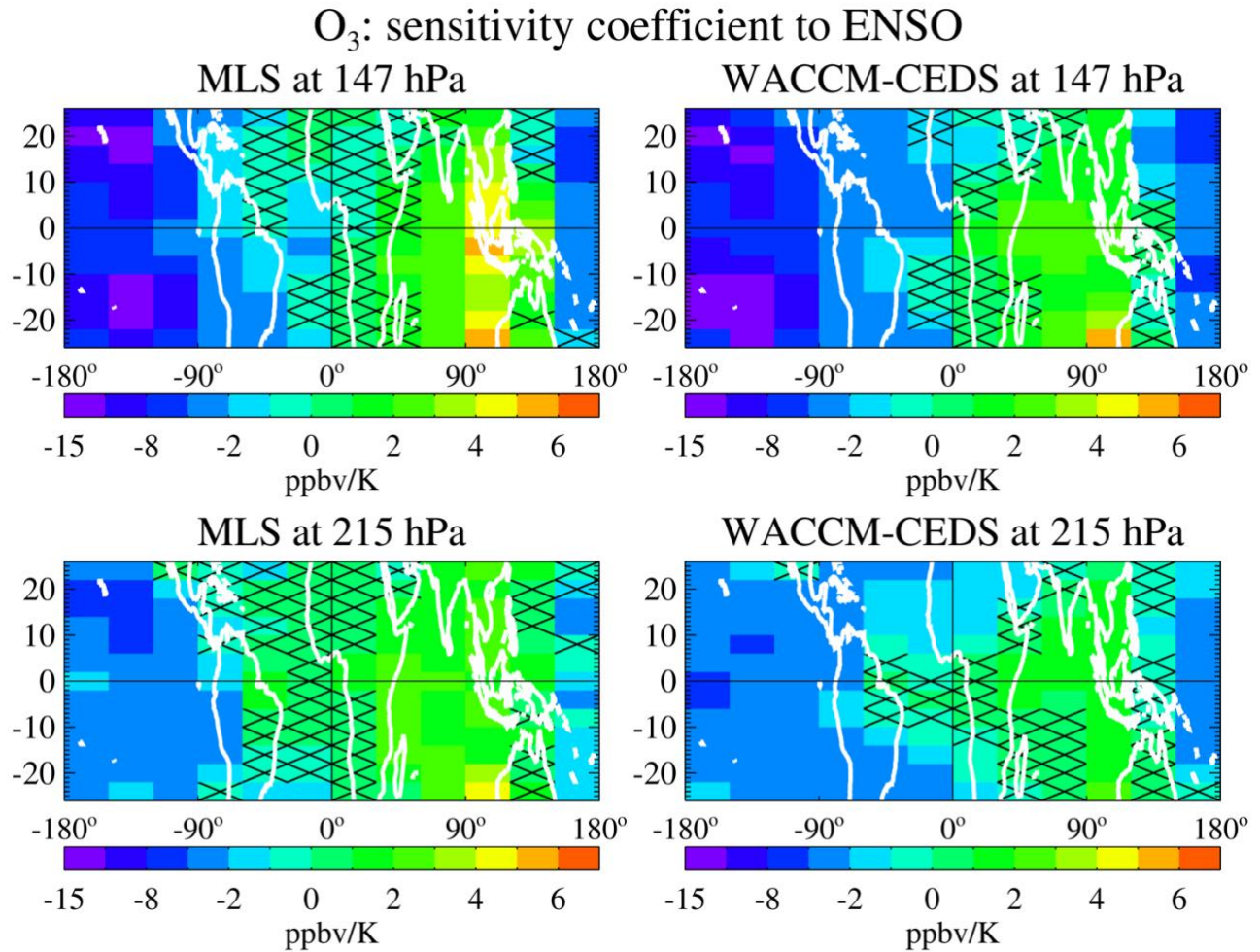
1532
1533
1534
1535
1536
1537
1538
1539

Figure 5. (a) The top map shows MLS ozone trends (2005–2020) at 178 hPa, (b) the bottom map displays horizontally-smoothed tropospheric column ozone trends for the same time period, following the analyses of Ziemke et al. (2019), (c) cross sections of the above mapped trends in 4°-wide latitude bins centered at 12°N, 0°, and 12°S (see legend) for MLS (black) and TCO (red), and (d) correlation coefficient values R (on the x axis) between the MLS ozone trends at different pressures (see legend) and the TCO trends as a function of longitude, at different tropical latitudes (y axis). This panel provides a broader picture of the trend correlations, which exhibit a minimum near the Equator and maxima near 12°S and 12°N.



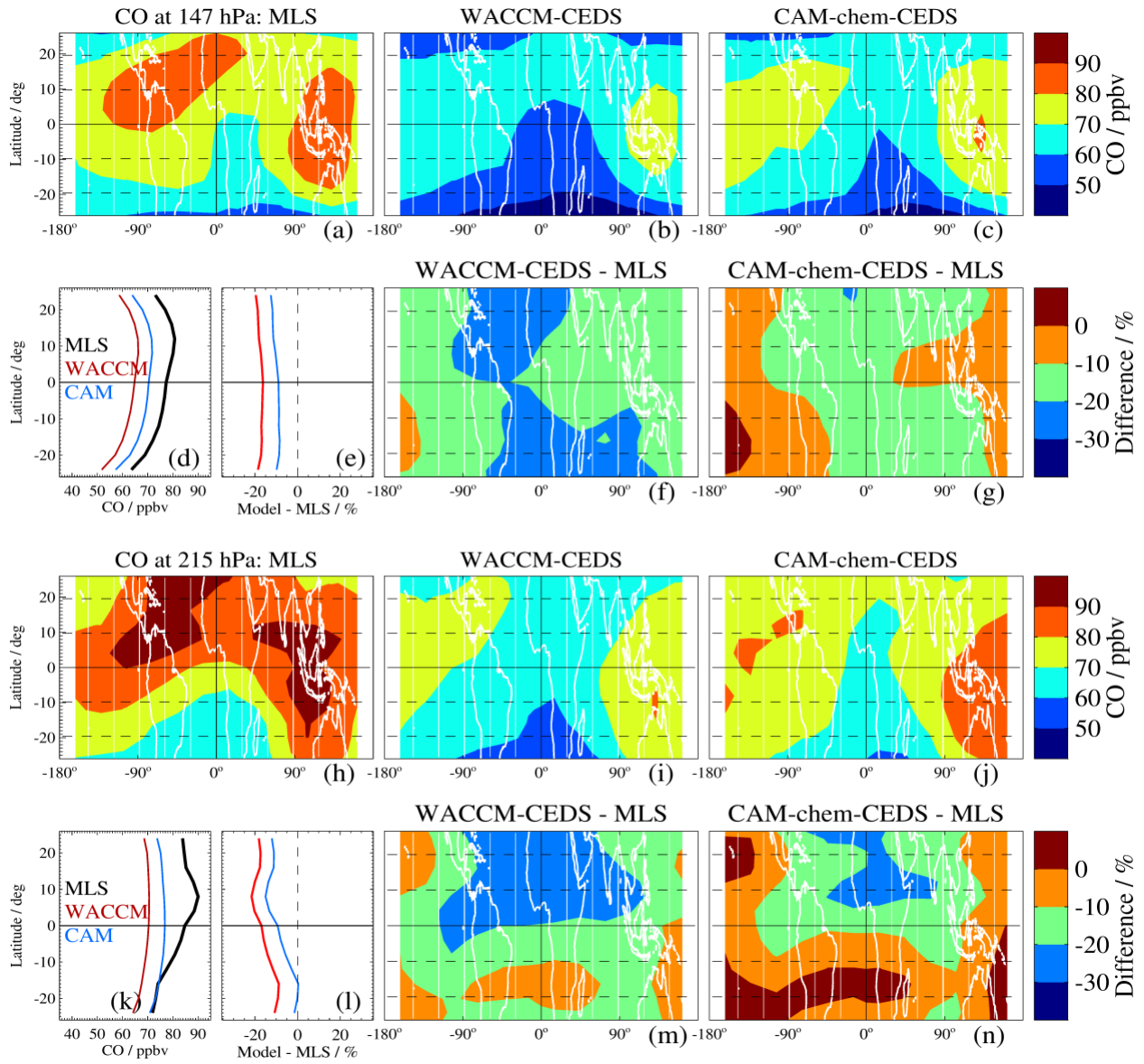
1540
1541
1542
1543
1544
1545
1546

Figure 6. Contributions to the time series variance from the main fitted components of the regression to the gridded tropical MLS ozone time series at 147 hPa (top 6 panels) and the same for the WACCM-CEDS time series (bottom 6 panels). The titles in each panel indicate that the explained variance is from specific components (annual, semi-annual, short-term, meaning 3- and 4-months, QBO, ENSO, and full fit).

1548
1549

1550 **Figure 7.** Sensitivity coefficient to ENSO for ozone at 147 hPa (top panels) and 215 hPa (bottom panels);
 1551 MLS results are shown in the left panels and the WACCM-CEDS results in the right panels. The black
 1552 crosses show the grid boxes for which the sensitivity is not significantly different from zero (based on the
 1553 2σ error estimates). Note that this color bar is assymmetric, with larger negative values than positive values.
 1554

1555
1556



1557
1558
1559
1560
1561
1562
1563
1564
1565
1566

Figure 8. Same as Fig. 1, but for CO.

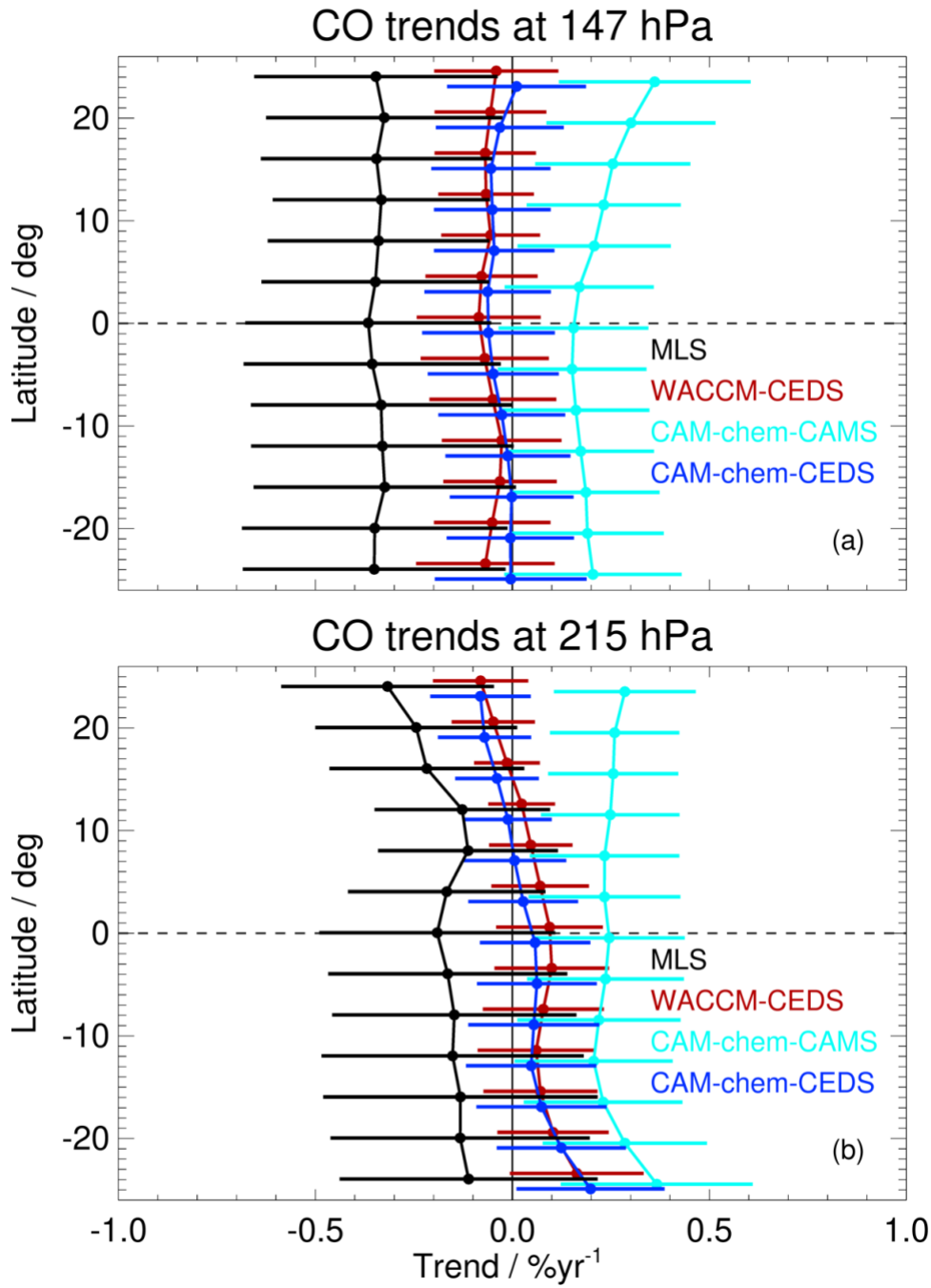
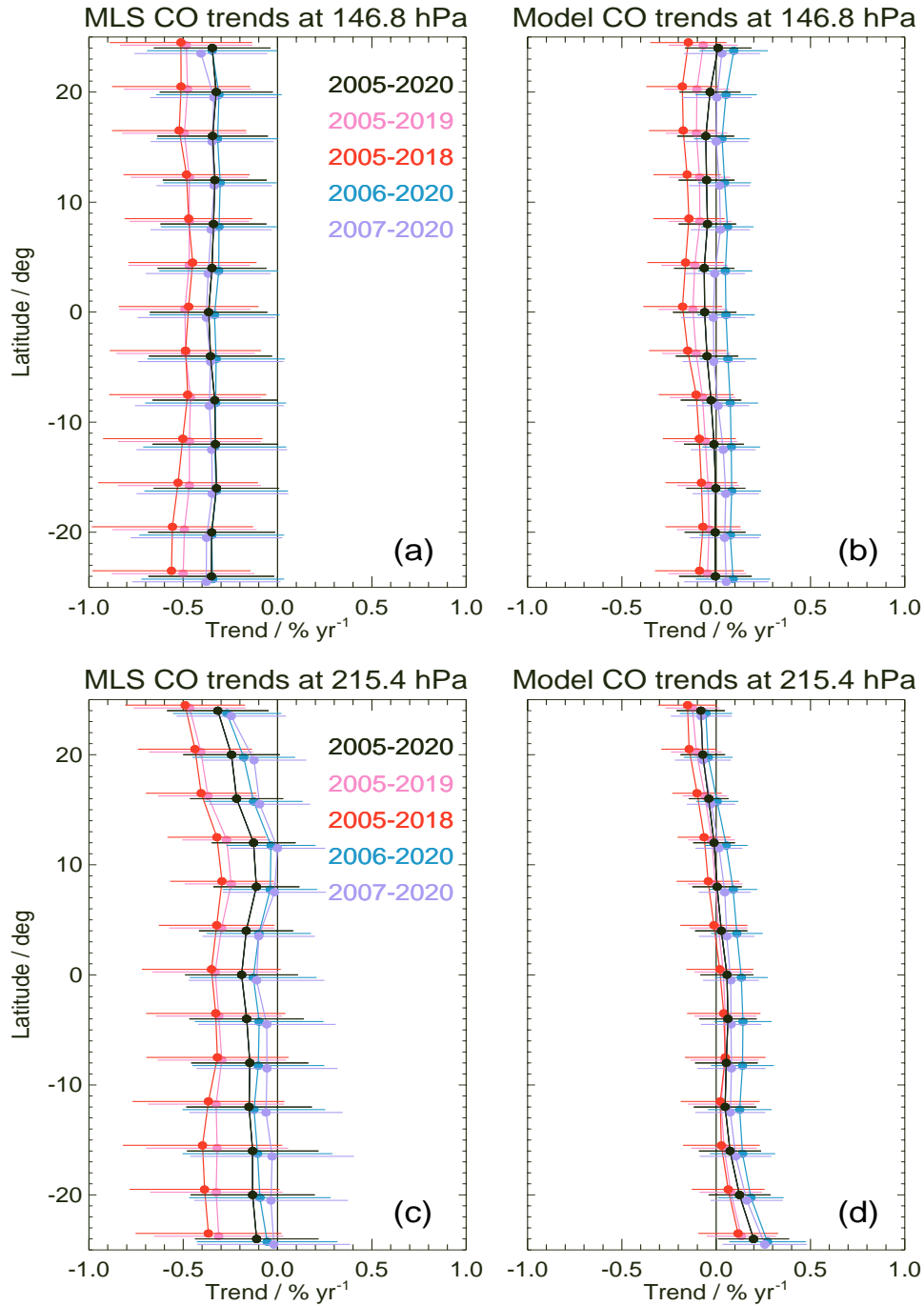


Figure 9. Same as Fig. 2, but for CO zonal mean trends for (a) 147 hPa, and (b) 215 hPa.

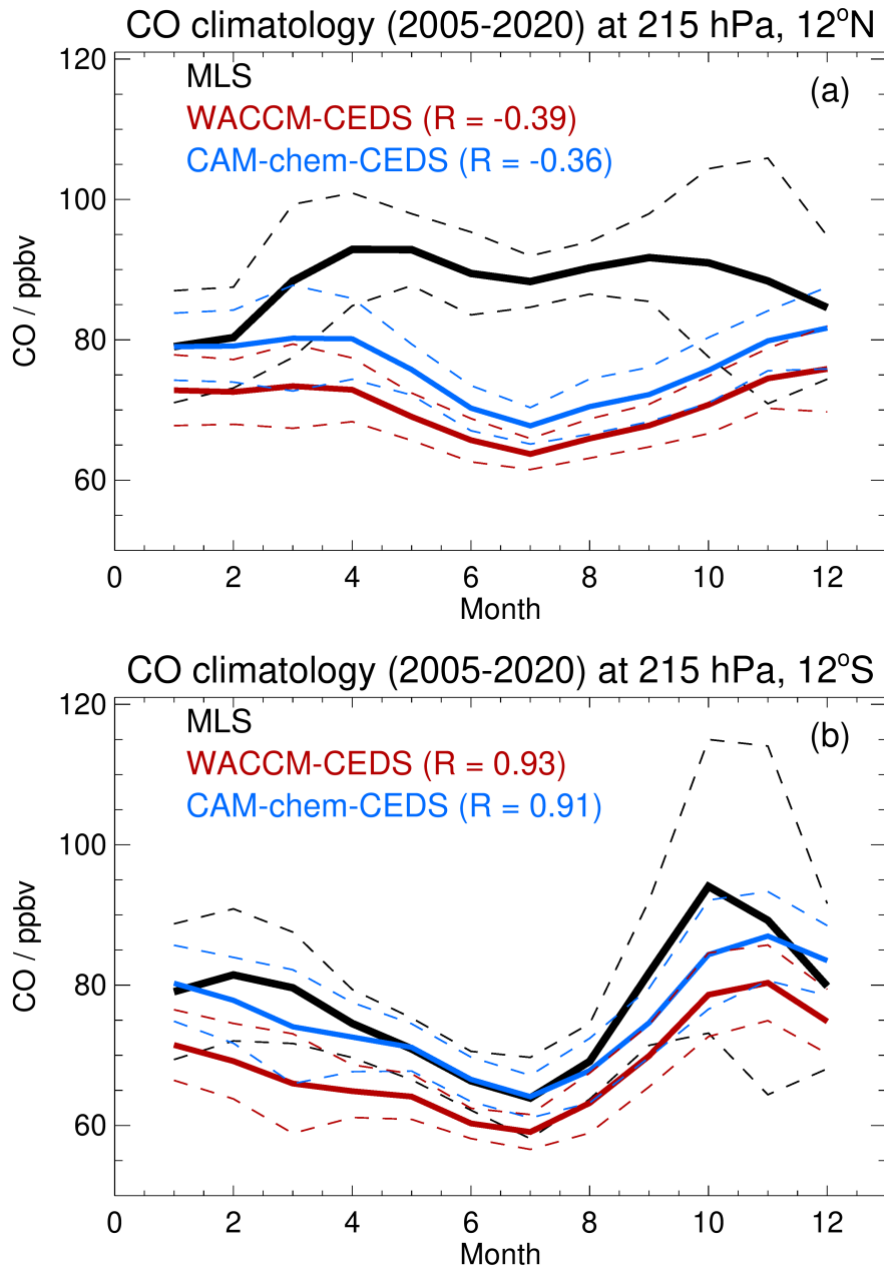
1568
 1569
 1570
 1571
 1572
 1573
 1574
 1575



1576
 1577
 1578
 1579
 1580

Figure 10. Same as Fig. 3, but for CO tropical zonal mean trends from MLS and CAM-chem-CEDS at the MLS CO UT retrieval levels of 147 and 215 hPa.

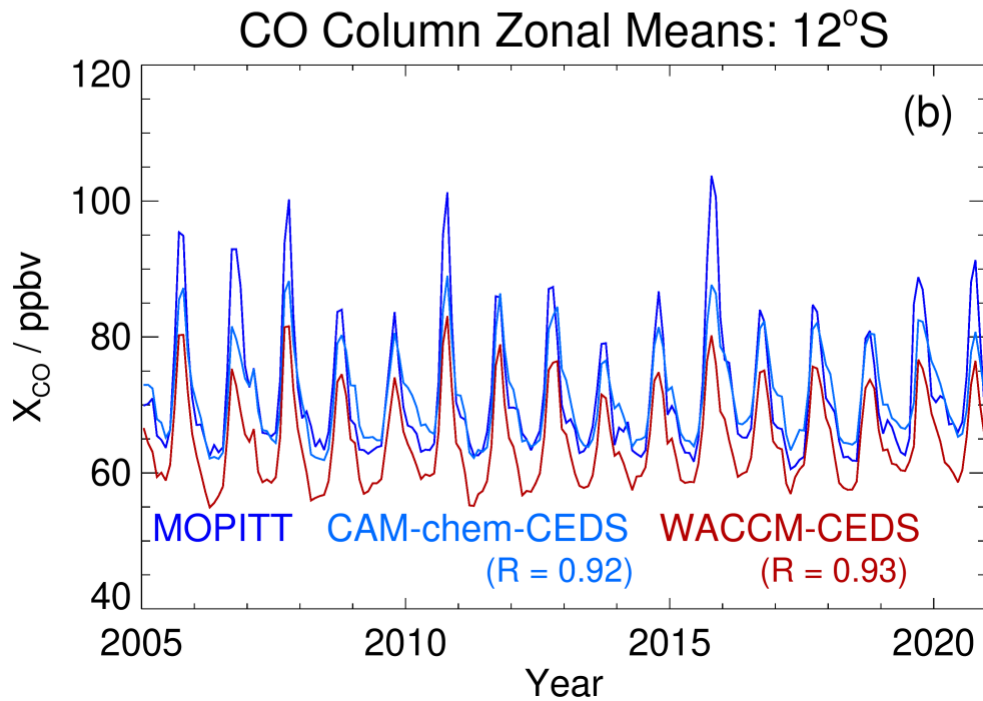
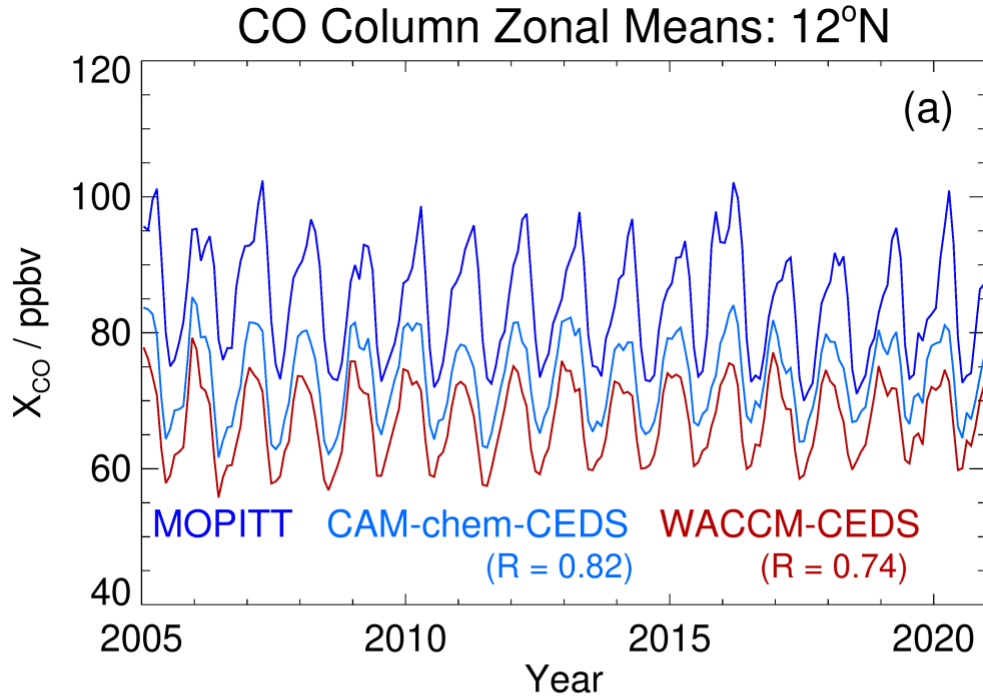
1581
1582
1583
1584
1585
1586



1587
1588
1589
1590
1591
1592
1593
1594

Figure 11. CO climatology at 215 hPa (using the 2005–2020 period) from MLS, WACCM-CEDS, and CAM-chem-CEDS for 4°-wide latitude bins centered at (a) 12°N and (b) 12°S. The thick solid lines represent the mean values from MLS (black), WACCM-CEDS (red) and CAM-chem-CEDS (blue), with corresponding variability estimates (twice the standard deviations) given by the colored dashed lines about each mean.

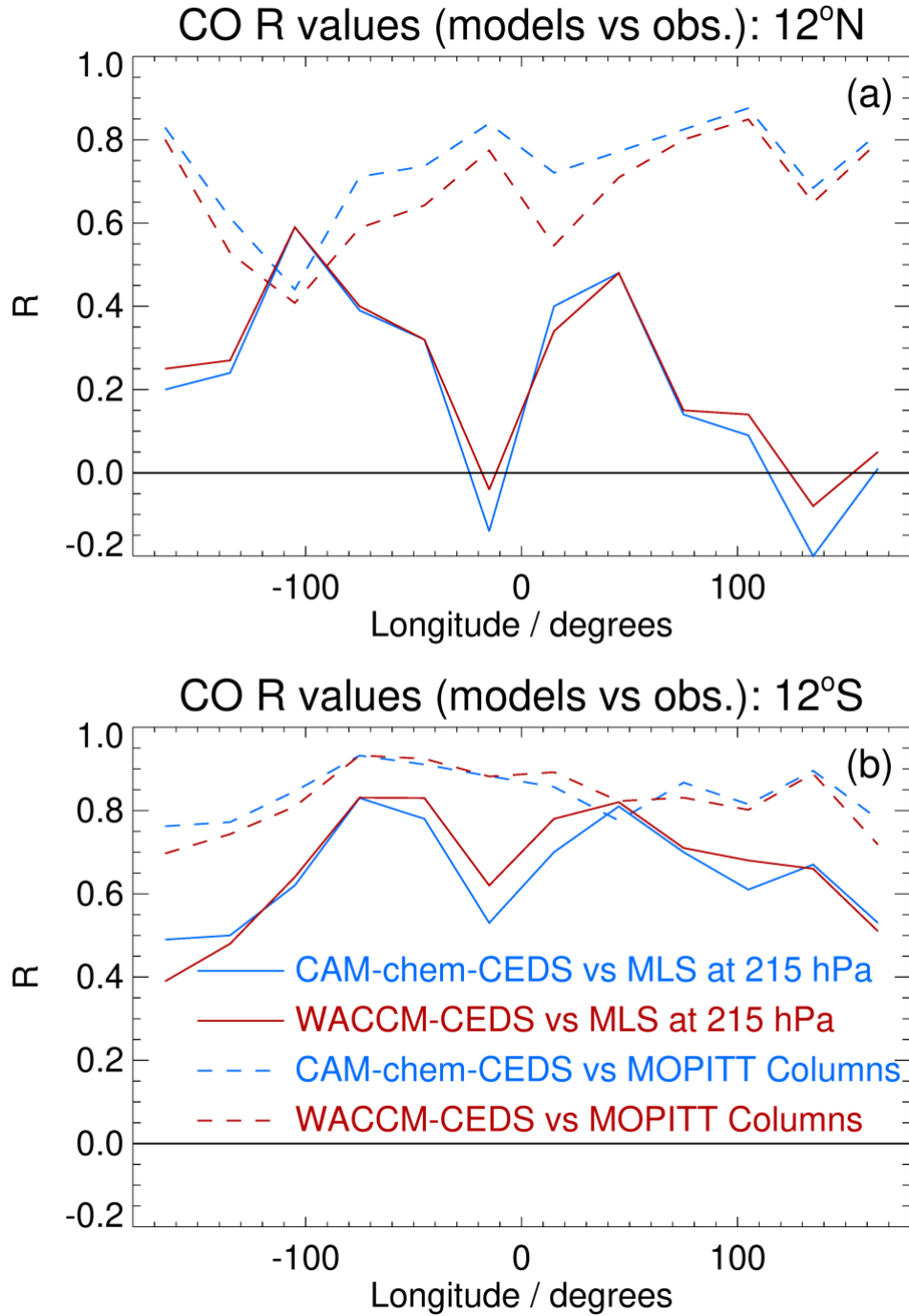
1595
1596



1597
1598
1599
1600
1601
1602
1603

Figure 12. CO column comparisons between zonal mean time series from MOPITT (purple) X_{CO} (see text) and from CAM-chem-CEDS (blue) and WACCM-CEDS (red) for 4°-wide latitude bins centered at (a) 12°N and (b) 12°S.

1604
1605



1606
1607
1608
1609
1610
1611
1612

Figure 13. Correlation coefficient values (R) for the zonal mean time series from the model CO columns (CAM-chem-CEDS in blue, WACCM-CEDS in red) versus MOPITT columns (dashed) and from the same two models' CO mixing ratios versus MLS CO at 215 hPa (solid) for 4°-wide latitude bins centered at (a) 12°N and (b) 12°S.

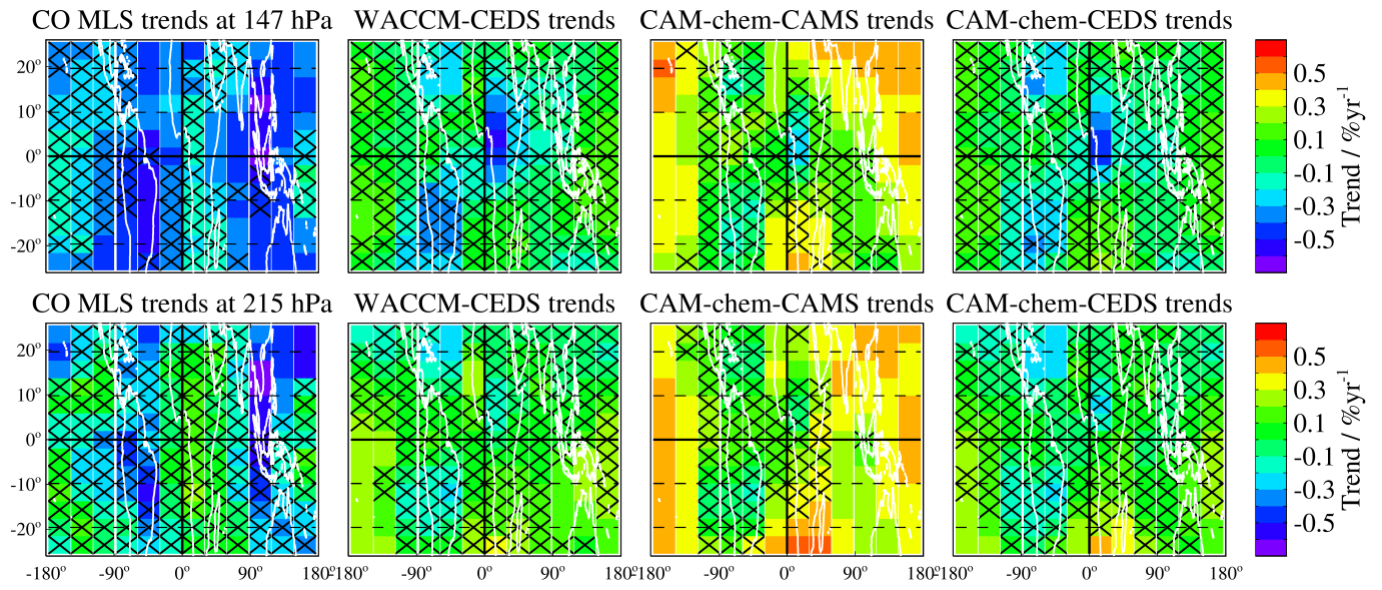
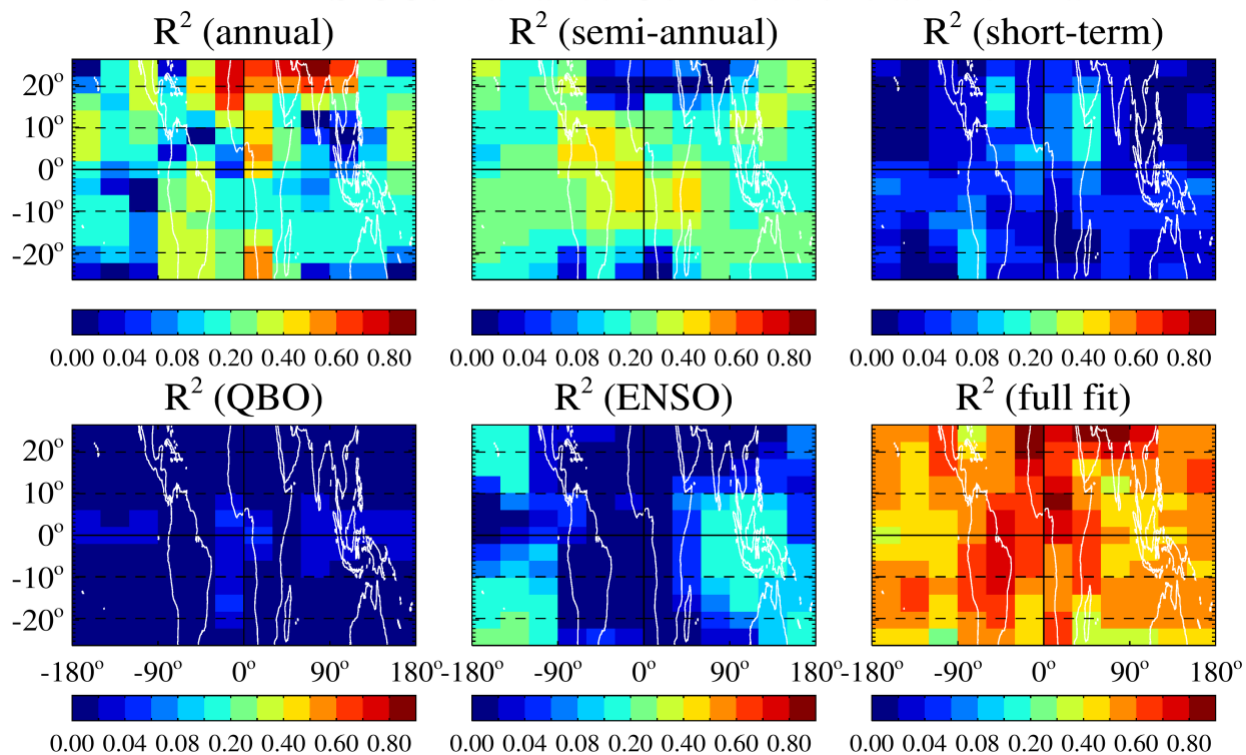
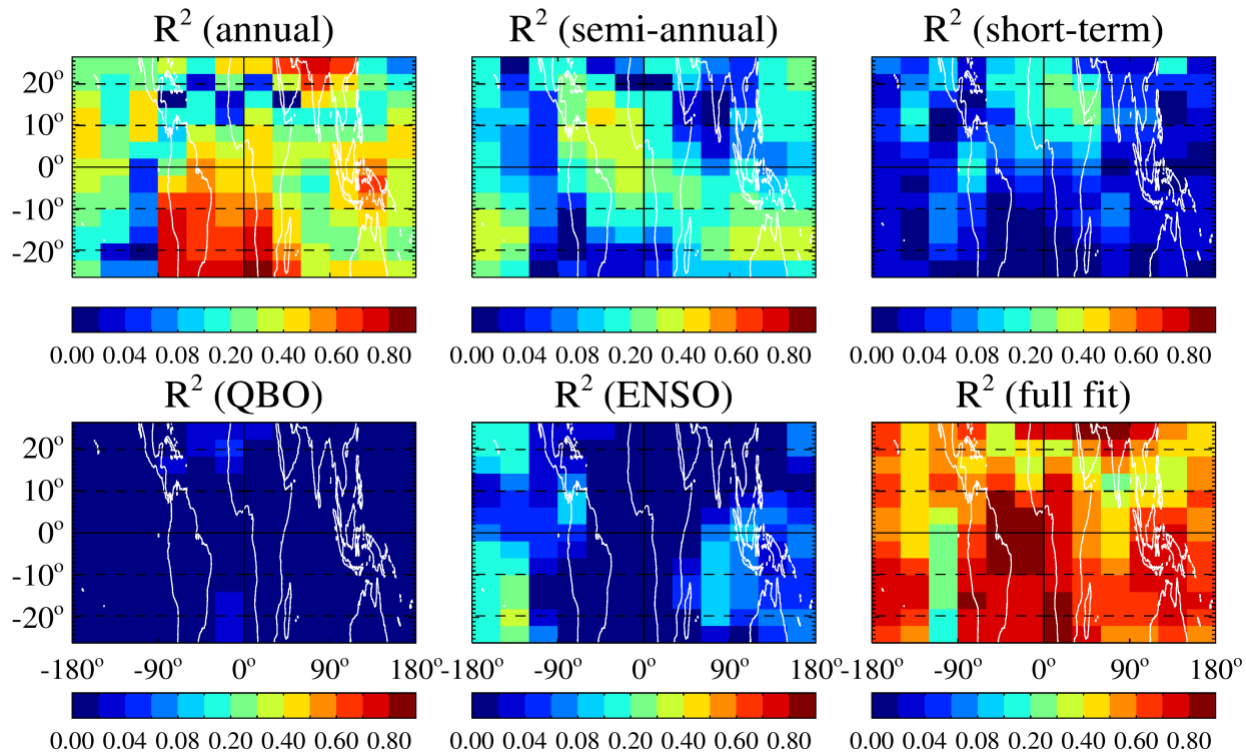


Figure 14. Same as Fig. 4, but for CO trends and all three model simulation results.

MLS CO: Variance Contributions at 147 hPa



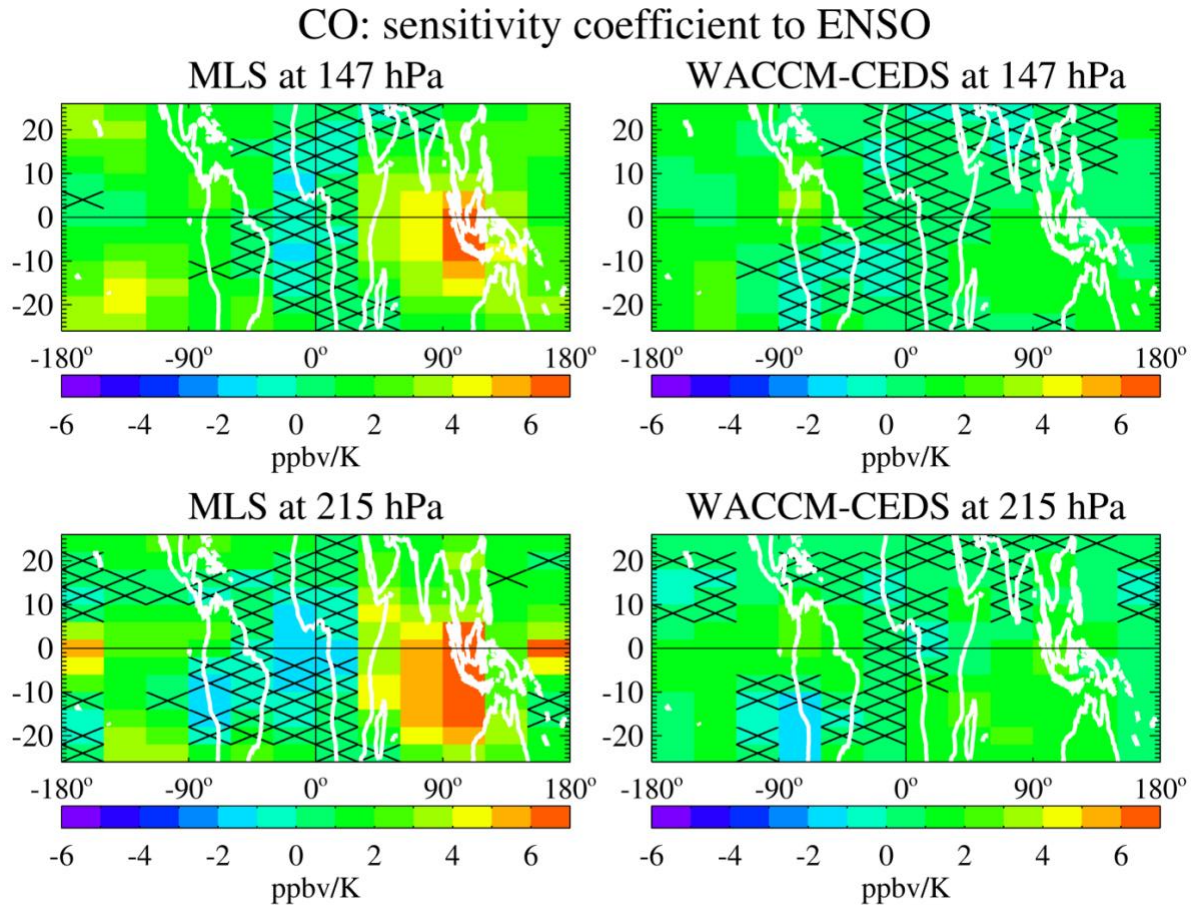
WACCM-CEDS CO: Variance Contributions at 147 hPa



1618
1619
1620

Figure 15. Same as Fig. 6, but for CO

1621
1622



1623
1624
1625
1626
1627

Figure 16. Same as Fig. 7, but for CO; unlike for O₃, there is no need here for an asymmetric color bar, but the positive range is the same as in the O₃ Figure.